

Copyright

by

Daniel Birt

2013

**The Dissertation Committee for Daniel Birt Certifies that this is the approved  
version of the following dissertation:**

**Imaging and Control of Magnetization Dynamics for Spintronic Devices**

**Committee:**

---

Xiaoqin Li, Supervisor

---

Maxim Tsoi, Co-Supervisor

---

Li Shi

---

Allan MacDonald

---

James Erskine

---

Dean Neikirk

**Imaging and Control of Magnetization Dynamics for Spintronic Devices**

**by**

**Daniel Birt, BS Physics**

**Dissertation**

Presented to the Faculty of the Graduate School of

The University of Texas at Austin

in Partial Fulfillment

of the Requirements

for the Degree of

**Doctor of Philosophy**

**The University of Texas at Austin**

**May 2013**

## Acknowledgements

It is difficult for me to imagine how I could have persevered through the difficult times when success seemed so elusive without the encouragement and support of my lovely wife. Likewise, the high points would not have seemed so high without her. Our son and bundle of joy joined us just in time to help me make the final push to wrap up a few programs and write this dissertation. I have to apologize if at any point I seem to be babbling. Those parts must have been written after one of our long conversations.

I owe a lot to Prof. Li for her patience, support, and guidance throughout the past six years. Embarking on this project was truly an adventure, and the way forward was rarely clear. I can only imagine the patience she required in watching me move from misstep to mishap and constantly biting off more than I could chew. Looking back on all of the difficulties and seemingly too rare victories, I can say with conviction that it was all a beneficial experience. Although I can only claim to have completed a small part of our original goals, I hope I have left her with a lasting and productive program. From the beginning I had the feeling that we would work well together, and I am happy to say that was indeed the case. I can only hope to have such natural working relationships with my supervisors in the future.

I also thank, Prof. Tsoi, my co-supervisor for his advice and helpful criticism.

I was extremely lucky to be able to learn the  $\mu$ -BLS technique from the inventors Dr. Demidov and Prof. Demokritov at the University of Muenster. I owe much of the success of our system to their assistance and hospitality. I am also grateful for the help of Prof. Ricketts and Dr. Shingo Tamaru at Carnegie Mellon University for inviting me to their lab to use their phase resolved scanning Kerr effect microscopy system. Our

collaborators at the Western Institute of Nanoelectronics at the University of California – Los Angeles provided us with many interesting samples to study.

My successor, Kyongmo An, deserves profuse thanks from me for his hard work in helping to complete the final projects and for his patience as I tried to relay my feeble understanding in half sentences, jumbled words, and confusing diagrams. With confidence I leave the  $\mu$ -BLS system in his capable hands, though I cannot say for certain if I was much help in his training.

I am thankful for the interesting conversations and things I have learned from all of my labmates throughout the years: Daniel, Tom, and Meg from the first batch of students; Tom, Akshay, Kavir and Sarah who joined the group after me. I must also acknowledge Dr. Yanwen Wu for instituting the wonderful tradition of the weekly group lunch. I also owe thanks to Dr. Konrad Dziatowski who was an immense help in the early days of the magnetism project.

Finally, I would like to thank the members of my committee for their interest in my work. It was an absolute pleasure presenting our results and attempting to answer their insightful questions.

## **Preface**

This dissertation is divided into three main sections. In the first section I explain the theory necessary for understanding the measurements. Chapter 1 motivates the current research. I discuss the current state of spintronics research and how the topics of this dissertation fit into the overall field. I also stress the relevance to device applications. Chapter 2 describes the static and dynamic aspects of magnetization for ferromagnetic films. Brillouin Light Scattering Spectroscopy is described in Chapter 3 where I discuss how this technique can be used to probe magnetization dynamics. In the second section I describe the experimental methods used in my research. Chapter 4 explains the experimental methods used in this research. First, the  $\mu$ -BLS system including the essential optical components, Sandercock interferometer, electronics, and the control software are discussed. The sample fabrication techniques are also discussed. In the third section I discuss projects that have been completed and suggestions for future research. My results both published and unpublished are presented in Chapter 5. The outlook and conclusions are provided in Chapter 6.

# **Imaging and Control of Magnetization Dynamics for Spintronic Devices**

Daniel Birt, PhD

The University of Texas at Austin, 2013

Supervisor: Xiaoqin Li

Co-supervisor: Maxim Tsoi

As features on integrated circuits continue to shrink, currently at 22 nm and predicted to approach 10 nm by 2020, the semiconductor industry is rapidly brushing up against the fundamental limits of electric charge and current based devices. These limits are due to the fact that charges are being pushed around in tiny areas and they repel one another with significant force. Fortunately, there are many other degrees of freedom in solids that do not suffer from these limitations and are just waiting to be harnessed in useful devices. This idea is behind all of the fields that have lately been proliferating ending in -onics, photonics, plasmonics, phononics, and of most relevance to this dissertation spintronics. Spintronics refers to a field of research wherein ways are sought to utilize the spin property of the electron in devices. One of the most attractive aspects of electron spin is that it can be used to store (transiently or permanently), process, and transmit information.

The main challenge in spintronics is accessing the spin degree of freedom. Until the discovery of the giant magnetoresistance effect in the late 1980's, the only way to manipulate the electron spin was through a magnetic field. Recent developments have

shown that electron spins can be controlled with direct currents of both heat and electrons, which have the benefit of being easy to generate and direct without interfering over a large area.

The purpose of this dissertation is to study methods of controlling the dynamics of magnetization in thin films for spintronic applications by imaging the spin wave intensity in devices. To this end we have constructed a micro-focus Brillouin Light Scattering system to map the intensity of spin waves propagating in thin ferromagnetic films on the sub-micron scale. We have studied issues relating to fundamental issues of spin wave propagation in thin films. We have investigated the possibility of spin wave amplification with direct charge currents and spin currents generated by the spin Hall effect. Furthermore, we have demonstrated the ability to measure the magnon and phonon temperatures, which is important for studies of thermal transport.

## Table of Contents

|   |          |
|---|----------|
| Preface.....  | vi       |
| List of Tables .....  | xi       |
| List of Figures .....   | xii      |
| <b>CHAPTER 1: MOTIVATION .....</b>                                      | <b>1</b> |
| 1.1 Spintronics and the Future of Electronics .....                     | 1        |
| 1.2 Recent Developments In Spintronics.....                             | 5        |
| 1.3 Role of Magnetic Dynamics in Spintronic Devices.....                | 11       |
| 1.4 Imaging of Magnetic Dynamics.....                                   | 13       |
| Chapter 2: Magnetism.....   | 18       |
| 2.1 Ferromagnetism .....  | 18       |
| 2.2 Magnetic Dynamics .....   | 34       |
| 2.3 Spin Waves .....  | 38       |
| 2.4 Spin Waves in Confined Structures .....                             | 44       |
| 2.5 Exciting Magnetic Dynamics.....                                     | 46       |
| Chapter 3: Brillouin Light Scattering .....                             | 48       |
| 3.1 Brillouin Light Scattering Spectroscopy.....                        | 48       |
| 3.2 Magneto-optic Kerr Effect.....                                      | 52       |
| 3.3 Brillouin Light Scattering from Spin Waves .....                    | 58       |
| Chapter 4: Experimental Methods .....                                   | 62       |
| 4.1 micro-BLS system .....  | 62       |
| 4.2 Sample Fabrication .....  | 78       |
| Chapter 5: Experiments.....   | 87       |
| 5.1 Introduction.....   | 87       |
| 5.2 Diffraction of Spin waves in a Waveguide from a Defect .....        | 89       |
| 5.3 Radiation of Spin Waves from a Waveguide into a Continuous Film.... | 99       |
| 5.4 Deviation of Spin Waves from Exponential Decay.....                 | 113      |

|   |     |
|---|-----|
| 5.5 Measurement of Magnon and Phonon Temperatures ..... | 124 |
| Chapter 6: Conclusions .....                            | 135 |
| 6.1 Summary of Work Completed .....                     | 135 |
| 6.2 Works Published or Presented .....                  | 140 |
| 6.3 Outlook .....                                       | 141 |
| Bibliography .....                                      | 143 |

## List of Tables

|   |    |
|---|----|
| Table 2.1. Comparison between the $g$ factors measured with FMR ( $g$ ) and those measured with the gyromagnetic effect ( $g'$ )..... | 26 |
| Table 3.1. Equivalent energies.....   | 51 |
| Table 3.2. Magneto-optic coefficients for iron, cobalt and nickel at 514 nm.....  | 58 |

## List of Figures

|  |    |
|--|----|
| Figure 1.1. Example spintronic applications.....   | 5  |
| Figure 2.1. Comparison of the magnetic fields $\mathbf{B}$ and $\mathbf{H}$ . .....                                  | 31 |
| Figure 2.2. Illustration showing the nonuniform internal magnetic field of a stripe magnetized along its width. .... | 33 |
| Figure 2.3. Illustration of magnetization precession.....  | 38 |
| Figure 2.4. Illustration of a spin wave. ....  | 39 |
| Figure 2.5. Calculated dispersion relation for spin waves in a thin film of permalloy. ....                          | 44 |
| Figure 3.1. Sketch of Brillouin light scattering spectrum. ....  | 49 |
| Figure 3.2. The three different configurations of MOKE measurements. ....  | 53 |
| Figure 3.3. Illustration of MOKE on linearly polarized light. ....   | 54 |
| Figure 3.4. BLS spectrum from spin waves excited at 10.2 GHz.....  | 61 |
| Figure 4.1. Schematic of the $\mu$ -BLS setup.....   | 62 |
| Figure 4.2. Photograph of our $\mu$ -BLS system. ....  | 63 |
| Figure 4.3. Schematic of the $\mu$ -BLS software control system. ....  | 65 |
| Figure 4.4. $\mu$ BLS drift correction procedure. ....   | 67 |
| Figure 4.5. Data showing drift correction required over a three-day scan. ....                                       | 68 |
| Figure 4.6. (a) Sketch of Sandercock interferometer. (b) Effect of tandem cavities on collected spectra. ....        | 73 |
| Figure 4.7. Thermal spin wave spectrum for a 30-nm-thick film in a 1000 Oe field. ....                               | 76 |
| Figure 4.7. Scanning electron microscope images of Py waveguides. ....   | 80 |
| Figure 5.1. Drawing of Permalloy waveguide with hole to scatter spin waves.....                                      | 91 |

|   |     |
|---|-----|
| Figure 5.2. Dispersion curves for three odd-ordered transverse wave guide modes.      | 92  |
| Figure 5.3. Measured and calculated spin wave diffraction pattern.                    | 93  |
| Figure 5.4. Reflection of spin wave from defect.                                      | 96  |
| Figure 5.5. Edge mode propagation around defect.                                      | 97  |
| Figure 5.6. Drawing of permalloy waveguide emptying into a continuous film.           | 100 |
| Figure 5.7. Dispersion of spin waves in the waveguide and continuous film.            | 101 |
| Figure 5.8. Behavior of spin waves at frequencies too low to propagate in the film.   | 105 |
| Figure 5.9. Constant frequency curves of spin waves showing the group velocity.       | 107 |
| Figure 5.10. Angular dependence of the spin wave group velocity.                      | 108 |
| Figure 5.11. Maps of spin wave radiation at different frequencies.                    | 109 |
| Figure 5.12. Illustration of the measured device and experimental configuration.      | 114 |
| Figure 5.13. Antenna response as a function of frequency.                             | 115 |
| Figure 5.14. Spatial scan taken below resonance at 9.8 GHz.                           | 116 |
| Figure 5.16. Experimentally determined dispersion relation (blue dots).               | 120 |
| Figure 5.17. Experimentally determined spin wave propagation lengths (blue dots).     | 121 |
| Figure 5.18. Experimental schematics.   | 125 |
| Figure 5.19. Magnetic field dependent thermal magnon spectra.                         | 126 |
| Figure 5.20. Temperature dependent thermal magnon spectra in a uniformly heated film. | 129 |
| Figure 5.21. Extracted magnon temperature along the thermal gradient.                 | 131 |
| Figure 5.22. Phonon temperature measurements.   | 133 |

# CHAPTER 1: MOTIVATION

## 1.1 SPINTRONICS AND THE FUTURE OF ELECTRONICS

Moore's law continues to maintain its status as a self-fulfilling prophesy. Every 18 months the computational power of microprocessors doubles. This expectation drives the marketing, which drives consumer demand, which drives research and development. So far, the engineers have managed to overcome the challenges and keep pace with continued improvement to the complementary metal-oxide-semiconductor (CMOS) processes. However, as the minimum feature size on integrated circuits continue to shrink these charge and current based devices are approaching their physical limits for speed and size. The minimum feature size is 22 nm as of 2013 and is expected to come below 10 nm by 2020. Problems such as increasing interconnect delay and off-state current leakage limit the speed and power dissipation in microchips as the feature size decreases. These problems stem from the fact that electrons repel one another quite strongly on such small length scales and lead some to talk about fundamental limits to the scaling of CMOS. There is reason to be skeptical about so-called fundamental limits, however. Such limits have been discussed since CMOS was first introduced in the early 1980's, and every time engineers have found a way to overcome them within the CMOS framework. Although it is difficult to pinpoint exactly when and for what reason conventional CMOS will reach its limits, it is inevitable that at some point in the near future a new way to store, transfer, and process information on chips will be required that involves more than just itinerant charge carriers.

Conventional electronics treats the electron simply as a mobile charged particle. Most of the difficult scaling problems in stem from the fact that electrons are conserved, meaning that once they are transferred some place they must be transferred to another place before another operation can be performed and the fact that electrostatic repulsion becomes extremely strong on the nanometer scale. Fortunately, there are other degrees of freedom in materials that do not suffer from the same deficiencies. This exploration of other degrees of freedom in condensed matter that could be incorporated in electronic devices is behind all of the fields that have lately been proliferating ending in –onics; for example, photonics where light is directed through nanometer sized channels; plasmonics, where resonances in collective electron motions are utilized; phononics, which makes use of lattice vibrations; and of most relevance to this dissertation spintronics. Spintronics refers to a field of research wherein ways are sought to utilize the spin property of the electron in devices. One of the most attractive aspects of electron spin is that it can be used to store (transiently or permanently), process, and transmit information.

Spintronics term was coined by S. A. Wolf in 1996 to name a Defense Advanced Research Projects Agency (DARPA) initiative for novel magnetic materials and devices. (See [1] for an early review by Wolf et al. circa 2000 on the subject.) In a way, the use of electron spin in computation is not new. The spin property of the electron has been used as a way to store information since almost the beginning of modern computing through its manifestation in the magnetic moment of ferromagnetic materials [2]. Moreover, ferromagnetic materials have been used in microwave electronics for their unique

gyrotropic properties [3]. This new initiative of spintronics, however, seeks to merge the tasks of information processing and storage in the basic building blocks of integrated circuits. A further goal is to introduce functionality that would not be possible with charge-based devices. The field of spintronics was spawned by discoveries of new ways to manipulate both microscopic and macroscopic electron spin states, which previously could only be accomplished with the Oersted field of an electric current. These discoveries were enabled in the late 1980's by the development of methods to deposit films with high quality interfaces. Developments in the field continue to be strongly dependent on the exploration and discovery of new material systems.

The field of spintronics can be classified into two subfields that are clearly divided in their approaches and bodies of literature. First, there is microscopic spintronics, in which researchers seek ways to control single electron spins in atomic sites in crystals, such as nitrogen-vacancy centers in diamond [4] or in quantum dots. Here the spins are treated as qubits useful for quantum computation and the fact that spin is a natural two state system makes it useful for performing logic operations. Such efforts are for the time being confined to cryogenic temperatures, and actual device applications do not seem to be on the horizon. Then, there is macroscopic spintronics, in which large populations of spins are manipulated. For example, the magnetization state of a nanomagnet may be flipped to store information or spin waves may serve to process or transmit information. Macroscopic spintronic experiments are typically done at room temperature since there is a more urgent focus on making practical devices. This is the field in which the work of this dissertation belongs. One can expect, that as the

microscopic field finds ways to perform qubit operations at higher temperatures and the dimensions of macroscopic spintronic devices decreases, these two fields will eventually meet to produce some truly new devices where information processing, storage, and transmission are completely integrated into a single framework utilizing microscopic states.

In the meantime proposals have been made to create device frameworks utilizing macroscopic spintronic effects. Some of the major components are pictured in Figure 1.1. Components for information storage include magnetic random access memory (MRAM) [5] and racetrack memory [6] for data storage, which promise to provide a universal memory that would have all of the attributes of static RAM, dynamic RAM, and Flash. RF components have been proposed including spin torque nano-oscillators (STNOs) for generating high frequency currents [7], [8], spin torque microwave detectors (STMDs) for detecting high frequency signals [9], [10]. Frequency filtering could be accomplished through magnonic crystals [11]. Computations could also be performed with magnetic dynamics with spin wave logic [12] components and spin valves for sensing magnetic states. All of these devices could be connected together and to other electronic components with a spin wave bus consisting of magnetic waveguides existing in the metal interconnect layer of CMOS chips [13].

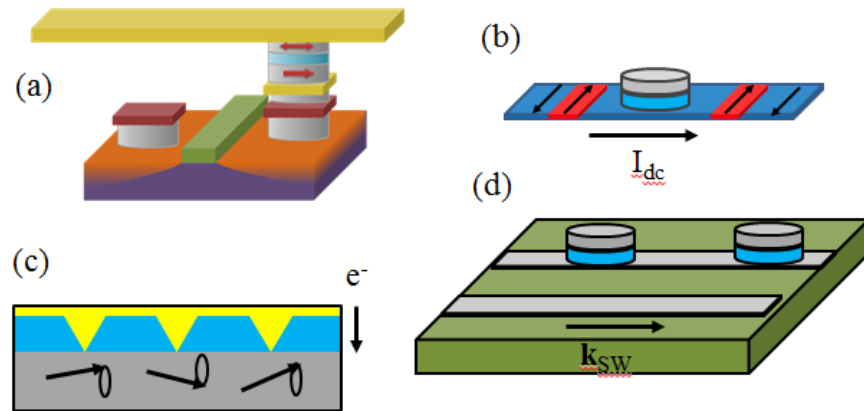


Figure 1.1. Example spintronic applications. (a) STT MRAM, (b) Racetrack memory, (c) spin torque nanoscillators, and (d) spin wave bus. See text for references.

## 1.2 RECENT DEVELOPMENTS IN SPINTRONICS

Here we wish to explain the recent developments that have provided the necessary background knowledge for the development of the devices described in the previous section. The development has proceeded along two veins.

First, magnonic crystals, spin wave logic, and spin wave bus devices are based on previous work on magnetization dynamics, which began with an understanding of ferromagnetic resonance [14]. Interest in spin waves and nonlinear effects reached a height in the 1960's and 1970's with the discovery of the insulating ferrite yttrium iron garnate (YIG), which is still one of the archetypical materials for studying spin wave propagation. Much of the current theory of spin waves was developed around that time. This knowledge has long been employed in microwave ferrite devices used in RF signal processing [3]. Later, nanofabrication techniques allowed the construction of devices to

manipulate spin wave propagation characteristics on the micron scale and smaller. This development ushered in the field that has recently become known as magnonics [15], a closely related field that some may consider to be subset of spintronics.

Second, MRAM, racetrack memory, STNO's and STMD's developed out of a new understanding of electron spin transport in metals. The field of spintronics is typically considered to have begun with the discovery of the giant magnetoresistance effect (GMR) in 1988 by the research groups of Peter Grünberg [16] and Alan Fert [17]. GMR describes a large change in resistance that is observed in multilayered metallic structures consisting of a nonmagnetic metal sandwiched between two ferromagnetic layers that occurs when the magnetizations of the two layers are aligned vs. misaligned. The reason this discovery was so significant is that it was the first to demonstrate a magnetically affected transport effect that occurred at room temperature and produced a significant effect for reasonable currents and could therefore be employed in commercial products. The adoption of the effect into actual devices happened quite rapidly so that by 1994, the first commercial product (a magnetic field sensor) became available, and in 1997 GMR sensors had become widely adopted in the read heads of hard disc drives [18]. GMR sensors have now been replaced by tunneling magnetoresistance (TMR) read heads that operate in a similar manner, but where the non-magnetic metal is replaced by a thin insulating layer. During the 10 years they were employed, the density of information stored on hard disks increased from 1 Gbit/in<sup>2</sup> to 600 Gbit/in<sup>2</sup>. Grünberg and Fert were awarded the Nobel prize in physics in 2007 considering the significance of the technological impact of their discovery. For an excellent review of new developments in

spin transport related spintronics please see the 2012 Nature Materials insight on the subject [19].

It is important to note that the use of magnetism in electronics preceded the discovery of GMR by a long shot, but the nature of the interaction between the electronic and magnetic parts was fundamentally different. The interaction between charge and the magnetization was mediated by the Oersted fields. For example, before GMR, hard disk read heads were made of inductive coils that sensed the magnetic fields of the domains on the disk. GMR is an effect due to spin polarized electron transport, not due to the Oersted field. This is essential for electronic devices because the spin transport interaction is local unlike the Oersted field, which can be quite difficult to confine to sub 100 nm dimensions. Magnetic effects on electron transport had been studied since Lord Kelvin discovered anisotropic magnetoresistance in 1857. In 1936, Mott proposed that conduction electrons in ferromagnets may be divided into two channels according to whether the electron is aligned parallel or opposite to the magnetization. This picture is valid as long as typical scattering events do not flip the spin of the electron. Spin transport effects did not attract much attention at first because high quality samples could not be fabricated. The discovery of GMR had to wait until the development of ultra-high vacuum sputtering systems that could produce high quality films with high repeatability.

One concept that characterizes recent developments in spintronics is that every effect has an inverse effect, and the inverse effect of GMR is the spin transfer torque (STT). STT describes how a polarized electron current can exert a torque on a magnetic layer to alter the direction of its magnetization. This effect was theoretically predicted in

1996 by Berger [20] and Slonczewski [21]. The first experimental evidence of STT was reported by Tsoi et al. [22] in a mechanical point contact configuration. Shortly thereafter switching of a multilayer was demonstrated in a pillar shaped spin valve [23], which opened the door to a new type of magnetic random access memory (MRAM) where bits are written with the STT rather than Oersted fields. New technology based on tunneling magnetoresistance (TMR) is being developed by companies, such as Everspin, as of the time of this writing (2013).

Another, technologically significant aspect of the STT is that the direct current induces dynamics in the microwave frequency range, a fundamentally new functionality that is not possible to achieve with a static Oersted field. High frequency dynamics induced by a spin polarized current were demonstrated in Refs. [7], [24], [25], which opened the possibility of microwave oscillators that could be integrated with digital electronics. The frequency can be tuned with the magnitude of the applied current. Moreover, it has been shown that the oscillations of several spin transfer nano-oscillators (STNOs) could be phase locked [26–28], which is essential to obtain the power levels required for practical applications in telecommunications.

The STT utilized in spin valve structures requires an electric current to obtain a spin current. The drawbacks of this method are that that a charge current is associated with the spin current so the same power dissipation issues affecting charge based electronics are still relevant and the polarization of the spin current is limited by the polarization of electrons in the ferromagnet, which is about 60-70% in Ni, Fe, Co and their alloys. Some of the newest developments in the field of spintronics have focused on

ways to generate spin currents that are not coupled to charge currents, i.e., pure spin currents. One of the benefits of a pure spin current is that it can be transferred to insulating magnetic materials where magnetization dynamics occur with much less dissipation than in metals. Two methods of generating pure spin currents that are receiving much attention lately are the spin Hall effect (SHE) and the spin Seebeck effect (SSE).

The SHE describes a process wherein spin-orbit interactions deflect the currents of spin up and spin down electrons in opposite directions, thus inducing a transverse spin current [29]. In non-magnetic metals, such as Pt which is commonly used to explore the SHE, the electrons are not polarized, and the transverse spin current is a pure spin current, which means it does not carry charge. SHEs can result from numerous spin-orbit interactions that can be extrinsic or intrinsic in nature, but do not require any external magnetic field to be applied. One of the main benefits of creating a pure spin current with the SHE is that it can induce a spin wave oscillation in a ferrimagnetic insulator, such as YIG, having small damping [30]. The SHE has also been utilized to tune damping in ferromagnetic metals [31], [32]. It is possible that three terminal SHE based spin valves could compete with MTJs for use in MRAM [33]. The main figure of merit for SHE materials is the spin Hall angle, which is defined as the ratio of the magnitude of the spin current to that of the charge current  $\theta_{SH} = J_s / J_c$ . SHE based memory elements would be much easier to fabricate than MTJs and could be improved by finding materials with larger spin Hall angles. So far, tungsten is the material with the largest known spin Hall angle [34].

The coupling of heat currents to spin currents offers another way to generate spin currents, which has attracted much interest lately. Spin caloritronics is the name of the field where such effects are explored [35]. The known spin caloritronic effects can be classified into two categories: 1) where itinerant electrons in metals are the main spin carriers and the effects can be understood with two channel transport with different thermoelectric properties, such as with the spin-dependent Seebeck effect [36]. 2) where collective effects, i.e., magnons, are the main spin carriers, which are present in metals and insulators, such as with the spin Seebeck [37]. The closeness of the names for these two different Seebeck effects is unfortunate and mainly due to the fact that the spin Seebeck effect was not understood at the time it was observed. A more proper name for the spin Seebeck effect might be the magnon Seebeck effect [35]. Spin caloritronic effects may provide a way to dissipate heat due to Ohmic resistance, which becomes increasingly harder to deal with as chip features become smaller. The heat dissipation can be put to good use in exciting magnetization dynamics and inducing switching in spin valves or MTJs. Hatami et al. proposed that spin-polarized thermoelectric heat currents can induce switching in spin valves [38]. Later, Slonczewski studied theoretically the spin-transfer torque when a thermal gradient is applied across a spin valve in which the polarizer is a magnetic insulator that exerts a torque on a free magnetic layer and found that the thermal torque may even be more efficient at switching the free layer than charge induced torque [39].

### 1.3 ROLE OF MAGNETIC DYNAMICS IN SPINTRONIC DEVICES

In the previous section we discussed the new ways to generate and utilize spin current that are currently being researched for device applications. Whether switching or microwave dynamics are beneficial, the dynamical magnetization processes must be understood because they play a part in both actions. The magnetization in a material is associated with angular momentum, unlike the electrical polarization. Therefore, when a torque is applied to the magnetic moment it precesses, typically with a period between a few tens of picoseconds or nanoseconds, so dynamical processes are involved even in switching nanopillars. For example, the critical currents required for switching and the switching times are affected by the dynamic states (spin wave modes) that may be excited by the STT [40]. Noise in magnetoresistive sensors is also highly dependent on these spin wave modes [41].

Spin wave generation is one of the key elements in magnonic and spintronic device applications. Spin wave dynamics play a particularly important role in the behavior of single and coupled STNO's. The coupling of arrays of STNO's is not well understood, but it is thought to be in large part mediated by spin waves propagating in the ferromagnetic film that joins the nanopillars. If the applied magnetic field is large enough the switching regime of the nanopillar is replaced by a regime of steady precession at microwave frequencies. The frequencies allowed are governed by the confined spin wave eigenmodes of the nanopillar. The excited eigenmodes of the nanopillar couple to the modes of the continuous film linking the nanopillars, and both localized nonlinear "bullet" modes can be excited [42] and propagating spin wave modes [43]. The bullet

modes are lower in frequency and not useful for the coupling of STNO's. who showed definitively using  $\mu$ -BLS that the spin waves are propagate with positive group velocity away from the nanopillar [44]. In other conditions, the spin transfer torque can also be used to generate an oscillatory motion of a magnetic vortex. Considering all of the dynamic processes involved from the 100's of MHz to 100's of GHz.

Once spin waves can be generated, for example using the STT in spin valves or MTJ's, their propagation characteristics can be manipulated to perform useful functions. The phase can be controlled to perform spin wave logic along a single channel of propagation [45] or using two channels with a delay as in a Mach Zehnder interferometer [46]. Magnonic crystals can be fabricated to perform frequency filtering [47]. The bandgaps and scattering properties of the magnonic crystals can be adjusted by an external magnetic field. Artificial and dynamic magnonic crystals can be fabricated allowing frequency transformation and reversal of the magnon propagation in a purely linear system [48]. Reducing the attenuation of spin waves is of great interest, such as proposals to increase the propagation length using the STT [49]. Control of spin wave attenuation has been demonstrated in confined structures [50]. Enhancement of the spin pumping efficiency by spin wave mode selection [51]. Unique propagation characteristics such as nonreciprocal propagation of surface spin waves can also add functionality to devices based on spin pumping [52]. The dynamic magnetization offers a richness of behavior that can lead provide functionality to spintronic devices that are not possible to achieve with non-magnetic means or can lead to detrimental behavior; therefore it is important to study in detail.

## 1.4 IMAGING OF MAGNETIC DYNAMICS

Spatial imaging of the magnetic dynamics in thin films and confined structures is essential for developing a complete understanding of the magnetization response of potential spintronic devices. The most widely used magnetic microscopy techniques today are time resolved scanning Kerr microscopy (TR-SKM) [53] and microfocus Brillouin light scattering spectroscopy ( $\mu$ -BLS) [54]. The spatial resolutions of these techniques are limited by the smallest beam spot size that can be achieved with the laser (about 250 nm). Other techniques that potentially offer higher spatial resolution include magnetic resonance force microscopy (MRFMR) [55] and time resolved X-ray magnetic circular dichroism (TR-XMCD) [56]. The main drawback with MRFMR is the fact that it probes localized modes due to the interaction of the tip with the sample and not the magnetic dynamics inherent in the sample. TR-XMCD while it can achieve spatial resolutions down to 20 nm and provide element specific magnetization states, the temporal resolution is limited to about 100 ps so it is unsuitable for studying dynamics in the GHz range. The ultimate spatial resolution imaging of single atom spin dynamics has been demonstrated using spin polarized scanning tunneling electron microscopy (SP-STM) [57], [58]. However, this method is mainly of academic interest since the measurements must take place at sub-Kelvin temperatures and in ultra-high vacuum. Magnetic dynamics are most commonly studied using purely electrical means with no spatial resolution. The frequency spectrum that can be obtained with such methods is highly detailed, but the challenge is to map the frequencies to specific modes which can be an error prone process. In the following discussion, we will review the recent results

that have been achieved with these methods, highlight their benefits and limitations, and explain why  $\mu$ -BLS is the ideal tool for the studies we wish to undertake.

Here we mainly want to focus on techniques that allow the spatial mapping of magnetic dynamics. However, we should at least briefly discuss some of the purely electronic techniques because they are so common in the field of magnetic dynamics. The detection scheme can either be electrical [25], [59], where current is passed through the magnetic layer to be probed, or inductive [60], [61], where the electrical signal in a waveguide couples to the magnetic layer through its oscillating Oersted field. In both configurations, one can measure the microwave absorption, which is similar to traditional FMR, or one can employ a broadband vector network analyzer operating in the GHz regime to perform (VNA-FMR), where the amplitude and phase of the signal are measured. Some notable recent results include the measurement of FMR in sub-100 nm spin valve structures [62] and spin Hall effect induced magnetization dynamics [63]. Chumak et al. have recently shown the ability to detect propagating spin waves using the inverse spin Hall effect [64], which is interesting because the signal measured is a DC voltage rather than a microwave response.

Recently, MRFMR has been employed to study edge modes in nanowires [65] and the magnetic dynamics around defect sites [66]. The technique employs an atomic force microscopy (AFM) system with a permanent magnet of nanoscale dimensions at the tip. The interaction of the tip with the magnetization in the film changes the resonant frequency allowing one to probe magnetic dynamics. The main drawback of this method is that the magnetic field of the tip creates a local environment in the sample and it is the

interaction of this local environment with the rest of the film that is probed rather than the magnetic dynamics inherent in the sample [67]. Therefore, while magnetic dynamics can still be probed with this technique, the results can be difficult to interpret. Spatial resolutions of about 100 nm have been obtained, but this is not much better than can be achieved with optical techniques.

One benefit of the TR-XCMD method is its ability to provide element specific information because it probes the magnetization of core level electrons. Therefore, in multilayer structures, it can probe the dynamics of different layers with different compositions. Also, the short wavelength of X-rays enables spatial resolution down to 20 nm [56]. This technique has been used to study magnetic vortex dynamics [68], current induced domain wall dynamics [69] and dynamics inside spin valve elements [70]. The frequency of excitations that can be probed is rather low in the sub GHz regime limited by the temporal resolution of about 100 ps due to the bunch size in synchrotron sources and jitter in the synchronization electronics. Although new ways have been developed to obtain higher temporal resolutions, the flux is too low to make them suitable for microscopy applications. It is however not suitable for probing the magnetic dynamics for electrons near the Fermi surface, which are relevant to spin transport effect [71].

While MRFMR and TR-XCMD have the advantage of having the highest spatial resolutions of the spatial mapping techniques, laser microscopy methods have contributed a far greater body of knowledge because such systems are highly versatile and relatively easy to construct. The temporal resolution of TR-SKM can reach the sub-picosecond timescale, making it suitable for measuring spin waves up to THz frequencies [72]. The

fact that the measurements can be done in the time-domain also makes it suitable for measuring the propagation of broadband spin wave packets and switching events. It should be noted that the timescale of dynamics that can be measured is also limited by the excitation scheme, which for the case of magnetic field pulses limits the timescale to about 50 ps. The study of faster dynamics requires optical excitation [72]. Measurements can be made in the frequency domain to study spin wave propagation if the photodetector signal is measured with a VNA or oscilloscope [73], [74]. The main drawback of this technique is that the excitation of the spin wave must always be phase locked to the laser probe, so it cannot probe incoherent phenomena such as thermally excited spin waves and chaotic signals from spin valves.

Like TR-SKM, the signal measured with  $\mu$ -BLS originates from the magneto-optic Kerr effect. The difference is that the  $\mu$ -BLS measurement is in its simplest form a frequency domain method, not a time domain method. Therefore, high frequency resolutions up to 50 MHz may be obtained. This makes it excellent for studying the eigenmodes of confined structures. Because the  $\mu$ -BLS signal is frequency filtered optically, incoherent excitations can be probed including thermal spin waves, as we will discuss more in Section 5.5. The ability to study thermal spin waves has made it possible to study modes of confined structures that would be extremely difficult to excite so they cannot be studied with TR-SKM [75]. In addition, the enhancement and suppression of thermal spin waves by the SHE induced STT has been studied using  $\mu$ -BLS [76]. Other interesting topics that have been studied include nonlinear effects [77–79], magnonic crystal band structures [80], and waveguide propagation [81–83]. It also serves as a

means to characterize materials for spintronic devices [84], [85]. Just as TRMOKE can be reconfigured as a frequency domain measurement, so can  $\mu$ -BLS be made into a time-domain method using a time-resolved photon-counting module for signal detection [86]. The timing resolution is limited to about 2 ns by the linewidth of the Fabry-Perot cavity. Phase resolution is also by interfering the scattered light with a coherent reference signal generated from either an electro-optic modulator or even a YIG crystal with an applied microwave signal [87–89].

I hope at this point the student is convinced that there is much to be gained from studying magnetic dynamics and properties and that  $\mu$ -BLS is an ideal tool for such investigations due to its sensitivity, high spatial resolution and flexibility in measurement. In the next chapter, we will begin the discussion of the theoretical background necessary to understand the measurements starting with a summary of ferromagnetism.

## Chapter 2: Magnetism

### 2.1 FERROMAGNETISM

Magnetic materials have been a source of curiosity since ancient times. Certain minerals, which are now known to contain iron oxide  $\text{Fe}_3\text{O}_4$ , were known to attract one another and pieces of iron. During the middle ages people found that a narrow magnet always pointed in the same direction in relation to the earth, which revolutionized navigation. At the time two ways were known to produce action at a distance: materials with electric charges were known to attract or repel one another depending if the charges were opposite or equal; and magnetic materials were known to possess poles that attract opposite poles and repel like ones. These forces seemed completely independent from one another because magnetic poles were not observed to interact with electrically charged objects. The relationship between magnetism and electricity was discovered in 1820 by Hans Christian Oersted when he noticed that a current carrying wire would deflect a compass needle perpendicular to the wire. Michael Faraday conceived of the concept of electric and magnetic fields and discovered electromagnetic induction in 1821. A few decades later, in 1864, Maxwell synthesized all of these findings into his equations of electrodynamics.

Materials that possess a magnetic moment in the absence of a magnetic field are called either ferromagnetic, meaning the total magnetic moment of a material is comprised of the sum of atomic moments all pointing in the same direction, or ferrimagnetic, meaning that the total magnetic moment is comprised of a sum of atomic

moments which may point in opposite directions but with a net magnitude in one direction. The distinction is not essential for what follows, and we will normally be concerned with ferromagnetism. For ferromagnetic materials, above a critical temperature, known as the Curie temperature, the thermal energy exceeds that of the potential energy gained by alignment and the magnetic moments point in random directions so that the material no longer has an overall magnetic moment.

The cause of ferromagnetism remained a mystery, however until the advent of quantum mechanics. Maxwell believed that the magnetization was due to microscopic internal currents. From the beginning ferromagnetism seemed to defy a classical explanation. After all, the magnetization of iron  $M = 1.76 \times 10^6$  A/m implies a circulating current density of the same magnitude. Moreover, Weiss's molecular field theory, which he developed to explain how ferromagnetic materials become nonmagnetic above the Curie temperature, postulated an internal field that was three orders of magnitude greater than the magnetization. Attempts to understand magnetism had a large role in the development of quantum mechanics. Neils Bohr in his doctoral dissertation written in 1911 explained why it was impossible according to the laws of classical physics for a collection of electrons to have a magnetic moment. The basic reason is that the thermodynamic state of any system does not depend on the magnetic field. From statistical mechanics, it is known that in thermal equilibrium a configuration with potential energy  $U$  occurs with a probability given by  $\exp(-U/k_B T)$ , where  $k_B$  is the Boltzman constant and  $T$  is the temperature. The Lorentz force law on an electron states

that  $\mathbf{F} = q(\mathbf{E} + \mathbf{v} \times \mathbf{B})$  and the work done to bring a charge to velocity  $v$  is  $\mathbf{v} \cdot \mathbf{F} = qvE$ , which does not depend on the magnetic. This negative result is probably one of the pieces of information that led him to develop the so called “old quantum theory” with the Bohr model of the hydrogen atom, where the electron angular momentum is quantized in multiples of  $\hbar$ ,  $|\mathbf{r} \times \mathbf{p}| = n\hbar$ .

The discovery of the intrinsic magnetic moment of the electron by Uhlenbeck and Goudsmit in 1925 and the theoretical understanding of its consequences proved to be the final pieces of fundamental physics missing in the understanding of ferromagnetism. Pauli proposed earlier in 1920, based on observations of the periodic table, that the electron has two internal states and that no two electrons can share the exact same state. Uhlenbeck and Goudsmit’s discovery showed that these two states are defined by angular momenta of  $\pm\hbar/2$ . Heisenberg showed in 1929 with his newly developed matrix mechanics that the large molecular field described in the Weiss theory was electrostatic in nature, arising from the overlap of the quantum mechanical wave functions of electrons and the Pauli exclusion principle. Heisenberg showed that the Hamiltonian representing the interaction of two neighboring atoms with total electron spins  $\mathbf{S}_i$  and  $\mathbf{S}_j$  is  $H = -2J \mathbf{S}_i \cdot \mathbf{S}_j$ , where  $J$  is the exchange constant, which is calculated from the overlap of electron wave functions and can either be positive, favoring the alignment of spins (ferromagnetic), or negative, favoring the anti-aligned spins (anti-ferromagnetic).

Because magnetic moments are associated with angular momentum, when one is perturbed in a static magnetic field it will precess much like a spinning top under the

influence of gravity. The fact that a magnetic moment has angular momentum and therefore precesses rather than simply rotate to align with a static field makes its behavior much different than that of an electric dipole, as will be discussed in the next section on magnetic dynamics. For now, we just wish to derive the precession frequency. The torque on a magnetic dipole in a magnetic field is given by  $\boldsymbol{\tau} = \boldsymbol{\mu} \times \mathbf{B}$ . The gyromagnetic ratio  $\gamma$  is defined as the ratio between the magnetic moment and the angular momentum. So we can write

$$d\boldsymbol{\mu}/dt = -\gamma \boldsymbol{\mu} \times \mathbf{B} , \quad (2.1)$$

which describes a precessing magnetic moment  $\boldsymbol{\mu}$ . The frequency of precession is  $\omega_p = \gamma B$ , which is known as the Larmor frequency.

The magnetic moment of an atom can arise from either the angular momentum of its electrons or from their intrinsic angular momenta. Atomic nuclei also possess magnetic moments, but they are about  $10^{-3}$  times smaller than those due to the electrons. The orbital magnetic moment can be understood in terms of an electron in a circular orbit around an atom with orbital radius  $\mathbf{r}$  and velocity  $\mathbf{v}$ . The magnetic dipole moment of a current loop is  $\boldsymbol{\mu} = I\mathbf{A} = -\frac{1}{2}e\mathbf{r} \times \mathbf{v}$ . In terms of the angular momentum  $\mathbf{L} = m_e \mathbf{r} \times \mathbf{v}$ , the moment is  $\boldsymbol{\mu} = -\frac{e}{2m_e} \mathbf{L}$ . For the case of an electron's orbital angular momentum

$\gamma_L = -\frac{e}{2m_e}$ , and  $\left| \frac{\gamma_L}{2\pi} \right| = 14 \text{ GHz/T}$ . The gyromagnetic ratio is twice as large for the

electron spin  $\left| \frac{\gamma_S}{2\pi} \right| = 28 \text{ GHz/T}$ . This fact was known empirically since Goudsmit and

Uhlenbeck's paper on electron spin, but was later proven by Dirac when he combined the theory of relativity with quantum mechanics.

The spin of electrons interacts more strongly with other electron spin moments and the angular moments interact most with other angular moments. This approximation is valid with spin orbit coupling is weak. This approximation is called L-S coupling or Russel-Sanders coupling [90]. Therefore, for a combination of spin and orbital angular momenta  $\boldsymbol{\mu} = \gamma_L(\mathbf{L} + 2\mathbf{S})$ . Here, the magnetic moment and total angular momentum  $\mathbf{J} = \mathbf{L} + \mathbf{S}$  are not necessarily parallel in the general case. However, only the component of magnetic moment that is parallel to  $\mathbf{J}$  has a well-defined measurable value. Therefore, we can write  $\boldsymbol{\mu} = \gamma\mathbf{J}$  where the gyromagnetic ratio is given in terms of the orbital motion gyromagnetic ratio and the Landé  $g$  factor  $\gamma = g\gamma_L$ . Then it can be shown using quantum mechanics that

$$g = \frac{3}{2} + \frac{S(S+1) - L(L+1)}{2J(J+1)} \quad (2.2)$$

For isolated atoms and ions, Eq. (2.2) allows one to accurately calculate the magnetic moment. The electronic ground states can be determined using Hund's Rules and the unpaired electrons give  $S$  and the total orbital angular momentum of the configuration is  $L$ . A completely filled shell, which has all electrons paired, has no angular momentum and therefore no magnetic moment. Magnetic moments in solids are often different from those that are calculated for isolated atoms and ions. For example, transition metals, which have unfilled d shells, show reasonable agreement for the electron spin  $S$ , but  $L$  is nearly 0. In such case, the orbital angular momentum is said to

be quenched. The cause of the quenching is the crystalline field, i.e. the strong electric field due to neighboring atoms, which distorts the orbitals of the outer electrons and removes the rotational symmetry of their electric potential so that angular momentum is no longer a conserved quantity.

The first attempts to measure the ratio  $\gamma = g\gamma_L$  between the angular momentum and magnetic moment nicely demonstrated the equivalence of the angular momentum associated with magnetism and mechanical angular momentum. Such measurements allow one to determine the magnitudes of the contributions of orbital and intrinsic angular momenta to the magnetization. The first successful measurement of  $\gamma$  was performed in 1915 by Barnett. He compared the magnetic field of a stationary rod to that of one rotating about its axis. Later, the inverse effect was demonstrated in by Einstein and de-Hass in Einstein's only experimental work. They showed that flipping the magnetization of a narrow ferromagnetic rod caused it to rotate about its axis. The relationship between rotation and magnetization is called the gyromagnetic effect. A weak coupling is required between the spin and orbital angular momenta and between the orbital angular momentum and the lattice for the change in angular momentum associated with magnetism to be equivalent to the change in rotational angular momentum. With such a coupling, the precessing angular momentum will gradually relax, transferring the momentum to the lattice. Additionally, the transfer of angular momentum to the environment, such as that transferred to the current in the electromagnet, should be negligible. For conditions of constant current in the coil, this is the case.

Another method of determining  $g$  involves perturbing the magnetization vector with a small oscillating magnetic field. A magnetic sample is placed in a static magnetic field and a small oscillating field perpendicular to the static field. The frequency is scanned and at a particular frequency, a resonance which would be given by the Larmor frequency for a sample in the shape of a narrow rod with the static field applied along its axis. This technique is known as ferromagnetic resonance (FMR). It was first performed by J. H. E. Griffiths in 1946. However, the correct values for  $g$  were determined by Kittel by taking into account the demagnetization field determined by the shape of the sample, which will be discussed later.

Interestingly, it turns out that the values of  $g$  measured from the FMR experiments and those measured from the gyromagnetic experiments are slightly different. The values for several ferromagnetic metals are shown below in Table 2.1 with  $g'$  denoting the gyromagnetic values and  $g$  denoting the FMR value. As mentioned previously, the orbital angular momentum is largely quenched for 3d so the values are close to 2, which is what one would expect for electron spin. However, the small differences in the measured  $g$  values are due to the small contribution of the orbital angular momentum. In the gyromagnetic measurement, the crystal is free to rotate, so all of the angular momentum is absorbed and contributes to the signal. In the FMR experiment, the crystal is rigid, so the spin angular momentum is absorbed, but the orbital angular momentum cannot be transferred to the crystal so it does not contribute to the signal. The deviation of the  $g$  values from the value expected from electron spin allows one to

calculate the relative contribution of the orbital angular momentum to the spin angular momentum to the magnetic moment. Following the argument above we have

$$\frac{1}{g'} = \frac{L+1/2 S}{J} \quad (2.3)$$

and

$$\frac{1}{g} = \frac{1/2 S}{J} \quad (2.4)$$

So that

$$g' = \frac{g}{g-1} \quad (2.5)$$

Denoting

$$\varepsilon = \frac{L}{S} \quad (2.6)$$

For small  $\varepsilon$

$$g' \simeq 2(1-\varepsilon) \quad (2.7)$$

and

$$g = 2(1+\varepsilon) \quad (2.8)$$

| Material    | $g$  | $g / (g - 1)$ | $g'$ | $\varepsilon(\%)$ from $g$ | $\varepsilon(\%)$ from $g'$ |
|-------------|------|---------------|------|----------------------------|-----------------------------|
| Fe          | 2.10 | 1.91          | 1.92 | 5                          | 4                           |
| Co          | 2.21 | 1.83          | 1.85 | 10.5                       | 7.5                         |
| Ni          | 2.21 | 1.83          | 1.84 | 10.5                       | 8                           |
| FeNi        | 2.12 | 1.90          | 1.91 | 6                          | 4.5                         |
| CoNi        | 2.18 | 1.85          | 1.84 | 9                          | 8                           |
| Supermalloy | 2.10 | 1.91          | 1.91 | 5                          | 4.5                         |

Table 2.1. Comparison between the  $g$  factors measured with FMR ( $g$ ) and those measured with the gyromagnetic effect ( $g'$ ).  
From Ref. [91].

After the introduction of FMR, interest was lost in gyromagnetic measurements of  $g$  because the mechanical measurements were more cumbersome and only suitable for studies of large samples. Recently however, with new developments in nanofabrication, micromechanical measurements of the gyromagnetic effect have permitted the study of the coupling of thin films and nanomagnets to the substrate, measuring torques that are a 10 orders of magnitude smaller than those measured in the Einstein-de Haas experiment. For example, the Einstein-de Haas effect was recently investigated experimentally for a permalloy film on a microcantilever [92] and mechanical torque due to spin flip on a torsion oscillator [93]. The effects of mechanical motion on spin current generation also have been studied theoretically [94–96], including most recently spin current generation by phonons [97].

Most isolated atoms in their ground states have magnetic moments due to unbalanced orbital and spin angular momentum. Hund's rules, which describe how electrons fill the ground states of isolated atoms, reveal that most atoms have unpaired spins and unfilled orbitals. The situation changes when atoms are brought into close proximity to form solids. The atomic orbitals hybridize and form bands, which decreases the magnetic moment in two ways: 1) the orbital angular momentum is quenched, because the crystal field does not have rotational symmetry and 2) the orbitals become bands which are spread out in space so the energy cost of pairing electrons in the same band is smaller than pairing electrons of opposite spin in the same orbital and the degeneracy of the orbitals is lifted. As a result most solids do not have magnetic moments. One type of material that form an exception are those with tightly bound 4f-orbitals, the hybridization is so weak that those levels do become spin polarized much as they do in the atomic state. In fact, there are only three ferromagnetic transition metals: Fe, Co, and Ni. These elements have strong hybridization but also strong exchange splitting.

There are two simplified models of ferromagnetism that are sometimes useful to give qualitative descriptions of various aspects of ferromagnetism. The first is the free-electron Stoner model. It was first proposed by Stoner [98] then independently by Slater [99]. The model assumes that the electron bands for spin-up and spin-down electrons have a relative shift in energy due to an exchange interaction but otherwise form parabolic free electron bands. In this picture, the conduction electrons can be divided into two channels with different resistances, which is useful for describing GMR. The other is

the s-d model, first introduced in Ref. [100], which divides the band into groups with mainly s-orbital characteristics to describe the conduction band and a band with d-orbital characteristics to describe localized states that contribute to the magnetization. The s-d model is often invoked when discussing STT with conduction electrons with angular momentum  $s$  interacting with local moments  $S$  with a Hamiltonian  $-JS \cdot s$ . Neither the itinerant Stoner model nor the localized s-d model provide sufficient basis for first principles calculations of magnetic properties. The actual situation is somewhere between the two situations. The fact that spin waves exist and the strong temperature dependence on the susceptibility support a localized model of magnetism. However, the fact that many materials have magnetizations of nonintegral numbers of Bohr magnetons supports the idea of nonlocalized bands carrying spin. A proper treatment of ferromagnetism can only be given by more complicated models, such as the local spin density approximation (LSDA).

The magnetic moments of the 3-d transition metals and their alloys do exhibit a simple behavior, as seen in the Slater-Pauling curve shown in Fig. **Error! Reference source not found.** According to Hund's rule for the filling of atomic orbitals, one would expect magnetic moments of 4, 3, and 2 Bohr magnetons per atom due to unpaired electrons for Fe, Co, and Ni, respectively. This doesn't include the additional contribution due to orbital angular momentum. Instead, the observed saturation magnetic moments correspond to only 2.2, 1.7, and 0.6 Bohr magnetons, respectively. If the saturation moments of metals from chromium to copper are plotted versus the number of electrons per atom, the slope is for the most part  $\pm 1$ . An extremely simplified band model of

magnetism in which the 4s and 3d bands are fixed for the 3d transition elements and their alloys can account for the main features of the Slater-Pauling curve. The curve can be explained by assuming that the d-shell is divided into an upper and lower part. The upper part holding 2.4 electrons per atom for each of the up and down bands and 3.6 electrons per atom for each band in the lower part. The 4s-shell holds about 0.6 electrons per atom. As the number of valence electrons decreases from about 10.6 halfway between pure Cu and Ni to 8.2 between Fe and Co, the magnetic moment increases from 0 to 2.4 Bohr magnetons. Then as the number of valence electrons decreases further, the upper part of the majority d-band is emptied until again there is no magnetic moment with 5.8 valence electrons per atom, just past Cr.

We should now comment on the different fields used to describe magnetism. The magnetic field  $\mathbf{B}$  is typically divided into two components, the  $\mathbf{H}$  field, which is the field due to external electric currents and the magnetization field  $\mathbf{M}$ , which is due to microscopic quantum mechanical currents and electron spin that are properties of the material itself. Maxwell's form of Ampère's Law with no time dependent electric field can be written  $\nabla \times \mathbf{B} = \mu_0 \mathbf{J}_{tot}$ , where  $\mathbf{J}_{tot}$  can be divided into two contributions: one that dissipates unless driven by a voltage  $\mathbf{J}_f$ , which is often called the free current, and one that remains indefinitely in a static field due to the dissipationless circulation of electrons in materials  $\mathbf{J}_m$ , which is known as the bound current. The fields  $\mathbf{M}$  and  $\mathbf{H}$  are defined as averaged over some volume, which is large enough that  $\int \nabla \cdot \mathbf{J}_m dV = 0$  so the magnetization can be defined as  $\nabla \times \mathbf{M} = \mathbf{J}_m$ . Then  $\mathbf{H}$  is defined as  $\mathbf{H} = \mathbf{B} / \mu_0 - \mathbf{M}$  so

that  $\nabla \times \mathbf{H} = \mu_0 \mathbf{J}_f$ . Now it remains to be shown how  $\mathbf{M}$  relates to the dipole moment per unit volume of the material.

If we think of a microscopic magnetic moment in the material as a small current loop, in the limit that the radius of the loop becomes infinitesimal, the magnetic field at the center is given by

$$\mathbf{B}(\mathbf{r}) = \frac{\mu_0}{4\pi} \left( \frac{3\mathbf{r}(\mathbf{r} \cdot \boldsymbol{\mu}) - r^2 \boldsymbol{\mu}}{r^5} + \frac{8\pi}{3} \boldsymbol{\mu} \delta(\mathbf{r}) \right) \quad (2.9)$$

Now if we consider the  $\mathbf{H}$  field without any free charges  $\nabla \times \mathbf{H} = 0$  so we can define a potential, much like the electric potential, such that  $\mathbf{H} = \nabla \varphi_m$ . Therefore, the  $\mathbf{H}$  field can be considered to be due to magnetic dipoles formed by magnetic charges. The preferred definition of a magnetic moment has changed over time. Before the 1930s, textbooks defined the moment using magnetic poles. Since then, most have defined it in terms of Ampèrian currents; however, the concept of magnetic poles is still extremely useful for analyzing fields in materials. The difference between the  $\mathbf{H}$  and  $\mathbf{B}$  fields are illustrated in Figure 2..

The field in the limit that the charges are brought together is given by

$$\mathbf{H}(\mathbf{r}) = \frac{1}{4\pi} \left( \frac{3\mathbf{r}(\mathbf{r} \cdot \boldsymbol{\mu}) - r^2 \boldsymbol{\mu}}{r^5} - \frac{4\pi}{3} \boldsymbol{\mu} \delta(\mathbf{r}) \right) \quad (2.10)$$

Now  $\mathbf{M} = \mathbf{B} / \mu_0 - \mathbf{H} = \boldsymbol{\mu} \delta(\mathbf{r})$ . Thus, the magnetization field is given by the magnetic dipole moment per unit volume under the condition that the volume is small enough and also large enough that the distribution of dipole moments is smooth and uniform.

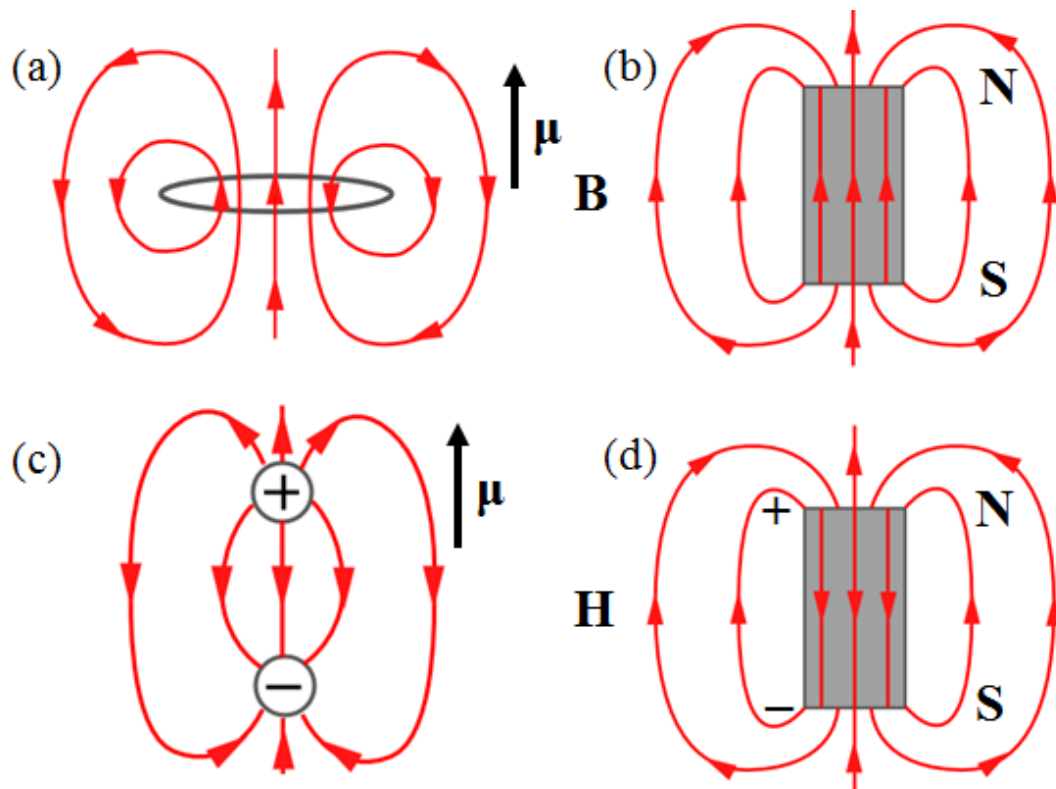


Figure 2.1. Comparison of the magnetic fields  $\mathbf{B}$  and  $\mathbf{H}$ .  
 In the presence of magnetic materials the  $\mathbf{B}$  and  $\mathbf{H}$  are different. The  $\mathbf{B}$  field resembles the field surrounding a magnetic dipole formed by a loop of current. The  $\mathbf{H}$  field resembles the field that would surround two magnetic charges forming a dipole.

It is useful to further divide  $\mathbf{H}$  into two parts: one part due to the arrangement of magnetic moments in the material  $\mathbf{H}_d$  and an external field  $\mathbf{H}_{ext}$  (i.e., the field that would be present if the material were removed). The field due to the magnetization is called the demagnetizing field because it points in the opposite direction of the magnetization and serves to decrease the field felt by a magnetic moment inside the material. In this respect it is exactly like the depolarizing field in dielectrics. This field is important to consider when calculating the forces on a magnetic moment inside a

material. The demagnetizing field is only easy to calculate for ellipsoidal samples where the magnetization happens to be uniform and the demagnetizing field also happens to be uniform. Then the internal magnetic field can be written as

$$\mathbf{H} = \mathbf{H}_{ext} - \vec{\vec{N}}\mathbf{M} , \quad (2.11)$$

where the demagnetization matrix  $\vec{\vec{N}}$  can be diagonalized with the axes of the ellipse as the principle axes so that  $N_{xx} + N_{yy} + N_{zz} = 1$ . Tables for these values for ellipses with different aspect ratios are available in many text book on magnetism, see for example [101].

For our purposes, we are concerned with the internal magnetic field of a ferromagnetic strip when the magnetic field is applied along the width of the stripe. The shape is a rectangular prism with thickness much smaller than the width, which is much smaller than the length. If the applied magnetic field is great enough, the magnetization throughout the film can be assumed to point in the direction of the applied field. Then the demagnetizing field assumes the form

$$N_{zz}(z) = \frac{1}{\pi} \left( \arctan \left( \frac{L}{2z+w} \right) - \arctan \left( \frac{L}{2z-w} \right) \right) . \quad (2.12)$$

The internal field is relatively uniform at the center of the stripe, but reduced from its external value, as shown in Figure 2.2. The field decreases at the edges, because spin wave modes confined to this region of reduced field can exist and are called edge modes, as will be discussed later in Section 2.4. If the field is not large enough to saturate the magnetization, there will be regions at the edges of the strip where the field is totally

excluded. In those regions, the direction of the magnetization will point in a direction determined by anisotropy or some initial conditions that can be ignored for the center of the strip. The magnetization at the unsaturated edges will point along the length of the stripe, but which direction along the length would be determined from the initial conditions.

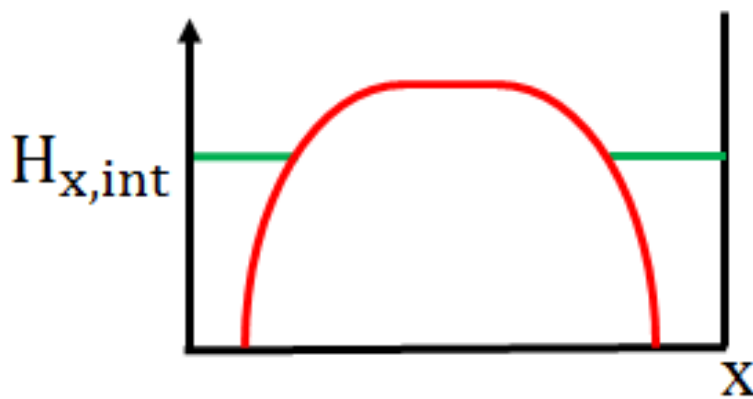


Figure 2.2. Illustration showing the nonuniform internal magnetic field of a stripe magnetized along its width.

When a magnetic field is applied to a ferromagnet the magnetization does not always align itself with the field immediately, as was discussed above for the case of the edges of a stripe. The magnetization may be pinned to a particular direction due to the shape of the sample or crystal directions and require energy to rotate. Furthermore, the sample may consist of domains that align at different strengths of the applied field. Therefore, the material exhibits hysteresis. The width of the hysteresis loop is called the coercivity. Magnetic materials can be divided into two categories, soft and hard, depending on whether they have a coercivity that is small or large, respectively. Hard magnetic materials are ideal for making permanent magnets. Soft magnetic materials are

best for applications in transformers, magnetic memory, and RF devices where the magnetization must be easily switched. It is a testament to the rapid technological progress that began in the beginning of the 1900's that the difference between soft and hard magnets went from less than two orders of magnitude up to eight. With the softest magnetic materials having coercivities of 0.1 A/m and the hardest with coercivities as high as 10 MA/m. For our experiments we use an especially soft ferromagnet known as permalloy ( $\text{Ni}_{80}\text{Fe}_{20}$ ). Because it is soft, the magnetization points in the direction determined by the magnetic field not by any crystal direction, so the dynamic properties are relatively easy to analyze.

## 2.2 MAGNETIC DYNAMICS

Even though quantum mechanics is necessary to explain why materials can possess magnetic moments, a classical description of magnetic moment and field suffices to describe many of the effects that we are concerned with in this research. The reason is that a large number of electrons and atomic sites can be averaged over for the relatively large wavelengths we are concerned with in our studies. Classically, local magnetic moments in a magnetic field behave like spinning tops in a gravitational field.

The equation of motion for a uniform magnetization in a ferromagnet was first proposed by Landau and Lifshitz [102].

$$\frac{\partial \mathbf{M}}{\partial t} = -\gamma \mathbf{M} \times \mathbf{H}_{eff} \quad (2.13)$$

This equation describes a precessing magnetization much like Eq. (2.1) describes a precessing magnetic moment, and is referred to as the Landau-Lifshitz equation or LL equation for short. In general,  $\gamma$  is a tensor, but for most materials it can be considered a scalar quantity. Note that the length of  $\mathbf{M}$  is conserved, and the tip of the magnetization vector will trace out a circle with an angular frequency of  $\omega_p = \gamma H_{eff}$ . Also note that the field acting on the magnetization is an effective magnetic field  $\mathbf{H}_{eff}$ . The effective magnetic field is given by the variational derivative of the free energy with respect to the magnetization

$$\mathbf{H}_{eff} = -\frac{\delta W}{\delta \mathbf{M}} \quad (2.14)$$

The free energy is the total energy in the magnetic system minus the energy required to assemble the magnetization configuration, which is specific to the sample shape. For a sample with no anisotropy the effective magnetic field is simply  $\mathbf{H}_{eff} = \mathbf{H}_{ext} - \mathbf{H}_d$ .

Now we wish to calculate the response of the magnetization to a small harmonic magnetic field. Let the magnetic field and the magnetization be written as the sum of static and oscillating parts.

$$\begin{aligned} \mathbf{H}_{eff} &= \mathbf{H}_0 + \mathbf{h}_{ac} \\ \mathbf{M} &= \mathbf{M}_0 + \mathbf{m}_{ac} \end{aligned} \quad (2.15)$$

Furthermore, assume that the oscillating parts are much smaller than the static parts. Then plugging Eq. (2.15) in to the LL Eq. (2.13), meaning that the static magnetization points in the direction of the static magnetic field. Neglecting the second order terms we can obtain the linearized LL equation

$$\frac{\partial \mathbf{m}_{ac}}{\partial t} + \gamma \mathbf{m}_{ac} \times \mathbf{H}_0 = -\gamma \mathbf{M}_0 \times \mathbf{h}_{ac} \quad (2.16)$$

Writing  $\mathbf{h}_{ac} = \text{Re}[\mathbf{h} \exp(i\omega t)]$ . Because the equation of motion Eq. (2.16) is linear, we also have  $\mathbf{m}_{ac} = \text{Re}[\mathbf{m} \exp(i\omega t)]$ . Substituting these forms into Eq. (2.16) gives the linearized LL equation

$$i\omega \mathbf{m} + \gamma \mathbf{m} \times \mathbf{H}_0 = -\gamma \mathbf{M}_0 \times \mathbf{h} \quad (2.17)$$

From the linearized LL equation, we can obtain the high frequency susceptibility tensor defined by  $\mathbf{m} = \vec{\chi} \mathbf{h}$ . Solving Eq. (2.16) gives

$$\vec{\chi}(\omega) = \begin{pmatrix} \chi & i\chi_a \\ -i\chi_a & \chi \end{pmatrix} \quad (2.18)$$

where denoting  $\omega_M = \gamma M_0$  and  $\omega_H = \gamma H_0$ .

$$\begin{aligned} \chi &= \frac{\omega_M \omega_H}{(\omega_H^2 - \omega^2)} \\ \chi_a &= \frac{\omega_M \omega}{(\omega_H^2 - \omega^2)} \end{aligned} \quad (2.19)$$

The susceptibility tensor  $\vec{\chi}$  calculated above is known as the Polder tensor. The Polder tensor can be diagonalized with a circularly polarized basis  $h_{\pm} = h_x \pm ih_y$  and  $m_{\pm} = m_x \pm im_y$ . Then the diagonal elements are given by

$$\chi_{\pm} = \chi \pm \chi_a = \frac{\omega_M}{\omega_H \mp \omega} \quad (2.20)$$

So we see that only the right circularly polarized component  $m_+$ , which is excited by the component  $h_+$  depends resonantly on applied static field  $H_0$  or the frequency of excitation  $\omega$ .

The LL equation, Eq. (2.13), does not include dissipation. It describes a magnetization vector that precesses with the same amplitude indefinitely, in reality, the precession amplitude decreases and the magnetization relaxes to its equilibrium position as energy is converted into heat. There are many ways to include damping phenomenologically in the equations of motion. For most purposes, the damping should not change the magnitude of the magnetization vector. Also, a convenient policy is to use a form that does not depend strongly on frequency in the regime being measured. Probably the most common way to introduce damping that meets these requirements is the form proposed by Gilbert, which is a friction like term, proportional to the speed of precession and directing the magnetization to its equilibrium direction parallel to the effective magnetic field, as illustrated in Figure 2.3.

The LL equation with the Gilbert term is commonly referred to as the Landau-Lifshitz-Gilbert (LLG) equation and is given by

$$\frac{\partial \mathbf{M}}{\partial t} = -\gamma \mathbf{M} \times \mathbf{H}_{eff} + \frac{\alpha}{M} \mathbf{M} \times \frac{\partial \mathbf{M}}{\partial t} . \quad (2.21)$$

Linearizing the LLG equation for small oscillating fields as we did for the LL equation gives

$$i\omega \mathbf{m} + \gamma \mathbf{m} \times \mathbf{H}_0 + \frac{i\alpha\omega}{M_0} \mathbf{m} \times \mathbf{M}_0 = -\gamma \mathbf{M}_0 \times \mathbf{h} , \quad (2.22)$$

which is equivalent to Eq. (2.17) with the substitution  $\omega_H \rightarrow \omega_H + i\alpha\omega$ . Therefore, we can make the same substitution in the susceptibility relations in Eqs. (2.19) and (2.20) to account for damping.

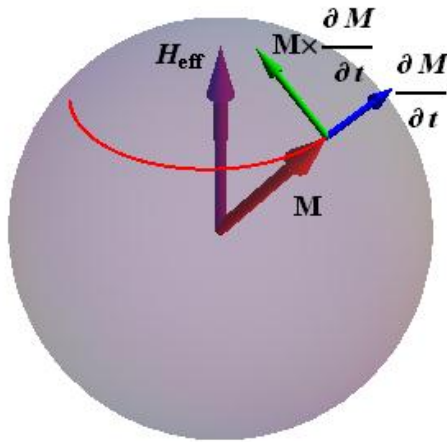


Figure 2.3. Illustration of magnetization precession.

### 2.3 SPIN WAVES

In the previous section, we considered the case when the magnetization of the entire sample precesses in phase. But if we consider magnetic moments localized to small volumes of a sample, they are not rigidly coupled and therefore do not need to precess in phase. When the phase relation between localized magnetic moments can be described by a wave with oscillatory spatial and temporal dependence, the excitation is called a spin wave, which is illustrated in Figure 2.4. The quantum of a spin wave is known as a magnon. The local magnetic moments interact through a dipolar coupling and also exchange coupling. For an isotropic crystal, the exchange coupling is isotropic, but the

dipolar coupling is always anisotropic with uniaxial symmetry determined by the direction of the applied magnetic field.

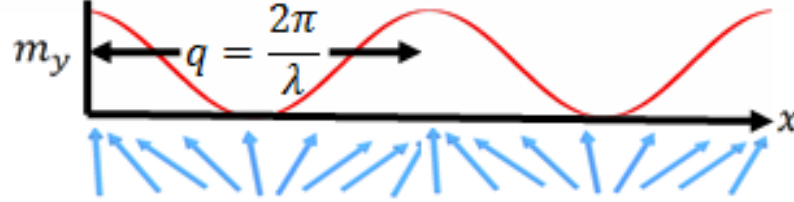


Figure 2.4. Illustration of a spin wave.

First, we consider spin waves propagating in a bulk material where we do not consider the sample shape or boundary conditions. Assuming plane waves,  $\mathbf{m}(\mathbf{k}) = \mathbf{m} \exp(-i\mathbf{k} \cdot \mathbf{r})$  and  $\mathbf{h}(\mathbf{k}) = \mathbf{h} \exp(-i\mathbf{k} \cdot \mathbf{r})$ . The exchange interaction can be taken into account with the field

$$\mathbf{h}_{ex} = -qk^2 \mathbf{m} \quad (2.23)$$

The dipolar coupling is accounted for with the field

$$\mathbf{h}_{dip} = -\frac{1}{k^2} \mathbf{k} (\mathbf{m} \cdot \mathbf{k}) \quad (2.24)$$

Substituting  $\mathbf{h} = \mathbf{h}_{dip} + \mathbf{h}_{ex}$  into Eq. (2.22) and taking the applied static field and equilibrium magnetization to be along  $\mathbf{z}_0$ , the equation of motion is

$$i\omega \mathbf{m} + (\omega_H + i\alpha\omega) \mathbf{m} \times \mathbf{z}_0 + \omega_M \mathbf{z}_0 \times (\mathbf{h}_{ex} + \mathbf{h}_M) = 0 \quad (2.25)$$

The dispersion relation can be obtained from Eq. (2.25) as

$$\omega^2 = A_k^2 - |\mathbf{B}_k|^2 \quad (2.26)$$

where

$$\begin{aligned} A_k &= \omega_H + \eta k^2 + \frac{1}{2} \omega_M \sin^2 \theta_k \\ |B_k| &= \frac{1}{2} \omega_M \sin^2 \theta_k \end{aligned} \quad (2.27)$$

Here,  $\eta = \gamma M_0 q$  and the angle  $\theta_k$  is the angle of the wave vector with respect to the direction of the static magnetic field  $z_0$ . As for the uniform precession case, we can account for damping by substituting  $\omega_H \rightarrow \omega_H + i\alpha\omega$ .

$$\frac{m_y}{m_x} = -i \frac{A_k + |B_k|}{A_k - |B_k|} = -i \left( 1 + \frac{\omega_M \sin^2 \theta_k}{\omega_H + \eta k^2} \right)^{-1/2} \quad (2.28)$$

For a ferromagnetic slab, translational symmetry and modes exist that are localized to the surface. The spin wave modes of a ferromagnetic slab of material were first analyzed by Damon and Eshbach [103]. In their analysis, they focus on long wavelength spin waves where exchange can be neglected. The electromagnetic boundary conditions are included by solving Maxwell's equations in the magnetostatic limit.

In the magnetostatic limit  $\nabla \times \mathbf{H} = 0$  so there is a potential such that  $\mathbf{H} = \nabla \varphi$ . We also have  $\nabla \cdot \mathbf{B} = \nabla \cdot (1 + \chi) \mathbf{H} = 0$ . Then for a slab with susceptibility of the form in Eq. (2.18). We obtain what is known as the Walker equation

$$(1 + \chi) \left[ \frac{\partial^2 \varphi}{\partial x^2} + \frac{\partial^2 \varphi}{\partial y^2} \right] + \frac{\partial^2 \varphi}{\partial z^2} = 0 . \quad (2.29)$$

Assume that the film is surrounded by material with no permeability in the frequency range of concern. The surroundings could be air or some other insulator. Denoting the

potential inside the film as  $\varphi_i$  and that outside the film as  $\varphi_e$ , the electromagnetic boundary conditions that the normal components of  $\mathbf{B}$  and the tangential components of  $\mathbf{H}$  are continuous across the boundary, gives the boundary conditions for the magnetic potential

$$\varphi_i = \varphi_e, \quad (1 + \chi) \frac{\partial \varphi_i}{\partial x} + i\chi_a \frac{\partial \varphi_i}{\partial y} = \frac{\partial \varphi_e}{\partial x} \quad (2.30)$$

If we assume wavelike solutions in all directions inside the film and outside the film, the potential decays exponentially with distance from the film surface, the dispersion relation for bulk spin waves is recovered, however, while the angle  $\theta_k$  still refers to the angle of propagation with respect to the direction of the magnetic field as shown in Eq. (2.31), the values are quantized due to the quantization of the out-of-plane wave vector  $k_x$ .

$$\sin^2(\theta_k) = (k_x^2 + k_y^2) / (k_x^2 + k_{\parallel}^2) \quad k_{\parallel}^2 = k_y^2 + k_z^2 \quad (2.31)$$

The wave vector component in the thickness direction  $k_x$  is obtained by solving the transcendental equation

$$2k_x \cot(2k_x L) = \frac{1}{k_{\parallel}} \left( k_x^2 - k_{\parallel}^2 + (\omega_H / \omega_M) (k_x^2 + k_{\parallel}^2) (k_y / k_z)^2 \right) \quad (2.32)$$

These solutions form a band with frequencies in the range  $\omega_H < \omega < \sqrt{\omega_H(\omega_H + \omega_M)}$ .

The group velocities of these waves are negative, which is why they are referred to as magnetostatic backward volume waves (MSBVWs).

Damon and Eshbach discovered that another solution exists where the wave vector decays exponentially away from the surface inside the film. In contrast to the

volume mode solutions, only one surface wave solution is permitted. The solution only exists for spin waves propagating within a certain range of angles from the direction perpendicular to the magnetic field, that is for, angles such that

$$\varphi_k \equiv \left| \frac{k_y}{k_z} \right| > \tan^{-1} \left( \sqrt{\frac{\omega_H}{\omega_M}} \right) \equiv \varphi_{crit} \quad (2.33)$$

As the angle of propagation goes from  $\varphi_k = \frac{\pi}{2}$  to  $\varphi_k = \varphi_{crit}$ , the solutions lose their surface character and become degenerate with the MSBVW band. For spin waves propagating perpendicular to the magnetic field, the solutions are called magnetostatic surface waves (MSSWs) because they are localized to the surface. The MSSW mode is localized to the top or bottom surface of the film depending on the sign of  $k_y$ . The dispersion relation is given by

$$\omega^2 = \omega_H (\omega_H + \omega_M) + \frac{\omega_M^2}{4} \left( 1 - e^{-2|k_y|L} \right) \quad (2.34)$$

This formula is accurate for long wavelength spin waves in thin films such that  $kL \ll 1$ .

When we are concerned with modes that have nodes in the film thickness direction exchange cannot be neglected, which makes the analysis much more difficult. There are two methods by which the spin wave spectrum in the regime where both dipolar and exchange effects must be included: one involves the magnetostatic potential and the other uses the tensorial Green function method. The benefit of the Green function method is that approximate dispersion relations can be obtained in closed form that

provide some physical intuition. The complete analysis can be found in a paper by Kalinikos and Slavin [104]. The equation of motion except that the effects of the

$$\ddot{\mathbf{P}}\mathbf{m}(z) = -i\frac{\omega}{\omega_M}\ddot{\mathbf{T}}\mathbf{m}(z) + \int_{-L/2}^{L/2}\ddot{\mathbf{G}}_{xy}(z, z')\mathbf{m}(z')dz' \quad (2.35)$$

where

$$\begin{aligned} \ddot{\mathbf{P}} &= \left( -\alpha \frac{\partial^2}{\partial z^2} + \alpha k_{\parallel}^2 + \frac{\omega_H}{\omega_M} \right) \begin{pmatrix} 1 & 0 \\ 0 & 1 \end{pmatrix} \\ \ddot{\mathbf{T}} &= \begin{pmatrix} 0 & -1 \\ 1 & 0 \end{pmatrix} \end{aligned} \quad (2.36)$$

and the dipole interaction tensor  $\ddot{\mathbf{G}}_{xy}$  is a bit too complicated to be reproduced here but can be found in Ref. [104]. With exchange being considered the equation of motion is a second order differential equation in the  $z$  direction and requires taking into account the exchange boundary conditions [105].

$$\begin{aligned} \frac{\partial m_x}{\partial z} + \eta \cos(2\theta) m_x &= 0 \\ \frac{\partial m_y}{\partial z} + \eta \cos^2(\theta) m_y &= 0 \end{aligned} \quad (2.37)$$

Here we just quote the result for the case of unpinned surface spins. Below is the relation we use for most of our calculations.

$$\omega_n^2 = \left( \omega_H + \eta\omega_M (k_{\parallel}^2 + k_z^2) \right) \left( \omega_H + \eta\omega_M (k_{\parallel}^2 + k_z^2) + \omega_M F_m \right) \quad (2.38)$$

where

$$F_m = \left( 1 - P_m \cos^2(\varphi) \right) + P_m \left( 1 + \frac{\omega_M}{\omega_H + \eta\omega_M (k_{\parallel}^2 + k_z^2)} (1 - P_m) \sin^2(\varphi) \right) \quad (2.39)$$

and

$$P_m = \left(\frac{k_y}{k}\right)^2 - \left(\frac{k_y}{k}\right)^4 \frac{2}{k_y L} \left(1 - (-1)^n \exp(-k_y L)\right). \quad (2.40)$$

For spin waves propagating perpendicular to the applied field with exchange neglected, Eq. (2.38) simplifies to Eq. (2.34) derived by Damon and Eshbach. For  $k_y L \ll 1$ , the expression for  $P_m$  simplifies considerably to

$$\begin{aligned} P_m &= k_y L / 2, \quad n=0 \\ P_m &= (k_y L / n\pi)^2, \quad n=1, 2, 3\dots \end{aligned} \quad (2.41)$$

Eq. (2.41) is sufficiently accurate for most of our results because the films are 10-100 nm-thick and wave vectors are about  $1 \mu\text{m}^{-1}$ .

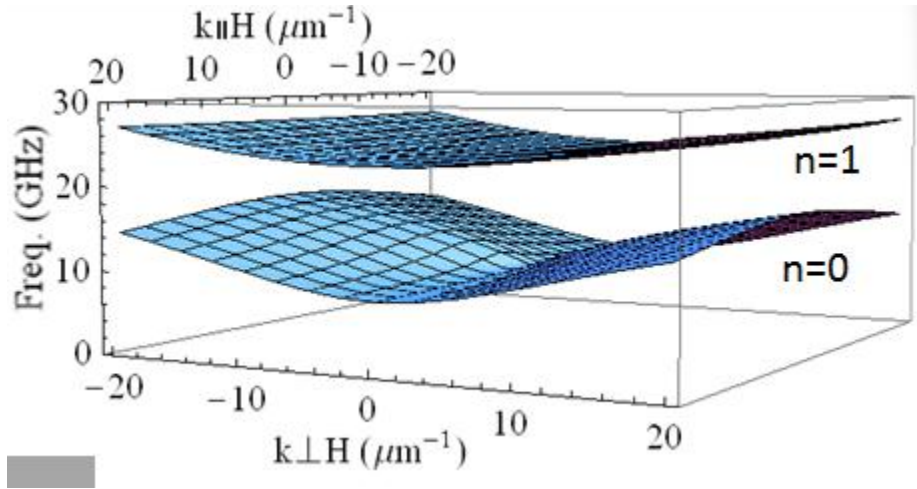


Figure 2.5. Calculated dispersion relation for spin waves in a thin film of permalloy.

## 2.4 SPIN WAVES IN CONFINED STRUCTURES

The spin wave modes that propagate in confined structures made of thin ferromagnetic films differ from those in continuous films in that the in-plane wave

vectors are quantized and the nonuniform internal magnetization can permit modes that are localized near the edges of the structure. The tensorial Green function method is also useful for obtaining approximate dispersion relations and mode structures in this case.

Guslienko et al. [106] showed that the dipolar interactions in a rectangular element impose boundary conditions on the eigenfunctions of the element that are much like the exchange boundary conditions

$$\left. \frac{\partial m_n(z)}{\partial z} \pm d(p)m_n(z) \right|_{z=\pm L/2} = 0 \quad (2.42)$$

where  $n$  is the mode index and

$$d(p) = \frac{2\pi}{p(1 + 2\ln(1/p))} . \quad (2.43)$$

Here  $p = L/w$  is the ratio of the thickness to the width of the element in the quantization direction. For small  $p$ , which is the case for our structures, the spins at the boundary are effectively pinned, and the eigenfunctions are sinusoidal functions quantized with an effective width that approaches the real width of the element as  $p \rightarrow 0$ .

$$k = \frac{2\pi(n+1)}{w_{eff}}, \quad n = 0, 1, 2, \dots \quad (2.44)$$

$$w_{eff} = \frac{d(p)}{d(p) - 2}$$

These results were derived for infinite stripes with the magnetic field applied along the stripe axis; however, as Gubbiotti pointed out [107], the boundary conditions are the same as long as the stripe width is longer than about  $1\mu\text{m}$ .

## 2.5 EXCITING MAGNETIC DYNAMICS

The excitation of spin waves by the Oersted field of an antenna operating at microwave frequencies is described by Kalinikos in Ref. [108]. Here we will just discuss the issues relevant to our experiments, which all involve films magnetized in-plane and parallel to the antenna. The representation below relates the Cartesian components of the Fourier transform of the antenna field to the circular components of the magnetization. The form of the equation is simplified compared to that given by Kalinikos. Here we do not sum over the thickness modes because they are well separated for the thin films that we use. We also restrict our attention only to waves propagating perpendicular to the magnetic field. Furthermore, we consider the magnetization to be uniform across the film thickness. This assumption is considered accurate for long wavelength surface waves where the in-plane wavelength is much greater than the film thickness. Furthermore, the formula given in the paper does not account for waves localized to the surface. With these assumptions, Eq. (36) in Ref. [108] is simply

$$\mathbf{m}(\mathbf{r}, t) = e^{i\omega t} \frac{1}{2\sqrt{\pi}} \sum_p \int_{-\infty}^{\infty} (\chi_{p,x} h_x(k_y) + \chi_{p,y} h_y(k_y)) e^{-ik_y y} dk_y \quad (2.45)$$

where the matrix elements of the susceptibility are given by

$$\begin{aligned} \chi_{p,x} &= (-1)^p \frac{\omega_M \left( \omega + (-1)^p (\Omega_k + \omega_M P_{nm}) - i\omega_{rk} \right)}{\omega_k^2 + \omega_{rk}^2 - \omega^2 + 2i\omega\omega_{rk}} \\ \chi_{p,y} &= \frac{i\omega_M \left( \omega + (-1)^p (\Omega_k + \omega_M - \omega_M P_{nm}) - i\omega_{rk} \right)}{\omega_k^2 + \omega_{rk}^2 - \omega^2 + 2i\omega\omega_{rk}} \end{aligned} \quad (2.46)$$

where  $\omega_k$  is the frequency calculated from the dispersion relation reproduced below, and  $\omega_{rk}$  is the relaxation frequency taking into account the damping parameter of the film  $\alpha$ .

$$\omega_k^2 = (\Omega_k + \omega_M - \omega_M P_{nn}) (\Omega_k + \omega_M P_{nn} \sin^2(\theta)), \quad \theta = \frac{\pi}{2} \quad (2.47)$$

Here,  $\Omega_k = \omega_H + \eta k^2$  and  $P_{nn}$  is given by Eq. (2.41).

## Chapter 3: Brillouin Light Scattering

### 3.1 BRILLOUIN LIGHT SCATTERING SPECTROSCOPY

Brillouin Light Scattering spectroscopy (BLS) is an inelastic light scattering technique that can be used to probe wavelike excitations in materials in the GHz frequency range. When light impinges on a material, it induces a polarization given by

$$\mathbf{P}(\mathbf{r}, t) = \epsilon_0 \vec{\chi} \mathbf{E}_i(\mathbf{r}, t) \quad (3.1)$$

where the susceptibility is related to the dielectric function by  $\epsilon_0(\vec{\mathbf{I}} + \vec{\chi}) = \vec{\epsilon}$ . The scattered light then satisfies

$$(\nabla^2 + k_s^2) \mathbf{E}_s(\mathbf{r}, \omega_s) = -\frac{\omega_s}{\epsilon_0 c^2} \mathbf{P}(\mathbf{r}, \omega_s) \quad (3.2)$$

It should be noted that the incident and scattered electric fields expressed in the equations above exist inside the material. One must consider the Fresnel equation to convert the back and forth between the beams outside the material to those inside. Consider a material with a dielectric function that has a constant part and a fluctuating part to its dielectric function

$$\vec{\epsilon}(\omega, \mathbf{k}) = \vec{\epsilon}_r + \delta \vec{\epsilon} \sin(\omega t - \mathbf{k} \cdot \mathbf{r} + \varphi) \quad (3.3)$$

The light wave can be written as  $\mathbf{E}_i(\mathbf{r}, t) = \mathbf{E}_i \sin(\omega_i t - \mathbf{k}_i \cdot \mathbf{r})$ . Then the scattered light is the sum of three beams

$$\begin{aligned} \mathbf{E}_{elastic} &\propto \mathbf{E}_i \sin(\omega_i t - \mathbf{k}_i \cdot \mathbf{r}) \\ \mathbf{E}_{Stokes} &\propto \mathbf{E}_i \sin((\omega_i - \omega) t - (\mathbf{k}_i - \mathbf{k}) \cdot \mathbf{r}) \\ \mathbf{E}_{anti-Stokes} &\propto \mathbf{E}_i \sin((\omega_i + \omega) t - (\mathbf{k}_i + \mathbf{k}) \cdot \mathbf{r}) \end{aligned} \quad (3.4)$$

The scattered beams shifted in frequency can be thought of as sidebands arising from the mixing of the oscillating incident light with the oscillating dielectric function, and they satisfy the conservation of energy and momentum

$$\begin{aligned}\omega_s &= \omega_i \pm \omega \\ \mathbf{k}_s &= \mathbf{k}_i \pm \mathbf{k}\end{aligned}\tag{3.5}$$

The process described above is inelastic light scattering. It can be used to probe wavelike excitations in a material that modify the dielectric function. Similar to an inelastic collision between two masses, inelastic light scattering describes a process wherein the incoming light gains or loses energy and momentum equal to the energy and momentum taken from or transferred to the material. In other words, the light is shifted up or down in frequency and changes direction relative to elastically scattered light, as shown in Figure 3.1.

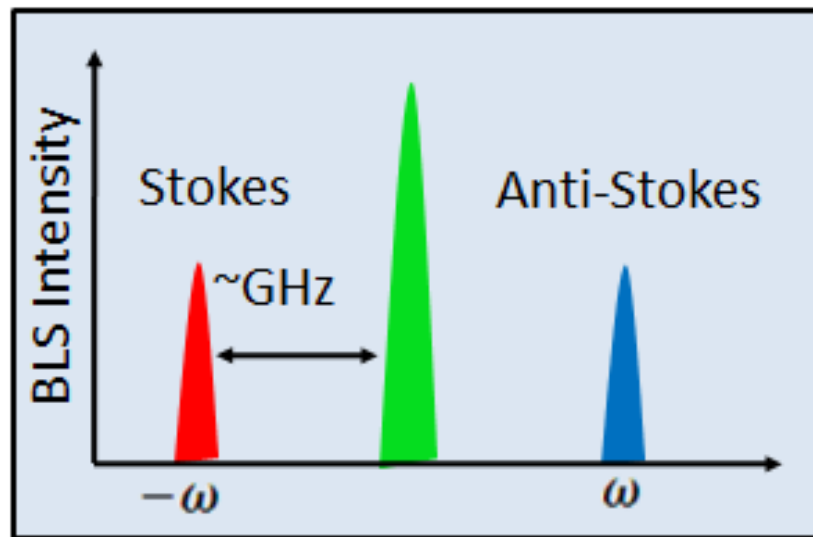


Figure 3.1. Sketch of Brillouin light scattering spectrum.

The unshifted line is called the Rayleigh line, the upshifted line is the anti-Stokes line, and the downshifted line is called the Stokes line. A helpful way to remember which is Stokes and anti-Stokes is that the anti-Stokes line requires that the excitation be populated, which is only true for excitations with frequencies such that  $\hbar\omega \ll k_B T$  where  $T$  is the relevant temperature for the excitation. Stokes did Raman experiments at room temperature therefore he only studied the downshifted line, which we now call the Stokes line. A discussion of the naming of the lines can be found in [109].

Inelastic light scattering techniques in the frequency domain are divided into two classes: BLS and Raman spectroscopy. The primary distinction is the instrumentation required to separate the shifted light from the elastically scattered light. A diffraction grating is used in Raman spectroscopy, which limits the frequency shifts it can distinguish to about 5 - 4000  $\text{cm}^{-1}$ . BLS requires a Fabry-Perot interferometer and is required to study shifts smaller than 5  $\text{cm}^{-1}$ . The Fabry-Perot interferometer will be described in more detail in Section 4.1 where the Sandercock interferometer is discussed. Some useful energy conversions are shown in Table 3.1.

Many different kinds of excitations in materials can lead to fluctuations in the dielectric constant and thus to inelastic light scattering. In fact, in solid state systems, it is pretty safe to say that every effect is coupled to every other effect to some degree. For elastic excitations (i.e., phonons) the coupling constants are called elasto-optic or Pockels coefficients. The magnetic excitations are coupled less strongly through the magnetic

permeability than through the dielectric function with magneto-optic effects due to spin-orbit interactions.

| Notes               | Wavenumber<br>( $\text{cm}^{-1}$ ) | Frequency<br>(THz)    | Wavelength<br>(m)     | Temperature<br>(K) i.e., $k_B T$ | Electron<br>Volts (meV) | Joules (J)             |
|---------------------|------------------------------------|-----------------------|-----------------------|----------------------------------|-------------------------|------------------------|
| 1 $\text{cm}^{-1}$  | 1.00                               | $3.00 \times 10^{-2}$ | $1.00 \times 10^{-2}$ | 1.44                             | 0.12                    | $2.00 \times 10^{-23}$ |
| 1 THz               | $3.34 \times 10$                   | 1                     | $2.00 \times 10^{-4}$ | 0.02                             | 4.14                    | $6.63 \times 10^{-22}$ |
| Green Laser         | $1.88 \times 10^5$                 | 599.98                | $5.32 \times 10^{-7}$ | $2.70 \times 10^5$               | $2.33 \times 10^3$      | $3.73 \times 10^{-19}$ |
| Room<br>Temperature | $2.01 \times 10^2$                 | 6.04                  | $4.96 \times 10^{-5}$ | 295                              | 25                      | $4.01 \times 10^{-21}$ |

Table 3.1. Equivalent energies.

### 3.2 MAGNETO-OPTIC KERR EFFECT

The modification of the dielectric tensor by a magnetic field is known as a magneto-optic effect. Magneto-optic effects that are linear in the magnetic field are divided into two categories: the Faraday effect, which describes the effect of the magnetic field on light transmitted through a material; and the magneto-optic Kerr effect (MOKE), which describes the effect of the magnetic field on light reflected from a surface. Magneto-optic effects that are even functions of the magnetization include the Voigt and Cotton-Mouton effects.

For now we will just take for granted that the magneto-optic effects lead to off-diagonal elements in the dielectric tensor to determine the effects on common measurements. When the magnetic field is applied along the z direction, the dielectric tensor has the following form

$$\boldsymbol{\varepsilon} = \begin{pmatrix} \varepsilon_{xx} & \varepsilon_{xy} & 0 \\ -\varepsilon_{yx} & \varepsilon_{yy} & 0 \\ 0 & 0 & \varepsilon_{zz} \end{pmatrix} \quad (3.6)$$

The refractive index is defined as  $n \equiv c\mathbf{k} / \omega$ . The wave propagating in the medium is then described by  $\mathbf{E}(r, t) = \mathbf{E}_0 e^{i\omega(\mathbf{n}\cdot\mathbf{r}/c - t)}$  where  $\mathbf{n}(\omega)$  must be determined. The solution is given by Fresnel's equations, which directly follows from inserting the form for the electric field in the Helmholtz equation

$$\nabla^2 \mathbf{E} - \nabla(\nabla \cdot \mathbf{E}) = -\frac{1}{c} \frac{\partial^2 \mathbf{D}}{\partial t^2} \quad (3.7)$$

Using  $\mathbf{D} = \boldsymbol{\varepsilon}\mathbf{E}$  we obtain the Fresnel equation

$$(n^2 \vec{I} - \vec{\epsilon} - \mathbf{n} \otimes \mathbf{n}) \cdot \mathbf{E} = 0 \quad (3.8)$$

Here  $\mathbf{n} \otimes \mathbf{n}$  denotes the outer product of the index of refraction with itself, i.e. the tensor with elements  $n_i n_j$ . MOKE measurements can be divided into three classes depending on the relationship between the scattering plane of the light and the magnetization of the film, as shown in Figure 3.2.

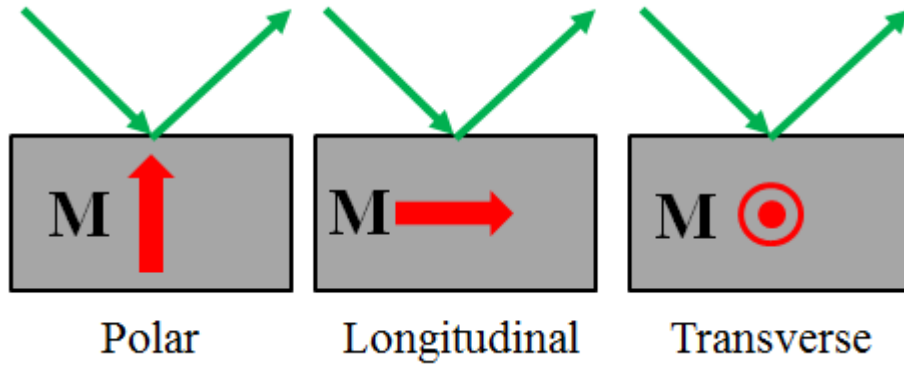


Figure 3.2. The three different configurations of MOKE measurements.

Consider light at normal incidence  $\mathbf{n} = n\hat{z}$  the solutions to the Fresnel equation is then

$$\text{Det} \begin{pmatrix} n^2 - \epsilon_{xx} & -\epsilon_{xy} & 0 \\ \epsilon_{xy} & n^2 - \epsilon_{xx} & 0 \\ 0 & 0 & -\epsilon_{zz} \end{pmatrix} = 0 . \quad (3.9)$$

So

$$n_{\pm}^2 = \epsilon_{xx} \pm i\epsilon_{xy} . \quad (3.10)$$

The linearly polarized light becomes elliptically polarized upon reflection and the plane of polarization is rotated, as illustrated in Figure 3.3. To determine the reflection

coefficients we consider the continuity of the electric and magnetic fields at the boundary of the medium.

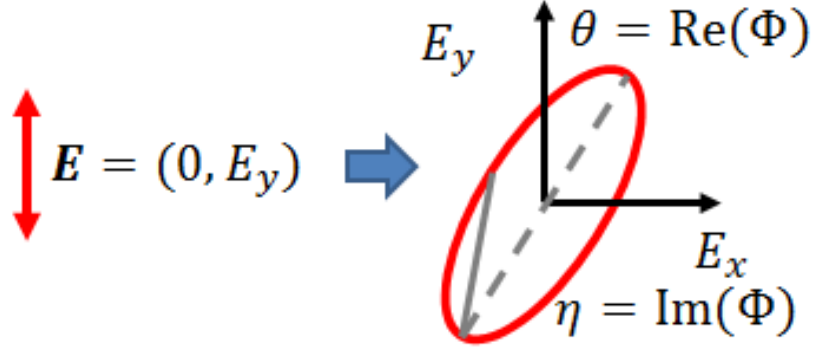


Figure 3.3. Illustration of MOKE on linearly polarized light.

For most materials, the Kerr rotation and Kerr ellipticity are less than  $1^\circ$ , and for normal incidence the Kerr rotation angle and ellipticity can be expressed as

$$\Phi = \theta_k + i\eta_k \approx -i \frac{n_0 \bar{n} Q}{\bar{n}^2 - n_0^2} \quad (3.11)$$

where  $Q \equiv i\varepsilon_{xy} / \varepsilon_{xx}$  is the Voigt parameter.

We can see how magneto-optic effects that rotate the plane of polarization of light might arise by considering the Lorentz force acting on a free electron. This analysis dates back to Bequerel in 1897. The motion of electrons in the presence of a static magnetic field  $\mathbf{B}$  in the presence of a harmonic electric field  $\mathbf{E}(\mathbf{r}, t) = \mathbf{E}(\mathbf{r})e^{-i\omega t}$  is given by the Lorentz force law

$$m_e (\ddot{\mathbf{r}} + \omega_0^2 \mathbf{r}) = -q\mathbf{E}e^{-i\omega t} - q\dot{\mathbf{r}} \times \mathbf{B} \quad (3.12)$$

where  $q$  is the absolute value of the electron charge,  $m_e$  is the mass of the electron, and  $\omega_0$  is the resonant frequency of the electron in its potential well. Assuming the steady state condition where the position takes on the time dependence of the driving field, the motion of the electron is described by  $\mathbf{r} = \mathbf{r}_0 e^{-i\omega t}$

$$(\omega^2 - \omega_0^2)\mathbf{r} - i\omega \frac{q}{m_e} (\mathbf{r} \times \mathbf{B}) = -\frac{q}{m_e} \mathbf{E} \quad (3.13)$$

Letting  $\mathbf{B} = B_0 \hat{\mathbf{z}}$  and considering that the polarization is defined by

$$\mathbf{P} = \frac{1}{V} \sum \mathbf{p} = -Nq\mathbf{r} \quad (3.14)$$

The relationship between the polarization and electric field can then be written as

$$\frac{m_e}{Nq^2} \begin{pmatrix} \omega^2 - \omega_0^2 & -i\omega\omega_c & 0 \\ i\omega\omega_c & \omega^2 - \omega_0^2 & 0 \\ 0 & 0 & \omega^2 - \omega_0^2 \end{pmatrix} \begin{pmatrix} P_x \\ P_y \\ P_z \end{pmatrix} = \begin{pmatrix} E_x \\ E_y \\ E_z \end{pmatrix} \quad (3.15)$$

where  $\omega_c = qB/m_e$  is the cyclotron frequency. The susceptibility matrix  $\tilde{\chi}$  defined by

$\mathbf{E} = \tilde{\chi}\mathbf{P}$  is then

$$\tilde{\chi} = \frac{Ne^2/m_e}{(\omega_0^2 - \omega^2)^2 - \omega^2\omega_c^2} \begin{pmatrix} \omega_0^2 - \omega^2 & i\omega_c\omega & 0 \\ -i\omega_c\omega & \omega_0^2 - \omega^2 & 0 \\ 0 & 0 & \omega_0^2 - \omega^2 \end{pmatrix} \quad (3.16)$$

The dielectric tensor which is defined by  $\mathbf{D} = \epsilon_0 \mathbf{E} + \mathbf{P} = \epsilon_0 (1 + \tilde{\chi}) \mathbf{E} = \epsilon_0 \tilde{\epsilon}_r \mathbf{E}$

$$\hat{\epsilon}_r = \begin{bmatrix} 1 & 0 & 0 \\ 0 & 1 & 0 \\ 0 & 0 & 1 \end{bmatrix} + \begin{bmatrix} \chi_{xx} & \chi_{xy} & 0 \\ \chi_{yx} & \chi_{yy} & 0 \\ 0 & 0 & \chi_{zz} \end{bmatrix} = \begin{bmatrix} \epsilon & i\epsilon_i & 0 \\ -i\epsilon_i & \epsilon & 0 \\ 0 & 0 & \epsilon_{zz} \end{bmatrix} \quad (3.17)$$

with

$$\begin{aligned}
\varepsilon &= 1 + \frac{\omega_p^2(\omega^2 - \omega_0^2)}{(\omega^2 - \omega_0^2)^2 - \omega^2\omega_c^2} \\
\varepsilon_i &= \frac{\omega_p^2\omega\omega_c}{(\omega^2 - \omega_0^2)^2 - \omega^2\omega_c^2} \\
\varepsilon_{zz} &= 1 + \frac{\omega_p^2}{\omega^2 - \omega_0^2}
\end{aligned} \tag{3.18}$$

where  $\omega_p = \sqrt{Nq^2 / m_e \varepsilon_0}$  is the plasma frequency.

Now in a ferromagnetic material, we can write the dielectric tensor in terms of the internal magnetic field and magnetization using  $\mathbf{B} = \mu_0(\mathbf{H} + \mathbf{M})$  where

$\mathbf{M} = (M_x, M_y, M_z)$  and  $\mathbf{H} = (0, 0, H_z)$ .

$$\frac{m_e}{Nq^2} \begin{pmatrix} \omega_0^2 - \omega^2 & -i \frac{\omega q \mu_0}{m_e} (H + M_z) & i \frac{\omega q \mu_0}{m_e} M_y \\ i \frac{\omega q \mu_0}{m_e} (H + M_z) & \omega_0^2 - \omega^2 & -i \frac{\omega q \mu_0}{m_e} M_x \\ -i \frac{\omega q \mu_0}{m_e} M_y & i \frac{\omega q \mu_0}{m_e} M_x & \omega_0^2 - \omega^2 \end{pmatrix} \begin{pmatrix} P_x \\ P_y \\ P_z \end{pmatrix} = \begin{pmatrix} E_x \\ E_y \\ E_z \end{pmatrix} \tag{3.19}$$

Then the susceptibility can be written as the sum of two parts, one linear in the magnetization components and one quadratic.

$$\begin{aligned}
\chi_L &= A(\omega^2 - \omega_0^2) \begin{pmatrix} 1 & -iC(H + M_z) & -iCM_y \\ iC(H + M_z) & 1 & -iCM_x \\ iCM_y & iCM_x & 1 \end{pmatrix} \\
\chi_{NL} &= A \begin{pmatrix} -C^2 M_x^2 & C^2 M_x M_y & -C^2 (H + M_z) \\ C^2 M_x M_y & -C^2 M_y^2 & C^2 M_y (H + M_z) \\ -C^2 M_x (H + M_z) & -C^2 M_y (H + M_z) & -C^2 (H + M_z)^2 \end{pmatrix}
\end{aligned} \tag{3.20}$$

with  $A = \frac{1}{(\omega_0^2 - \omega^2) \left( (\omega_0^2 - \omega^2)^2 + (M_x^2 + M_y^2 + (H + M_z)^2) \right)}$ .

Now the part of the dielectric tensor that is linear in the magnetization is

$$\hat{\epsilon}_r = n^2 \begin{pmatrix} 1 & -iQM_z & iQM_y \\ iQM_z & 1 & -iQM_x \\ -iQM_y & iQM_x & 1 \end{pmatrix} \quad (3.21)$$

where  $n$  is the complex index of refraction and  $Q$  is the Voigt constant.

$$n^2 = 1 + \frac{\omega_p^2}{(\omega^2 - \omega_0^2)^2} \quad (3.22)$$

$$Q = \frac{\omega q \mu_0}{m_e} \frac{n^2 - 1}{n^2}$$

The depth-dependence of the MOKE coefficients is also a factor that should be considered for quantitative comparison of the signal and to consider nonuniform magnetization in the film thickness direction. As the light passes through the ferromagnetic layer, its amplitude is diminished and its phase is delayed. Hence, the MOKE signal depends on the depth at which the light was scattered. For films with thickness  $d$  greater than the probing depth of the light, i.e.,  $d > \lambda / (4\pi \text{Im}(n_z))$ , the depth dependence is modeled well by the function

$$P_{s/p}(z) = P_{s/p}(0) \exp(-4\pi i n_z z / \lambda) \quad (3.23)$$

where  $P_{s/p}(0)$  is the polar MOKE signal at the surface of the film [110].

| Wavelength<br>(nm) | Material | Diagonal<br>component of $\epsilon$ | Off-diagonal<br>component of $\epsilon$ , K |
|--------------------|----------|-------------------------------------|---|
| 514.5 nm           | Fe       | -0.4+16.4i                          | 0.31+0.24i                                  |
| (2.41 eV)          | Co       | -9.5+14.2i                          | 0.22+0.11i                                  |
| Ar Ion Laser       | Ni       | -8.0+12.4i                          | 0.055+0.022i                                |

Table 3.2. Magneto-optic coefficients for iron, cobalt and nickel at 514 nm. The on diagonal components are taken from [111]. The off diagonal components are obtained from [112].

### 3.3 BRILLOUIN LIGHT SCATTERING FROM SPIN WAVES

In the previous section, we discussed how the magnetization modifies the scattered light from a ferromagnet in the static case. The same effect is responsible for the BLS signal from spin waves, which is just a temporal and spatial variation of the magnetization. From a classical standpoint which is valid when the magnon populations are large, variations in the dielectric function of a medium will modulate the scattered light mixing the incident signal with that of the spin waves. Two sidebands result in addition to the unmodulated light which are commonly referred to as the Stokes and anti-Stokes intensities

The first observation of surface magnetostatic modes using BLS was in the ferromagnetic semiconductor EuO by Grünberg and Metawe [113]. Depending on the scattering geometry, they observed the surface mode to be either on the Stokes side or

anti-Stokes side. The appearance of the surface mode on only one side of the spectrum was a consequence of the nonreciprocal propagation characteristics of the MSSW. The exchange interaction across thin spacers between ferromagnetic metals has attracted much interest due to the GMR effect. BLS has been used to study the effect in multilayer films. For example, Fe/Cr/Fe by Demokritov et al. [114].

Numerical models to calculate the spin wave intensity described by Cochran [115], [116] and Giovanni [117]. Relation between the Kerr angle was also expressed by Buchmeier [118]. Hamrle showed an analytical calculation of the BLS intensity from spin waves using the MOKE effect [119]. Calculation can allow one to make quantitative statements about the energy carried in each mode or isolate the dynamics of a single ferromagnetic layer in a multilayer structure.

There are four reasons that the Stokes to anti-Stokes ratio can be different from unity. First, the difference can be due to the thermal population factors. It is more probable to create a magnon (Stokes process) than to destroy one (anti-Stokes) because the magnon must already be thermally excited to be destroyed. The ratio is given by  $\exp(\hbar\omega/k_B T)$ , so a room temperature with frequency in the GHz regime, the ratio is nearly one. This difference is often used to measure temperature in Raman measurements, where the frequency shifts are three orders of magnitude larger than for BLS measurements. This effect is present in measurements from any excitation including magnons and phonons. Second, the quadratic MOKE coefficients may lead to asymmetry. On the Stokes side, the interference between the quadratic and linear terms is

destructive and the intensity is proportional to  $|K - nSG|^2$ . On the anti-Stokes side the interference is constructive so the intensity is proportional to  $|K + nSG|^2$ . In ferromagnetic metals such as Permalloy the third effect is dominant. For these first two effects, a reversal of the magnetic field does not cause a reversal in the ratios.

The third effect applies to MSSW waves, which are localized near the surfaces. Because the side on which the surface wave is localized changes when the magnetization is reversed, the effect on the Stokes-anti-Stokes ratio also reverses. Surface wave localization does not however explain the asymmetric intensities observed for very thin films for small wave vectors in the in-plane direction. A fourth reason was explained by Camley et al. [120], and is due to the off diagonal components of the magnetization correlation functions.

$$I = |B|^2 r_{yy} S_{yy}(Q_{\parallel}, \Omega) + r_{xx} S_{xx}(Q_{\parallel}, \Omega) + 2\text{Re}(r_{yx} S_{yx}(Q_{\parallel}, \Omega)) \quad (3.24)$$

where  $r_{xx}$ ,  $r_{yy}$ , and  $r_{yx}$  are reflectivities defined in [121],  $S_{xx}$ ,  $S_{yy}$ , and  $S_{yx}$  are the spin correlation functions of the dynamic components. The off-diagonal component  $S_{yx}$  changes sign if  $\Omega$  changes sign. Therefore, if it contributes positively to the intensity on the Stokes side, it contributes negatively on the anti-Stokes side.

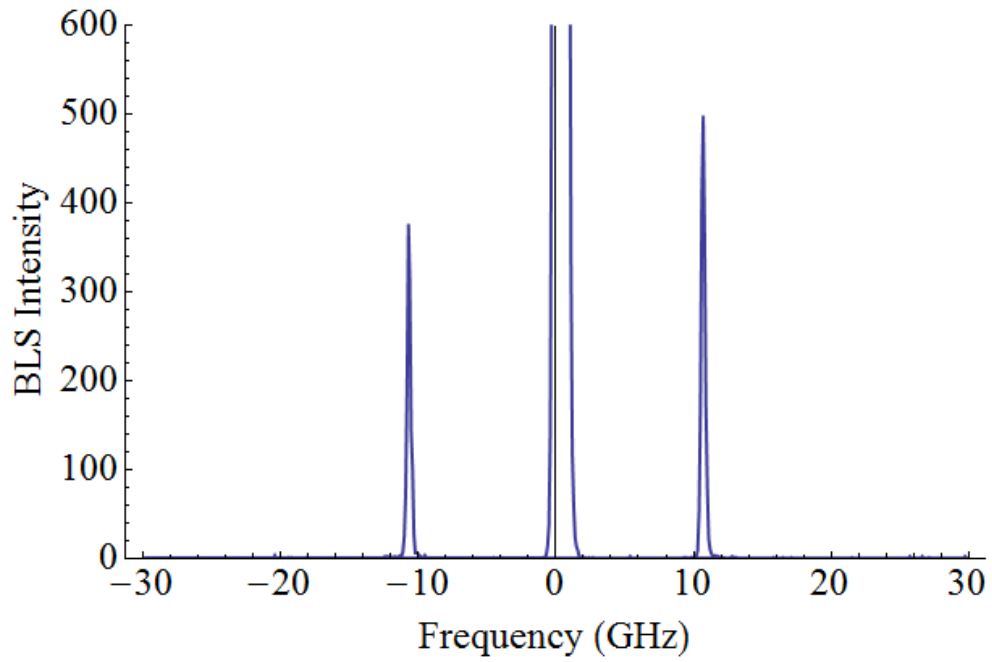


Figure 3.4. BLS spectrum from spin waves excited at 10.2 GHz. The Stokes / anti-Stokes asymmetry is visible due to the off diagonal components of the spin correlation functions.

## Chapter 4: Experimental Methods

### 4.1 MICRO-BLS SYSTEM

#### Overview

The first demonstration of a  $\mu$ -BLS system was presented in 2004 by Demidov and Demokritov who were then working with Prof. Hillebrands [122]. It consists of the usual equipment for performing BLS on opaque materials, including a Sandercock multi-pass tandem interferometer for high contrast, a polarizer to separate the magnon scattered light from the rest, and continuous wave laser. A scanning laser microscopy setup was added to obtain a spatial resolution of the spin wave intensity measurement of about 300 nm. To correct for beam drift, which cannot be completely eliminated at such small length scales, optical feedback using a CCD is required to correct the beam position. A schematic of the  $\mu$ -BLS system is shown below in Fig. 4.1.

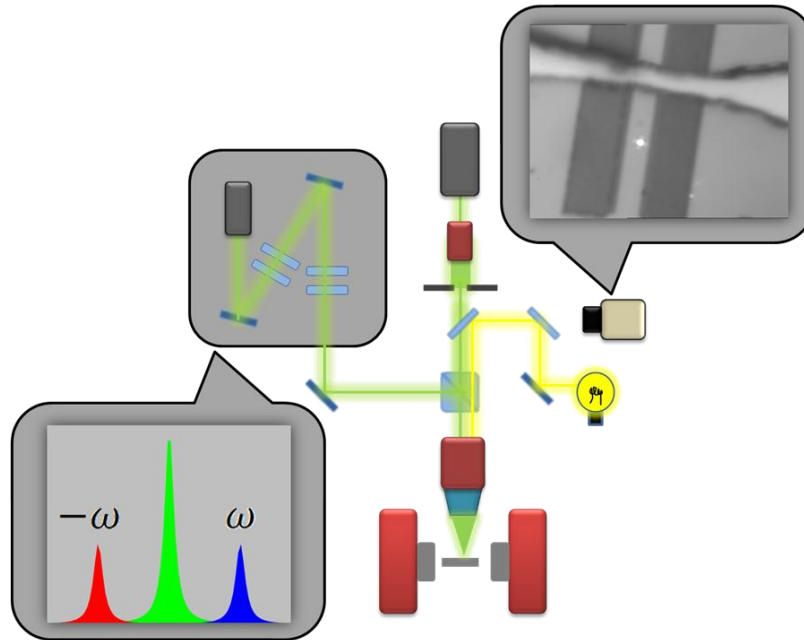


Figure 4.1. Schematic of the  $\mu$ -BLS setup.

The scanning laser microscopy setup consists of a 3-axis nanopositioning stage, a CCD camera, and a long working distance 100x microscope objective. The working distance of the microscope objective is typically a few mm to allow easy access for electrical connections such as wires and microwave probes.

Numerous effects related to spin wave propagation and in ferromagnetic confined structures have been studied with  $\mu$ -BLS, such propagation and scattering in waveguides [83], [123–125], bandgaps in magnonic crystals [47], [126], [127], harmonic generation of spin waves [77], [128], spin transfer torque in nanopillars [129] and due to the spin Hall effect [32], [50], [76]. Time [130] and phase [131] resolution have also been demonstrated, although these capabilities have not yet been implemented in our system.

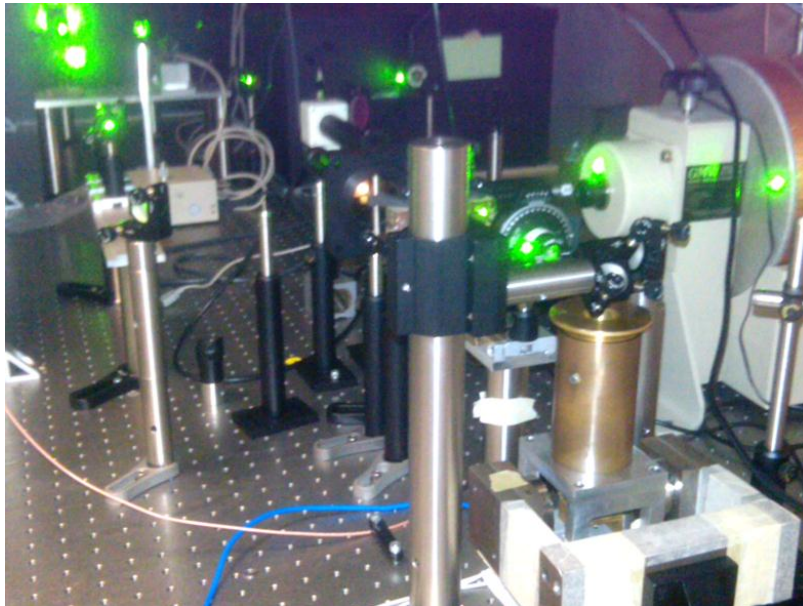


Figure 4.2. Photograph of our  $\mu$ -BLS system. In this configuration we are using a permanent magnet. The microscope objective is held in the brass tube and the sample is underneath between the poles of the magnet.

## **Control Software**

One of the most critical components of the  $\mu$ -BLS system is the control software. It is responsible for ensuring that all of the devices involved in the scan function together without mishap for measurements that can last several days. Over the course of such long scans problems may arise that could compromise the quality of the data unless they are resolved. For example, small temperature variations in the laboratory may cause the optical components to shift ever so slightly causing the beam to deviate from its intended position by an amount larger than the beam spot size. While proper construction can prevent drifts on the order of microns, active feedback is necessary for long measurements with 100 nm spatial resolution. Other problems may arise if the interferometer is not able to maintain alignment or if one of the connected devices encounters a problem in applying a parameter. When a problem is encountered the control program will pause the scan and solve it programmatically if possible, and if not it will notify the operator that action needs to be taken. When the problem is resolved, the scan can resume.

A graphical description of the control system is shown below in Figure 4.3. Each device is controlled by a plugin, which communicates with the main BLS Scan Loader plugin and occasionally with other plugins. The plugins send messages back and forth to share data and coordinate the scan, pausing when a problem is encountered and resuming the scan when ready. After the user starts the scan, the scan loader plugin notifies the device plugin loaded first that it should apply the first parameter on its list to the device it controls. When the device plugin has applied the parameter it notifies the scan loader plugin that it is ready, and the scan loader program tells the next device plugin on the list to apply the parameter on its list. This process repeats until it reaches the bottom level of the scan and it is ready to collect a BLS spectrum. At this point, the interferometer

control program is requested to begin taking a BLS spectrum. After a specified time, the spectrum collection is stopped, and the data is saved to a file. The scan loader program then instructs the lowest level device plugin to apply the next parameter on its list. When the parameter list of the lower level plugin is exhausted, the next parameter of the next higher level device plugin is applied. This process repeats to complete the scan with every combination of parameters desired. During the course of the scan, a monitor plugin may detect a problem with the scan and request that the scan be paused. All devices are notified that they should be paused and they reply back when they are in a suitable state. After the problem is resolved, the device plugins are notified that they should resume the scan. When all device plugins have replied that they are ready to resume the scan, the scan is resumed.

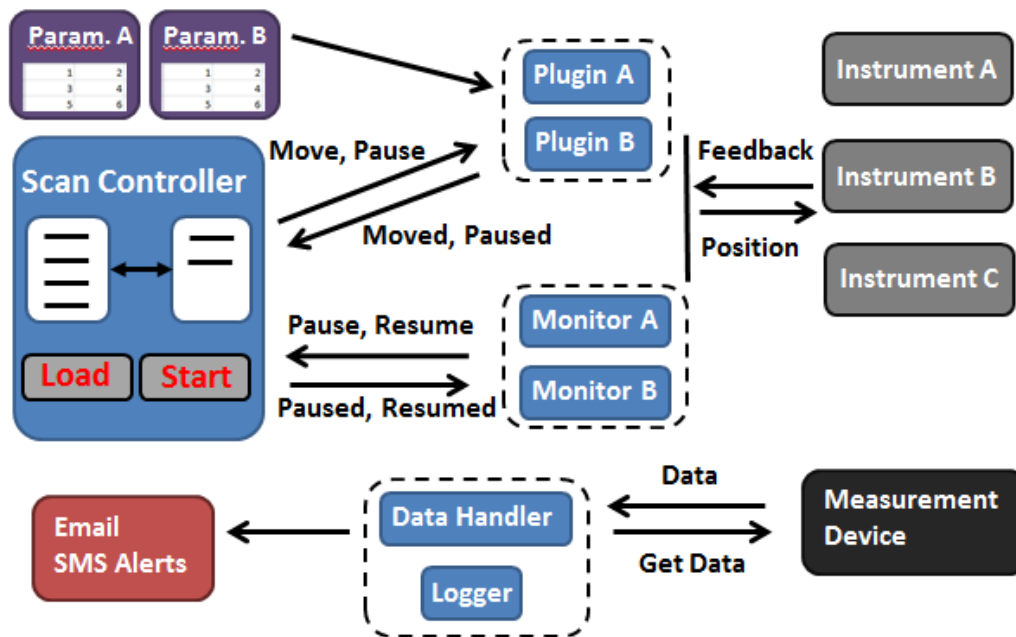


Figure 4.3. Schematic of the  $\mu$ -BLS software control system.

The main benefit of the plugin architecture is that the scan can be easily reconfigured. The scan order can be rearranged by simply loading the plugins in a different order. Adding a new device is simple because all device plugins are basically the same. All plugins perform the same function: apply a parameter to a device when told to do so, resolve any issues that may arise in applying that parameter, and notify the scan loader that the parameter has been applied so it can move to the next device. Therefore, all the user should have to do is supply the drivers for the device. The basic plugin template can be copied and modified with the appropriate device drivers. The plugin template automatically provides the communication functionality and the ability to respond to certain events. Because each device should respond differently to different events, adding a new device requires some changes to the control loop. So adding a new device requires slightly more work than just adding the device drivers, but with the plugin architecture adding a new device to the scan is as simple as possible. New devices can also be connected to different computers as long as they are connected on a network because the messaging system can operate over a network.

Perhaps the most important monitor plugin is the position monitor, which ensures that the beam spot remains in the correct position throughout the scan. Without active feedback thermal expansion in the frame of the microscope may cause the beam to shift position and possibly go out of focus. Correction of the in-plane drift is accomplished by comparing the position of a region of interest on the sample with the position of the laser beam. The drift correction procedure is illustrated in Figure 4.4. If the stage is set to a position at which the distance between the beam spot and the region of interest are known, this distance should always be the same.

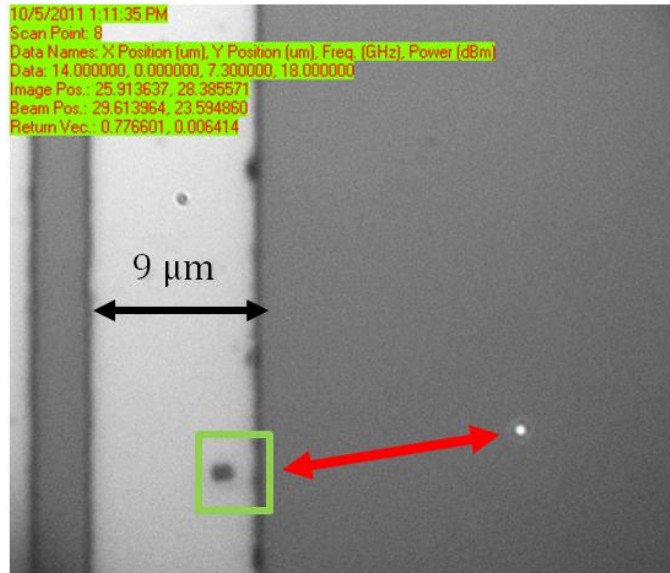


Figure 4.4.  $\mu\text{BLS}$  drift correction procedure.

The distance between the region of interest (outlined in green) and the beam spot must remain constant when the stage is in the alignment position.

Any difference from the known distance is due to drift and should be corrected. The camera pixels are calibrated to the stage position by moving the stage a known amount in the  $x$  and  $y$  directions and locating the region of interest selected using image recognition. Data of the drift correction shifts are shown in Figure 4.5, which shows that the routine is capable of maintaining the beam position with an accuracy better than 30 nm.

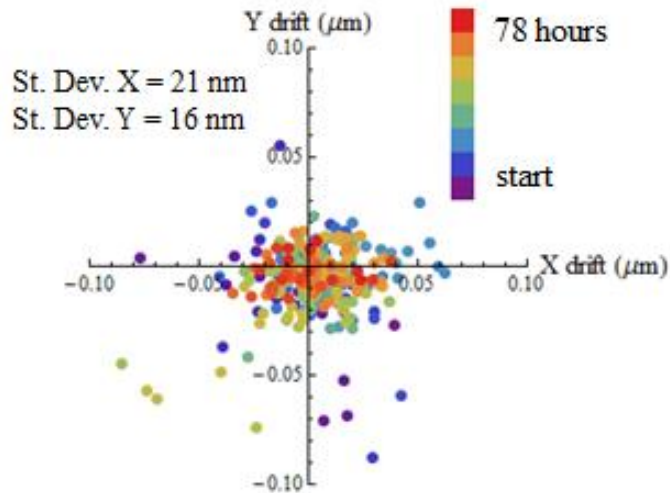


Figure 4.5. Data showing drift correction required over a three-day scan.

To obtain the beam position and spot size, the beam image on the CCD camera is fit with Gaussian functions in the  $x$  and  $y$  directions. The FWHM of the beam is typically about 320 nm when properly focused. One dimension is slightly larger than the other, due to the properties of linearly polarized light when focused. (See the optics section for more explanation.) If the sample surface is highly reflective, the beam will saturate the camera and it cannot be fit with a Gaussian function. If this is the case, the gain of the camera may be reduced programmatically when the beam coordinates and spot size are required. The peak intensity of the beam must be less than the saturation limit of the detector. Because the optical properties of the device studied may not be uniform, it is best to select a particular point where the beam position and spot size can be characterized well to perform the drift correction. The focus is maintained by either measuring the peak intensity of the beam spot or measuring the spot size by fitting with a

Gaussian. To correct for possible drifts in the focal position, the  $z$  axis of the positioning stage is scanned  $\pm 2 \mu\text{m}$  from the current position in steps of 200 nm and the position with the highest intensity or minimum beam size is the focused position.

The BrilliaNT program written by Dr. Demidov at U. Muenster controls the interferometer. It implements the active mirror stabilization routine and collects the counts recorded by the photocounting module. In our system, BrilliaNT runs on its own desktop computer because it consumes a lot of computational resources. If other programs are running on the same computer BrilliaNT sometimes hangs and must be restarted. There are certainly ways that the structure of the BrilliaNT program may be optimized to consume fewer resources should the need arise, but currently it is functioning just fine on its own computer. The BLS Scanner program interacts with BrilliaNT through a TCP/IP connection. Through this connection our program can start and stop BLS signal collection and request that BrilliaNT save data. It also monitors the positions of the mirror positioning stages. Occasionally one of the stages may go out of range over time. In that case, the BLS Scanner program will halt the data collection and request BrilliaNT to perform the autoalign procedure. This typically takes a few minutes to complete during which time the scan must be paused. The operator can be informed via email or text if the alignment procedure was required and whether it was successful. Physical intervention is required if the autoalignment is not successful, but fortunately this rarely happens.

## Sandercock Interferometer

The JRS TFP-1 interferometer is a tandem multipass interferometer with a special design that increases its contrast and free spectral range compared to a conventional Fabry-Perot interferometer. The essential part of a Fabry-Perot interferometer is the Fabry-Perot cavity which consists of two partially reflective mirrors with reflectivities of about 90-98%. The mirrors cannot be fully reflective because light must be able to enter and leave the cavity. Light is transmitted through the cavity when the optical path length between the mirrors is equal to an integer times the wavelength, i.e.,  $m\lambda = 2nd$  where  $n$  is the index of refraction of the material between the mirrors and  $d$  is the distance between the mirror surfaces. Therefore, the frequency transmitted is  $f = \lambda / nc$ . The transmitted frequency is scanned either by scanning the distance between the mirrors or scanning the index of refraction. The TFP-1 that we use scans the mirror separation with piezoelectric actuators. Alternatively, some interferometers change the index of refraction by adjusting the air pressure in the cavity between the mirrors [132], [133].

A basic Fabry-Perot cavity consists of two mirrors and the transmission lineshape is given by the Airy distribution

$$A(\sigma) = \left( \frac{T}{1-R} \right)^2 \frac{1}{1 + (4F^2 / \pi^2) \sin^2(2\pi nd / \lambda)} \quad (4.1)$$

Here  $T$  is the transmission of one of the mirrors,  $R$  is the reflectivity,  $\lambda$  is the wavelength of the laser in vacuum, and  $F$  is the finesse. The finesse is equal to the free spectral range divided by the full width half maximum of the lineshape. The free spectral

range is just the distance the mirrors must be scanned between transmission of one cavity mode and the next  $\Delta\lambda = \lambda^2 / 2d$ . Therefore, a higher finesse means a higher frequency resolution. In general, several factors contribute to the finesse and the individual factors add in parallel. The total finesse is then given by

$$\frac{1}{F^2} = \frac{1}{F_F^2} + \frac{1}{F_R^2} + \frac{1}{F_P^2} \quad (4.2)$$

where  $F_F$  is the flatness finesse,  $F_R$  is the reflectivity finesse, and  $F_P$  is the pinhole finesse. The flatness finesse is due to the flatness of the mirror and is given by

$$F_F = \frac{M}{2} \quad (4.3)$$

where  $1/M$  is the deviation expressed as a multiple of the wavelength from true flatness or parallelism across the mirrors. Obviously, if the mirror is not flat, the distance between the mirrors of the cavity is not well-defined, so the lineshape increases.

The reflectivity of the mirrors also contributes to the finesse. For reflectivities close to one, the higher the reflectivity, the higher the finesse. In practice, the reflectivity should not be too high because it decreases the transmission through the cavity.

$$F_R = \frac{\pi\sqrt{R}}{1-R} \quad (4.4)$$

The pinhole finesse is given by

$$F_P = \frac{4\lambda f^2}{D^2 d} \quad (4.5)$$

where  $f$  is the focal length of the lens and  $D$  is the diameter of the pinhole.

Generally the limiting values of the finesse are determined by the mirror reflectivity and the flatness. Limitations in the achievable flatness of the mirror and quality of substrate coatings limits  $F$  to about 100.

The contrast is the ratio of the maximum of the Airy function to the minimum and is equal to the following

$$C = 1 + \frac{4F^2}{\pi^2} \quad (4.6)$$

For a single pass interferometer, it is difficult to obtain a contrast better than  $C = 10^4$ . This contrast is sufficient as long as the ratio between the signal and the elastically scattered light is greater than  $10^{-4}$ . For scattering from opaque and reflective surfaces this is not the case and higher contrast is required. Fortunately, the contrast of the interferometer may be improved by passing the light several times through the same cavity. The contrast is then  $C^p$  where  $p$  is the number of passes. Contrasts as high as  $10^9$  have been obtained using a five-pass interferometer [134]. With the multipass arrangement the transmission (about 50%) and finesse (50-100) remain comparable to the single pass arrangement. A finesse of 100 implies that the FWHM is 250 MHz for a free spectral range that spans 50 GHz. Higher resolution may be obtained if needed by introducing a spherical Fabry-Perot cavity in tandem with the multipass interferometer [135]. Alternatively, one can employ a tunable laser to stabilize the interferometer (offset stabilization) and increase the resolution, as recently demonstrated in 2011 by Koreeda et al. [136].

The free spectral range can be increased without decreasing the resolution of the interferometer through the use of two interferometers in tandem with slightly different mirrors separation distances and thus different mode spacings. This is the principle behind the Sandercock interferometer, illustrated in Figure 4.6.

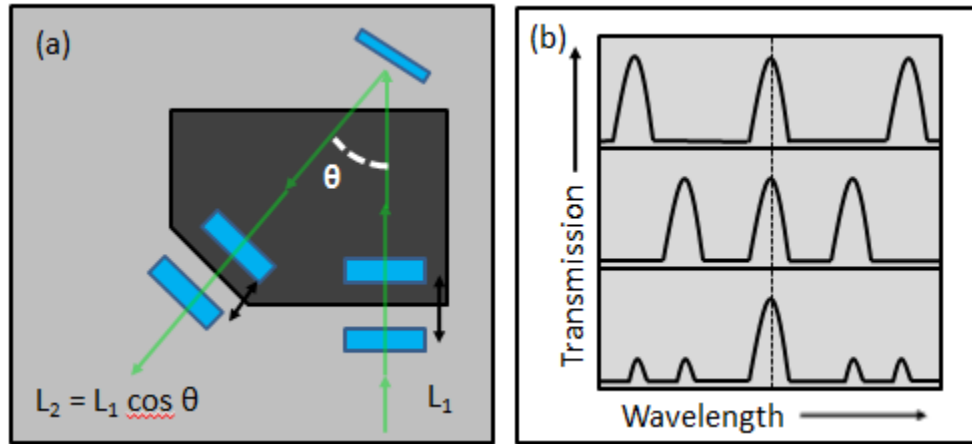


Figure 4.6. (a) Sketch of Sandercock interferometer. (b) Effect of tandem cavities on collected spectra.

An active alignment scheme is required to maintain the parallelization between the flat mirrors in each Fabry-Perot cavity and the distance between the mirrors. The alignment scheme is described in detail in [137]. In brief, alignment is accomplished by measuring the transmission of the reference beam, which is a sample of the laser that is not scattered from the sample. Each time the mirrors pass through the point at which the laser beam line is transmitted, the peak height of the transmitted beam is measured. One of the mirrors is then tilted slightly by the piezoelectric actuators along one of the axes and the peak height is measured again. If that peak height is greater than the one before, the tilt is maintained, otherwise, the mirror tilts back. Then the same action is performed for another axis. The Sandercock TFP-1 Interferometer requires 16 passes through the

reference beam to correct the alignment of all mirrors: two for each of the X-Y and four each for the spacing between the mirrors. Thanks to the alignment scheme, the transmission of the interferometer should be stable over extended period of times. However, the transmission cannot be assumed to be constant between passes, which is why the error in the photon counting bins is larger than the square root of the number of counts. This is important to consider when calculating error bars for collected spectra. A good strategy to judge the accuracy of the measurement is to break the total measurement into several identical pieces that can be averaged together and the standard deviation between the measurements divided by the square root of the number of measurements is the error in the calculated average.

## **Optics**

Perhaps the most essential optical component in the  $\mu$ -BLS setup is the Glan-Laser polarizer. It is used to isolate the rotated component of the scattered light from the sample. The polarizer consists of two crystals of calcite cut at a particular angle and sandwiched together. Because calcite is birefringent, light with orthogonal polarization components will be refracted at different angles. The crystal is cut in such a way that the S-Polarization (rotated) component is reflected through a  $68^\circ$  angle and exits the polarizer through one of the two side ports. The P-Polarization (nonrotated) passes straight through the polarizer. One should keep in mind that Glan-Laser polarizers are designed to work with well collimated light beams; divergent beams will result in multiple output beams.

The objective lens used to focus and collect the scattered light is the Mitutoyo M Plan Apo 100X LD, which has a numerical aperture of 0.70 and is highly corrected to

produce a flat image, with excellent color resolution. The objective is infinity-corrected, meaning that collimated light will be focused at the focal point of the lens to a diffraction limited spot size. The Apo in the name means it is an apochromatic lens. An apochromatic objective lens is corrected for aberrations with red, blue, and yellow light whereas a standard achromatic objective lens is only corrected for red and blue. The working distance is 6 mm, giving ample room for electrical connections to be made to the sample. The effective focal length is 2 mm, which is useful for calculating the magnification power. For example, using a 200 mm lens to focus the image from the microscope onto the CCD camera, the magnification is 100X.

The strong focusing of the objective means that a range of wavevectors is collected by the objective. This range of wavevectors is approximately given by the Fourier transform of the beam spot, which would have a maximum allowed wavevector approximately equal to  $2\pi/d$  where  $d$  is the diameter of the beam spot. Therefore, when a range of spin wave modes are active, such as with thermally excited spin waves, a broad peak is observed due to the spin wave dispersion. A thermal spectrum collected for 1 hour with a 2 mW beam from a 30-nm-thick permalloy film in a 1000 Oe field is shown in Figure 4.7 to illustrate this point.

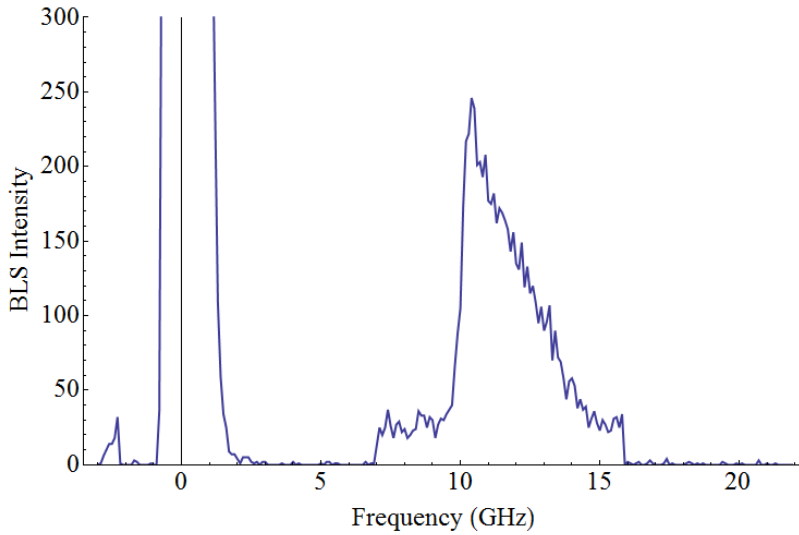


Figure 4.7. Thermal spin wave spectrum for a 30-nm-thick film in a 1000 Oe field.

### Laser

The laser used is a Spectra Physics Excelsior diode-pumped solid state laser. It outputs a continuous beam of 532 nm at 150 mW with a power stability of  $\pm 2\%$  as measured over an 8 hour period. The linewidth is less than 10 MHz, and the output polarization is vertical with the orthogonal component less than 1:100. The laser was chosen primarily because of its narrow linewidth, power stability, large longitudinal mode spacing, which are filtered to large degree. Diode pumped solid state lasers are becoming more popular to use in BLS measurements. Previously, the only lasers with sufficiently narrow linewidths were argon ion lasers which are difficult to use and maintain. Coherent Verdi lasers are another type of solid state laser that have also been used, but the longitudinal modes become visible in the collected spectra after long scans.

The gain crystal is neodymium-doped yttrium vanadate ( $\text{Nd:YVO}_4$ ). A diode laser pumps the  $\text{Nd}^{3+}$  ions to an excited state which relaxes by emitting a photon at 1064

nm. In the Excelsior laser, the infrared output of the neobdymuim-based laser is frequency doubled to produce green light at 532 nm using second harmonic generation in a potassium titanyl phosphate (KTP) crystal. The second harmonic power produced by second harmonic generation is

$$P_{2\omega} \propto \frac{d_{eff}^2 P_{\omega}^2 l^2 \Phi}{A} \quad (4.7)$$

where  $d_{eff}$  is the effective nonlinear coefficient,  $P_{\omega}$  is the pump laser power,  $l$  is the crystal length,  $\Phi$  is the phase-matching factor and  $A$  is the cross-sectional area of the beam in the crystal. Therefore, to obtain the highest conversion efficiencies, the nonlinear crystal is placed within the laser resonator.

The laser resonator consists of an optical cavity with two mirrors coated to reflect 532 nm light with the gain and nonlinear crystals in between. Because the gain envelope is relatively large at about 6-10 GHz, several longitudinal modes are allowed. To ensure single mode operation an etalon (a thin flat piece of glass in this case) is placed inside the microscope cavity.

The stability of the power incident on the sample is important to consider when measurements of beam intensity are made, and when intensities gathered over a long period of time must be compared. The power stability of the laser may be a significant factor especially when accuracies in the intensity above  $\pm 2\%$  are required in measurements lasting several hours. The beam pointing stability may also be a significant factor although this has not been carefully studied in our optical system. The alignment of the beam may change by up to  $6 \mu\text{rad}/^{\circ}\text{C}$ . Given that the light must travel over about 2 m

from the laser to the sample and another 1.5 m from the sample into the interferometer, this pointing stability may significantly affect the transmission of the optical system. It may be prudent to shorten the optical path length as much as possible or to monitor the power incident on the sample and the fraction of the scattered light transmitted through the interferometer.

## **4.2 SAMPLE FABRICATION**

### **Substrates**

We have used MgO, glass, sapphire and silicon substrates in fabricating our samples. The thermal conductivity, electrical conductivity, and optical properties are issues to consider when choosing the proper substrate for fabrication. Silicon substrates are the easiest to work with from a fabrication standpoint, but the reflective surface is not ideal for the optical position correction routine and the low thermal conductivity compared to sapphire means that less laser power can be applied for the measurement. When fabricating with electron beam lithography, silicon substrates only require a layer of resist. On insulating substrates, a layer of chromium must be deposited on top of the resist to dissipate the charge deposited by the electron beam.

### **Thin Film Deposition**

The ferromagnetic films used in were deposited with magnetron sputtering. It is the ideal method for depositing films of high purity with high quality interfaces. In a magnetron sputtering chamber a magnetic field is applied in the plane of the target surface to constrain the secondary electrons within a narrow region near the target surface. Trapping the electrons in this way drastically increases the chances that a sputtered atom from the target will become ionized. The increased ionization efficiency

of a magnetron results in a dense plasma in the vicinity of the target. This, in turn, leads to increased ion bombardment of the target, giving higher sputtering rates and, therefore, higher deposition rates at the substrate.

Other metals used for contact pads and antennas were deposited using thermal deposition. For thermal deposition metal is placed in a tungsten or molybdenum boat. The boat is connected across electrodes in the chamber. When the desired pressure is reached a current is run through the boat, which heats the boat and the material inside to the point that the material evaporates and is deposited on the substrate. Most metals will not stick well directly to a substrate so a few nanometer of chromium should be deposited first to ensure that the metal adheres well.

### **Focused Ion Beam Milling**

Focused ion beam milling (FIB) is a subtractive fabrication method whereby structures can be etched by bombarding the sample with heavy ions, typically  $\text{Ga}^+$ . The ions sputter away the unwanted material. The drawback to this method is that the edges of the structure can be contaminated with implanted Ga atoms that may affect the magnetic properties. Source ions are generally accelerated to an energy of 1–50 keV and focused onto the sample by electrostatic lenses.

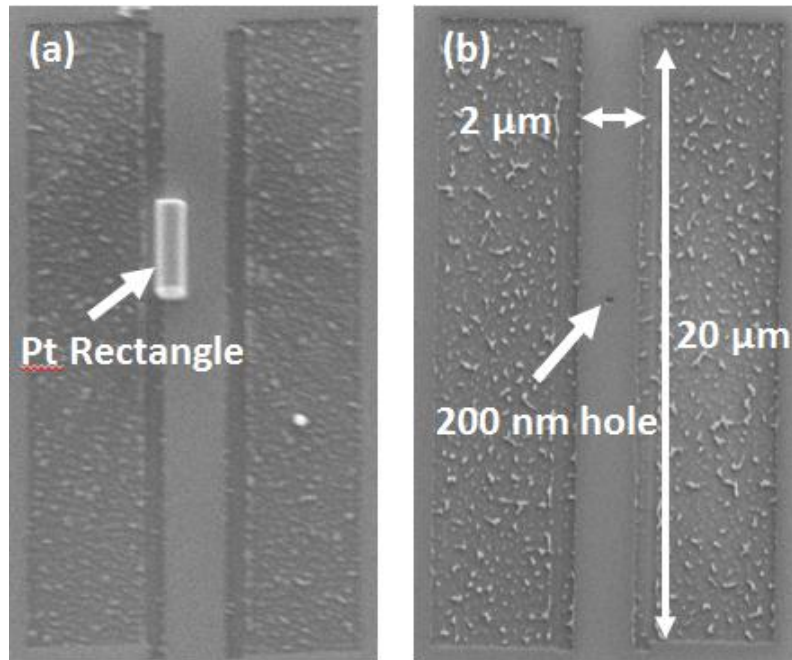


Figure 4.8. Scanning electron microscope images of Py waveguides. (a) A Pt strip laid across the waveguide did not have any visible effect on spin wave propagation. (b) A 200 nm hole scattered spin waves, as discussed in Section 5.2.

The FIB used at the CNM is an FEI Strata DB235 FIB. This system was used to fabricate the waveguide structures for the diffraction experiment discussed in Section 5.2 and the radiation experiment discussed in Section 5.3. Because the samples were fabricated on a sapphire substrate, charge buildup would cause the beam to drift during the etching of the large rectangles that defined the waveguide. The problem was solved by first etching lines to define the edges of the waveguide. The lines were small enough that charging of the surface did not present a problem. Then a large rectangular area was etched bordering the thin line defining the waveguide edge. During the writing, the rectangle was smeared by the drift of the beam, but because the edge was defined by the line that was etched previously, this no longer presented a problem. Scanning electron microscopy images of the fabricated waveguides are shown in Figure 4.8.

## **Photolithography**

Photolithography is a microfabrication technique used for transferring patterns from a mask to a device substrate using light. We use it to pattern devices with features greater than  $2\ \mu\text{m}$  magnetic waveguides and electrical contact pads. Although  $2\ \mu\text{m}$  is by no means the smallest feature size that can be achieved, it is the smallest size that can be achieved without considerable effort. Achieving higher resolution would require careful control and debugging of all stages of patterning, and the cost of masks with higher resolution increases considerably above this point. We have found it easier to use electron beam lithography for smaller features, as discussed in the next section. In the following discussion I will give an overview of the steps for patterning a substrate, pointing out relevant technical details and aspects. I will present the steps that we have actually used and discuss ways that improvements in resolution and repeatability can be made if needed. Several good books discuss photolithography in more detail, including the one by Chris Mack [138].

The technique is ideal for high throughput in making multiple copies of a pattern because the mask can be reused and the entire pattern is exposed at once. The mask consists of a transparent substrate with patterned dark regions. The mask substrate could be mylar, glass, or quartz in order of decreasing cost and achievable resolution. The dark regions of the mask are filled with black ink for mylar substrates and some type of metal, usually chrome, for the quartz and glass substrates. The light that passes through the transparent parts of the mask induces changes in a polymer film called photoresist, which can make the photoresist either amenable or resistant to removal by a developer solution in the case of positive and negative resist, respectively. Typically the mask is fabricated using another lithography technique that exposes the pattern point-by-point, such as electron beam lithography. Mylar masks can simply be made by printing, although not

with a conventional office printer because the dots are not dense enough to block light completely.

The photolithography process can be broken down into 9 steps: 1. substrate preparation, 2. photoresist coating, 3. baking, 4. exposure, 5. development, 6. post-development bake, 7. pattern transfer, and 9. resist removal. These steps can be repeated to make complex structures with several layers. The layers can be aligned under a microscope.

The device substrate must first be cleaned thoroughly to remove organic residue, adsorbed water and sometimes native oxide. For our purposes, we have found that in most cases blank substrates can be sufficiently cleaned by wiping the surface with a dust-free cloth and acetone and rinsing with isopropyl alcohol. This process should be repeated three to five times. Of course, if the substrate is not blank and contains fabricated structures, the substrate should only be rinsed, not wiped. If this procedure does not produce the desired results, a detergent called Hellmanex can also be used. The substrate is submerged in the solution and placed in an ultrasonic bath for at least an hour. Hellmanex will not remove metals on the substrate surface. More thorough cleaning can be accomplished with a piranha clean. Piranha solution is a mixture of sulfuric acid and hydrogen peroxide that removes organic residues and removes metals by forming complexes that dissolve in the solution. It also attaches  $-OH$  groups to the surface making it hydrophilic and potentially reducing the sticking ability of the photoresist. Note that metals will be removed in this process! The reaction between the sulfuric acid and hydrogen peroxide is exothermic and potentially explosive. Care must be taken to and this procedure can only be performed in specified fume hoods, and the one performing the reaction should wear extra protective equipment.

Photoresist is hydrophobic, so care must be taken to remove all water from the substrate surface. Baking the substrate on a hotplate or an oven will remove much of the water, but often a top layer of adsorbed water will remain, and  $-OH$  groups attached to the surface cannot be removed by heating. The remaining layer of water and  $-OH$  groups will make the surface hydrophilic and thus repulsive to the photoresist. Results can be improved using adhesion promoters which remove the water that is adsorbed on the substrate surface and replacing the  $-OH$  groups by organic groups that are soluble in the photoresist. Typically we do not use adhesion promoters for either electron beam lithography or photolithography because we have achieved adequate patterns without them, but for complex structures with small features they may prove useful. One of the most commonly used adhesion promoters is hexamethyl dizilane (HMDS). It should be beneficial no matter what substrate is used. HMDS can be applied to the substrate by spin coating then drying however, by far the preferred method of applying the adhesion promoter is exposing the substrate to HMDS vapor. This allows good coating of the substrate without excess HMDS deposition, and the high temperature of the vapor will result in a more complete reaction with the  $-OH$  groups. Once properly treated with HMDS the substrate can be left for up to several days without significant re-adsorption of water. A good test to determine whether is to apply a drop of water to the surface and determine the contact angle.

After organic residues and excess water are removed from the substrate surface, the substrate is ready to be coated with photoresist. This is typically done through spin coating, in which a sufficient amount of photoresist is applied to the center of the substrate then the substrate is spin at high speed. The centrifugal force will spread the photoresist evenly across the substrate. The speed and duration of the spinning determines the thickness of the photoresist. The calibration curves of speed vs. thickness

for the specific type of photoresist can be found in its datasheet. Ideally the walls of the resist are vertical and tall. The specific resist should be chosen according to the method in which the pattern will be transferred to the substrate. The resist can be of the positive or negative type, and some are more resistant to certain kinds of etching than others. It is possible to use positive resist can be used to make negative patterns, as will be discussed further in the next step. Small pieces like those we use are generally more difficult to work with than full wafers. The vacuum chucks cannot always be used so the piece must sometimes be secured to a silicon wafer with glue or wax. In addition, a thicker layer of resist collects around the edges of the sample, which makes it impossible to fabricate small structures near the edge. For this reason, the smallest features should not be located closer than 2 mm from the edge of the sample. Large contact pads can be fabricated closer to the edge without a problem, but the thicker parts may need to be exposed longer than the thin parts. The best results would be obtained by using a large wafer and cutting it into smaller pieces after processing.

The mask of the must have windows through which the alignment markers can be viewed. The resist is exposed under and ultraviolet mercury vapor lamp. The standard positive photoresist, which is not soluble in the aqueous base developer, is converted to a carboxylic acid on exposure to UV light in the range of 350–450 nm. If the pattern is over exposed, the features will be larger than expected and edges and corners will not be defined well.

After exposure, the sample is placed in a developer solution to remove the exposed resist. The pattern to be transferred to the sample remains. After development, the sample is baked to remove the excess developer solution before the pattern is placed in a chamber for either film deposition or etching.

## **Electron Beam Lithography**

Electron beam lithography (EBL) is similar in principle to photolithography, the important difference being that a focused beam of electrons are used to write the pattern rather than diffuse light shone through a mask. Electron beam widths of a few nanometers can be obtained, but the resolution is actually limited by secondary electron scattering from the resist or sample surface. The disadvantage of EBL is that the pattern is written point-by-point in serial, which is why the technique is not used for the large-scale fabrication of microchips. The process for sample preparation is mostly identical to that used for photolithography. The only step that differs significantly is the exposure step, which I will now describe. While EBL is perhaps the most accurate and precise of all the lithographic techniques, perfection comes at a high price. The complex equipment and slow exposure times makes EBL impractical as a mass production micro manufacturing method. Also, because electrons are charged particles, EBL must be performed in a vacuum.

Because EBL directs a beam of electrons at the substrate, charge may accumulate on insulating substrates causing the beam to drift and ruining the spatial resolution of the writing process. This makes insulating substrates more difficult to work with than silicon. The charge accumulation may be avoided by depositing a thin layer of metal on top of the photoresist. This gives the charge a path from the write area to the conducting pins holding the sample in place on the holder. In our case, we use about 3-5 nm of Cr for charge dissipation.

ZEP-520 and PMMA are popular photoresists. PMMA can be prepared in the lab by dissolving PMMA powder in Anisole solvent. The solution should then be filtered through filter paper to remove large pieces of PMMA that did not dissolve. If the liftoff procedure will be used, a bilayer of resist can be used to improve edge quality. A light

PMMA can be spread on the substrate and dried followed by a layer of heavy PMMA. The light PMMA at the bottom will be over exposed so that the edge profile will be undercut. This prevents the buildup of metal around the edges of the resist.

Before defining a pattern one must define the global coordinate system on the sample and align the individual write fields. A write field is the area over which the beam will raster. The write field is aligned to the global coordinate system using markers. In the RAITH or Zeiss SEM system, the alignment markers are identified by the user. In the JEOL system, the positions are identified in the macro and are found automatically by the machine.

## Chapter 5: Experiments

### 5.1 INTRODUCTION

In this section six different experiments are discussed that shed light on the unique properties of MSSW propagation and the possibility of affecting spin wave propagation with DC currents. The first four experiments resulted in papers that have been published. For completeness the majority of the discussions found in those papers are reproduced here with some added insights that did not fit into the papers or were developed after the papers were published. The last two experiments described

The spin wave diffraction and radiation experiments were completed in the laboratory of Prof. Sergej Demokritov at the University of Muenster using the micro-BLS system run by his staff scientist Dr. Vladislav Demidov. The samples were fabricated by myself with the help of Dr. Brian O’Gorman who was a student of Prof. Tsoi at the time. In the diffraction experiment, we explore how a spin wave excited inside a Permalloy waveguide scatters from a defect in the form of a hole drilled in the center of the waveguide. These results are relevant to the field of magnonics specifically to magnonic crystals in which periodic nonuniformities are used to create a customized spin wave band structure. In the radiation experiment, we explore how the anisotropic dispersion of MSSW causes spin waves to radiate in two beams, known as caustics, when they propagate from a ferromagnetic waveguide into a continuous film of the same material. The radiation pattern changes with frequency, and understanding the pattern is relevant to various spin wave logic and bandpass devices that have been proposed.

The spin wave decay and temperature experiments were completed using the micro-BLS system I constructed. First, we explore a property of the magnetic susceptibility that can cause the spin wave intensity to differ significantly from the expected exponential decay as it propagates away from the excitation source. The

magnetic susceptibility is shown to describe a propagating spin wave together with a slowly decaying background term that interfere to produce an oscillatory pattern in the spatial intensity profile of the magnetization away from the point of excitation. This feature is relevant to devices relying on spin wave propagation regardless of the excitation source because the background magnetization is built into the magnetic susceptibility. Second, we show that BLS can be used to measure the magnon temperature in a Permalloy film and that the temperature can be measured across a temperature gradient established in the plane of the film. Furthermore, we show that we can simultaneously measure the phonon temperature using the BLS signal scattered from phonons. This method permits the study of thermal transport in systems consisting of ferromagnetic films on a substrate. Such studies could provide insight into the processes involved in the spin Seebeck effect.

Finally, I will discuss two experiments that have not yet yielded publishable results. The first relates to our efforts to measure an increase in the spin wave propagation length due to the spin hall effect in a wave guide consisting of a bilayer of Ta and the ferromagnet CoBFe. We have not yet observed the increase in propagation length that we were hoping to find, but we have observed other effects which may be related that we cannot fully explain at this time. The final experiment relates to the spin Seebeck effect and currently in the planning stages. This experiment would build on our results for measuring the magnon temperature.

## 5.2 DIFFRACTION OF SPIN WAVES IN A WAVEGUIDE FROM A DEFECT <sup>1</sup>

Spin waves in thin ferromagnetic films have unique propagation characteristics, such as nonreciprocal propagation and an intrinsic anisotropy that make them interesting for use in spintronic devices. Many of these characteristics were discussed in Section 2.3. Numerous interesting propagation phenomena have been explored in waveguide structures that are relevant for device applications, such as cornering [124], self-focusing [139], edge-mode propagation [82], [140], second-harmonic generation [128] and tunneling-like behavior [141]. When a spin wave encounters an inhomogeneity it scatters and its wave vector is altered; some of the energy is transmitted and some is reflected. Alteration of the phase [142] and wave vector [143] as the spin wave propagates through an inhomogeneous magnetic field have been demonstrated. Thermal gradients can result in similar alterations to the propagating spin wave [144]. To a first approximation, the scattering is elastic so the frequency remains the same. In continuous films scattering into any wave vector with the same frequency is allowed. Due to the anisotropic nature of the spin wave dispersion relation this typically results in the formation of caustic beams [43], [86], [145]. In confined structures, the propagating modes are quantized spin waves and can only scatter into particular wave vectors. When the inhomogeneity is periodic, the resonant scattering conditions can lead to band gaps and the formation of so called magnonic crystals [80], [146–148], which could be applied in microwave signal processing devices. Therefore, a better understanding of spin wave scattering from inhomogeneities would be beneficial, which is the purpose of this experiment

In this experiment, we study the scattering of spin waves excited in a magnetic waveguide by a submicrometer circular defect. The defect scatters the incident fundamental mode of the waveguide into a combination of several higher order transverse

---

<sup>1</sup> This discussion follows closely that in Ref. [123].

modes resulting in a complex diffraction pattern. We show that the incident spin wave is partially reflected leading to an apparent standing wave pattern between the defect and excitation source and a significant drop in spin wave intensity after the defect. The efficiency of the reflection depends on the wave vector of the excited spin wave. Finally, we found that the defect does not significantly affect the propagation of the channeled double-beam spin wave.

The structure investigated consists of a Permalloy waveguide on a sapphire substrate with a gold microwave antenna laid over the top. A sketch of the sample is shown in Fig. 5.1. The sample was prepared as follows: a 36-nm-thick film of Permalloy was first sputtered on a sapphire substrate. Then, a waveguide, 20- $\mu\text{m}$ -long, and 2- $\mu\text{m}$ -wide, containing a circular defect with the diameter of 200 nm in its center was etched into the continuous film using a focused ion beam. After etching, a 5-nm-thick layer of  $\text{SiO}_x$  was deposited uniformly over the entire sample to insulate the waveguide from the excitation circuit and protect the Permalloy film from corrosion. A 50-nm-thick, 2.4- $\mu\text{m}$ -wide stripe antenna was defined using photolithography, followed by thermal deposition of gold and a lift off procedure. The antenna was positioned over the waveguide 2.8  $\mu\text{m}$  away from the defect.

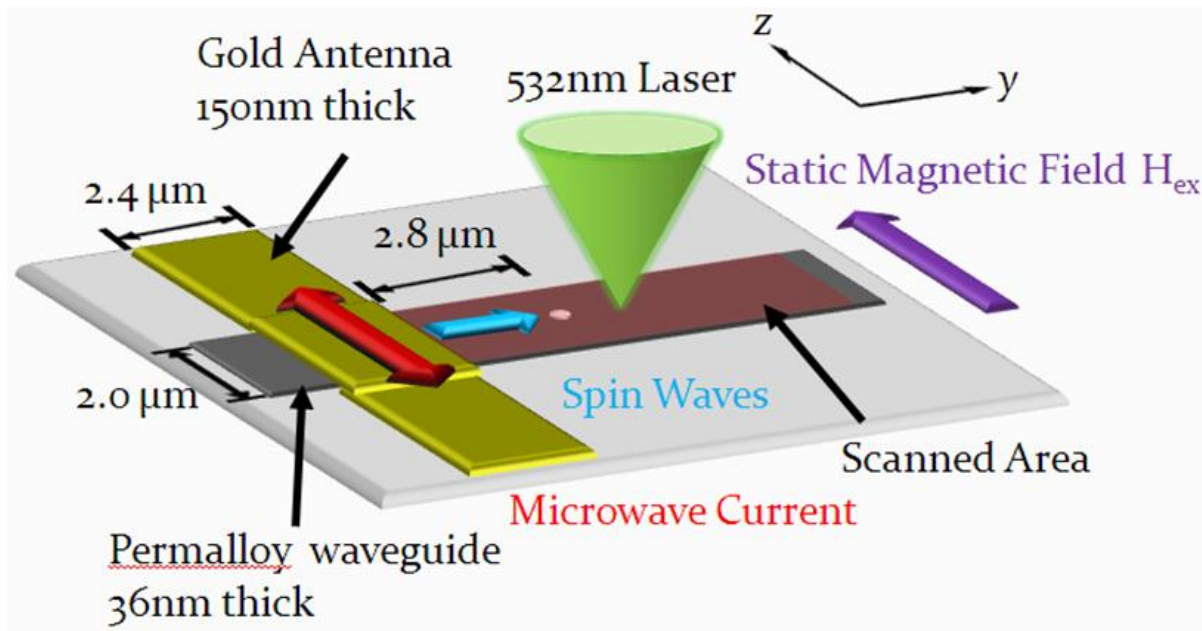


Figure 5.1. Drawing of Permalloy waveguide with hole to scatter spin waves. The green cone shows the probing laser beam, which is scanned over the red shaded area to map the spin wave intensity.

Spin waves were excited under the antenna by passing a microwave current through it. A uniform magnetic field of 900 Oe was applied perpendicular to the waveguide axis to enable the excitation of MSSWs. Although the applied field is uniform, the field inside the waveguide is reduced at the center due to demagnetization effects and goes to zero at the edges.<sup>4</sup> Assuming pinned spins at the edges, the allowed modes along the transverse ( $z$ ) direction of the waveguide are standing modes with wave numbers  $k_z = n\pi/w$ , where  $w$  is the width of the waveguide and  $n$  denotes a nonzero natural number. Figure 5.2 shows the calculated dispersion curves of the three lowest odd-order transverse spin wave modes of the waveguide. The calculation, following Ref. [139], takes into account the reduced internal field at the center of the waveguide. The

efficiency of excitation of odd-order modes quickly reduces with the order number  $n$ , whereas even-order modes cannot be excited in the studied system due to the symmetry of the dynamic field of the antenna over the width of the waveguide. The frequency band over which the fundamental mode ( $k_z = \pi / w$ ) can be excited is limited by the fact that the maximum wave number that can be excited by the antenna with significant amplitude is  $k_y < \pi / d$  where  $d$  is the width of the antenna [108]. Therefore, the fundamental mode can only be efficiently excited by the antenna for frequencies between 8.4 and approximately 9.2 GHz (see Fig. 5.2).

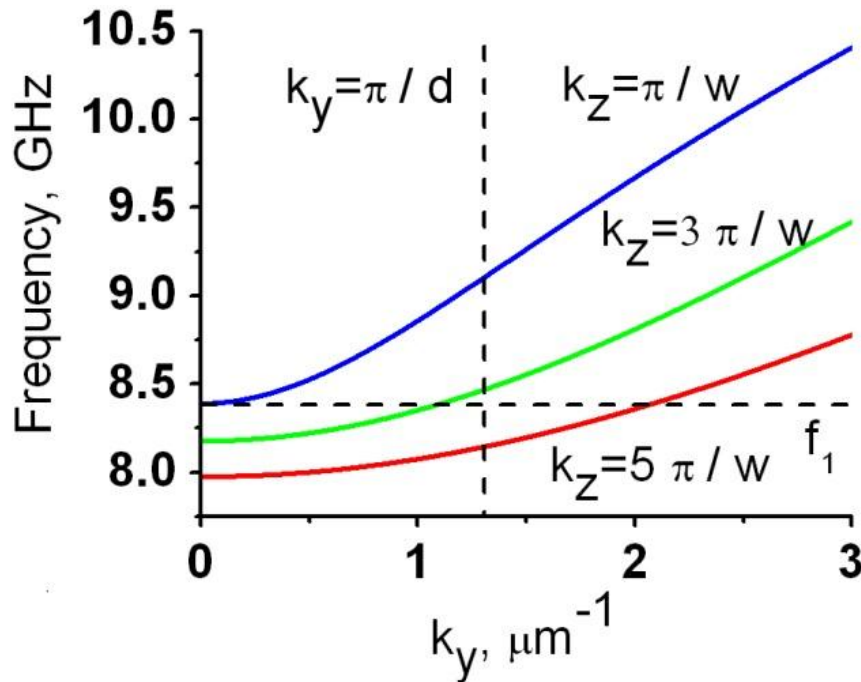


Figure 5.2. Dispersion curves for three odd-ordered transverse waveguide modes. The dashed vertical line indicates the highest wave vector that can be excited by the antenna. The dashed horizontal line indicates the lower cutoff frequency of the fundamental waveguide mode, which is the lowest frequency that can be efficiently excited. Figure reproduced from Ref. [123].

We first mapped the spin wave intensity inside the red shaded area in Figure 5.1 with an excitation frequency of 8.9 GHz. This map is shown in Fig. 5.3(a). All spin wave intensity data presented in this paper are multiplied by  $\exp(\gamma y)$  to numerically compensate the spatial decay of spin waves, where  $y$  is the propagation coordinate and experimentally determined decay rate ( $\gamma = 0.7 \mu\text{m}^{-1}$  at 8.9 GHz). The spin wave intensity pattern exhibits a half sine profile in the  $z$  direction between the antenna and the defect as expected for the fundamental mode. After encountering the defect, however, the spin wave intensity pattern drastically increases in complexity.

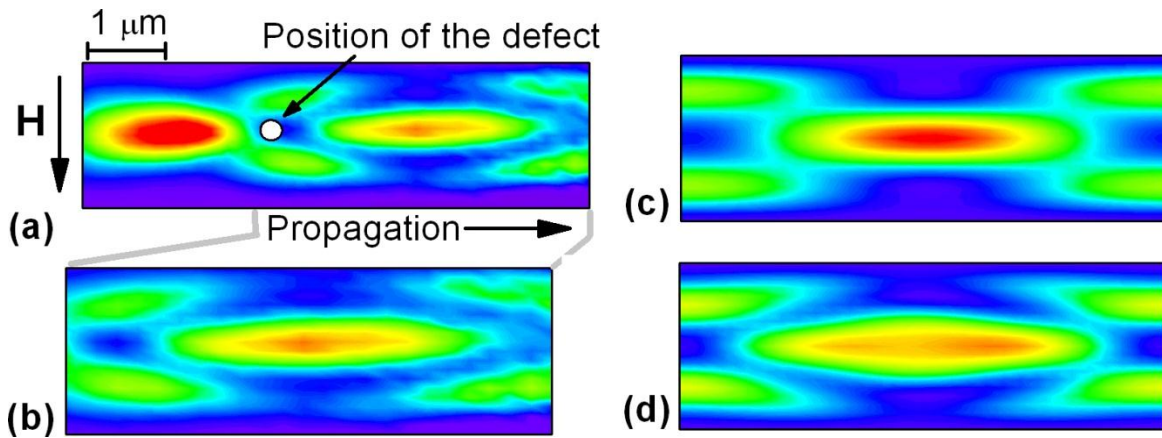


Figure 5.3. Measured and calculated spin wave diffraction pattern.

(a) Spin wave intensity map recorded for the excitation frequency of 8.9 GHz. Data was collected with step sizes of 0.1 and 0.2  $\mu\text{m}$  along the  $z$  and  $y$  directions respectively. The map has dimensions of 2 by 7  $\mu\text{m}$ . (b) Portion of the measured diffraction pattern after the defect. (c) Calculated intensity obtained by taking into account the modes with the order numbers  $n=1$  and 3 only. (d) Calculated pattern for three modes with  $n=1, 3$  and 5. Figure reproduced from Ref. [123].

The transformation actually starts slightly before the incident wave reaches the position of the defect, which suggests that the spin wave diffracts from the inhomogeneity of the internal magnetic field caused by the defect, rather than from the defect itself. The

complex diffraction pattern seen after the defect can be considered as interference produced by several co-propagating modes of the waveguide. The interaction of spin waves with a defect results in the energy transfer from the fundamental mode excited by the antenna into higher-order modes, which the antenna cannot excite directly. We attempted to reproduce the experimentally observed pattern by calculating a superposition of modes, where the amplitude and phase differences of the modes are the fitting parameters. The measured intensity map after the defect is displayed in Fig. 5.3(b) for easy comparison with the calculated interference patterns in Figs. 5.3(c) and 5.3(d). The calculation in Fig. 5.3(c) includes only the first two modes,  $n = 1, 3$ , and it already exhibits a characteristic structure of alternating lobes with the maxima of the spin wave intensity at the edges of the waveguide and on its middle line. When the third mode ( $n = 5$ ) is added (Fig. 5.3(d)), the edge lobes tilt with respect to the axis of the waveguide, and the center maximum assumes a diamond-like shape. These features are consistent with experimental observations. We found that the experimental pattern is best reproduced for the relative amplitudes of the modes equal to 1, 0.6, and 0.2 for  $n = 1, 3, 5$ , respectively. These results indicate that the excitation of higher-order waveguide modes due to the diffraction on a small-size defect is much more efficient than that achieved with a stripe antenna in an unobstructed waveguide [139]. We conducted similar experiments for several frequencies within the fundamental mode frequency range of 8.4–9.4 GHz. All of them show qualitatively similar diffraction patterns to that in Fig. 5.3(a), but significantly different efficiencies of spin wave reflection. The latter fact is demonstrated in Fig. 5.4, which shows the spin wave intensity

integrated across the width of the waveguide as a function of the propagation coordinate for three different frequencies. The data are normalized at the positions of the maxima. After compensating for the spatial decay as described above, the spin wave intensity past the defect is nearly constant. The integrated intensities of Fig. 5.4 reveal two significant features. First, a standing wave in the  $y$  direction is formed by the partial reflection of the spin wave from the defect. Second, the relative intensity of the diffracted waves depends on the frequency of the incident spin wave in a nonmonotonous way. This intensity increases from 8.5 to 8.9 GHz. Above 8.9 GHz (data not shown), the intensity decreases until reaching a minimum at 9.1 GHz, after which it increases again. This oscillatory behavior could be due to a resonant interaction of spin waves with an inhomogeneous static magnetic field.<sup>16</sup> In order to understand this dependence in detail, one needs to take into account the long-range dipolar fields of the spin waves and the exact spatial distribution of the internal magnetic field inside of the Permalloy waveguide, which is strongly nonuniform due to the presence of the defect.

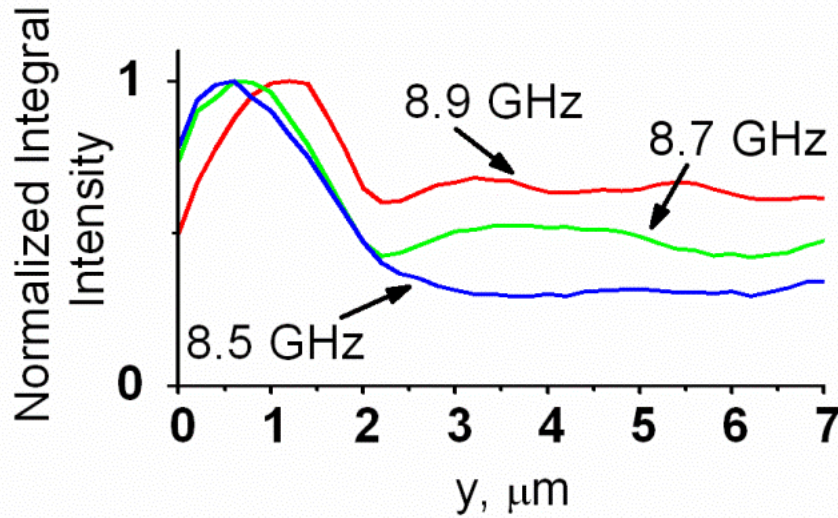


Figure 5.4. Reflection of spin wave from defect.

The spin wave intensity integrated across the width are plotted to show the reflection and transmission of power due to the defect at three different frequencies. The data are normalized at the position of maximal intensity. Figure reproduced from Ref. [123].

Finally, we analyzed the influence of the defect on spinwaves propagating in field-induced channels formed close to the edges of the Permalloy waveguide due to the nonuniformity of the internal magnetic field [83]. To observe double channel propagation, we recorded spin wave intensity maps at microwave excitation frequencies below the lower cutoff frequency of the fundamental mode  $f_1$  (see Fig. 5.2). A typical map obtained at 8.1 GHz is shown in Fig. 5.5(a). As expected, the map displays two spin wave channels shifted toward the edges of the Permalloy waveguide. In contrast to the case of the fundamental mode, the channeled spin waves do not encounter the magnetic inhomogeneity caused by the defect; therefore, their propagation is not affected significantly. The only noticeable effect is a small variation of the distance between the

spin wave beams as a function of the propagation coordinate, which is depicted quantitatively in Fig. 5.5(b). The observed variation can be understood as slight deformation of the field-induced channels due to the nonuniformity of the internal magnetic field caused by the defect. As the excitation frequency was increased toward  $f_1$ , the beams shifted closer to the middle of the stripe and the variation of the distance between them became more pronounced but the presence of the defect did not lead to any noticeable spin wave diffraction or reflection effects.

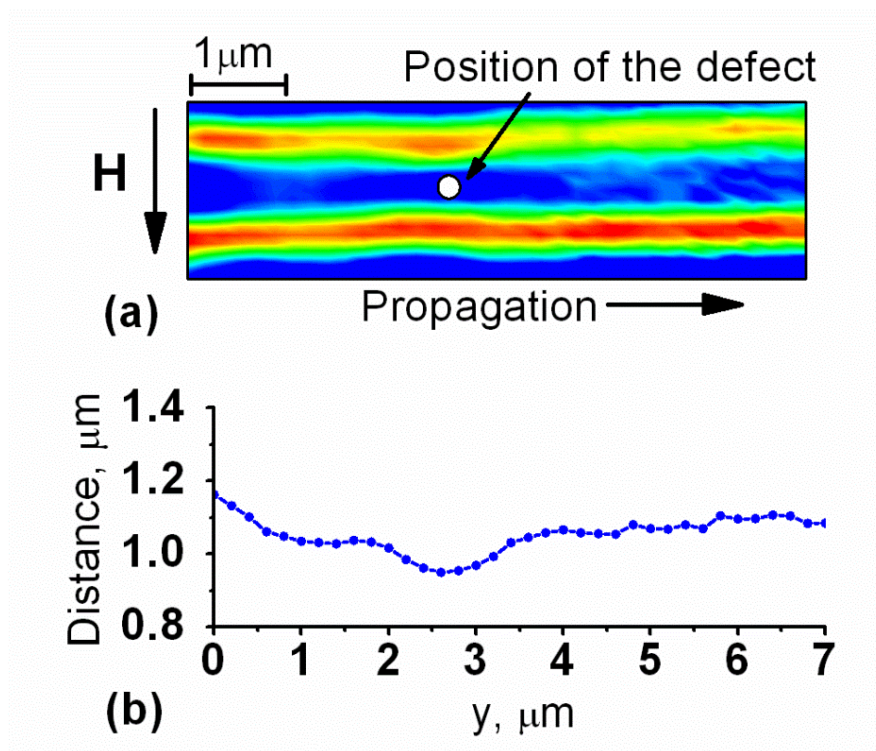


Figure 5.5. Edge mode propagation around defect. (a) Spin wave intensity map recorded for the excitation frequency of 8.1 GHz. (b) Separation distance between the two channels as a function of the propagation coordinate. Figure reproduced from Ref. [123].

In conclusion, we have experimentally studied the influence of a submicrometer-size defect on spin wave propagation along a 2- $\mu\text{m}$ -wide Permalloy waveguide. We show that such small defects cause strong diffraction and reflection of spin waves corresponding to regular waveguide modes, but they have little influence on the propagation of channeled spin waves. These findings complement recent studies regarding the manipulation of spin wave propagation in micro-waveguides and provide important background for technical applications of spin waves in guiding structures for signal processing.

### 5.3 RADIATION OF SPIN WAVES FROM A WAVEGUIDE INTO A CONTINUOUS FILM<sup>1</sup>

Here we report on the experimental investigations of spin wave radiation from a 2- $\mu\text{m}$ -wide magnetic-stripe waveguide into a continuous magnetic film. The measurements were performed using spatially resolved microfocus Brillouin light scattering ( $\mu\text{-BLS}$ ) spectroscopy, which allowed the direct two-dimensional visualization of spin wave propagation with the submicrometer spatial resolution. We show that the radiation of spin waves is strongly affected by the spatial variations of the demagnetizing field. These variations lead to a total reflection of spin waves if their frequency lies within a certain interval. At frequencies where the radiation is allowed, one observes rather unusual propagation features originating from the anisotropy of the spin-wave dispersion. The spin-wave patterns exhibit a multiple-ray structure with a clearly defined preferential radiation direction depending on the excitation frequency and the static magnetic field. We also provide an analytical model explaining these experimental findings.

Figure 5.6 shows the sketch of samples used in the experiments. A 36-nm-thick permalloy (Py) film deposited onto a sapphire substrate by a magnetron sputtering was patterned using a focused ion beam to define a 2- $\mu\text{m}$ -wide and 20- $\mu\text{m}$ -long stripe waveguides, as shown in the figure. After the patterning process, the structure was covered by a 5-nm-thick  $\text{SiO}_x$  layer to provide protection from oxidation and electrical isolation of the Py structure from the excitation circuit. Finally, a 150-nm-thick gold (Au) stripe antenna was defined using photolithography followed by thermal deposi- tion of

---

<sup>1</sup> This discussion follows closely than in Ref. [145].

the gold and a lift-off process. The antenna had a width of  $t=2.4\ \mu\text{m}$  and was positioned at a distance of  $3.2\ \mu\text{m}$  from the junction between the stripe waveguide and the unpatterned film. The sample was placed into a uniform static magnetic field of 900 Oe applied in the plane of the Py waveguide and perpendicular to its axis. In this way, the

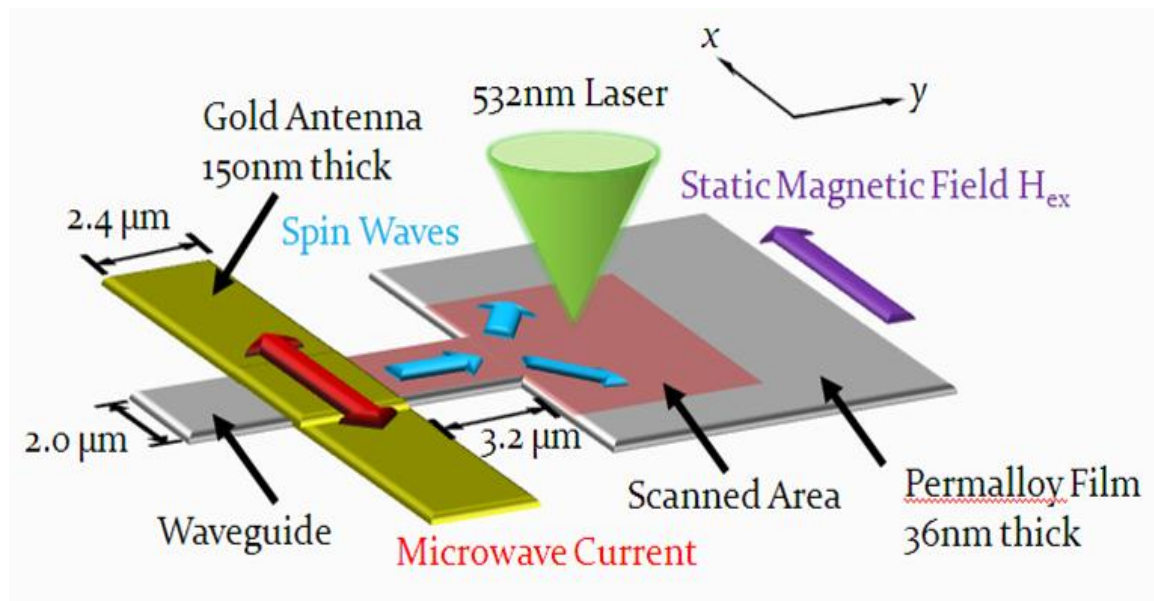


Figure 5.6. Drawing of permalloy waveguide emptying into a continuous film. The green cone shows the probing laser beam, which is scanned over the red shaded area to map the spin wave intensity.

propagation geometry of the so-called Damon-Eshbach (DE) spin waves [103] was realized for the waveguide. The excitation of spin waves was performed by a transmission through the stripe antenna of a continuous-wave microwave current at a fixed frequency  $F$ . The current created a dynamic magnetic field  $h$  coupled to the dynamic magnetization in the permalloy waveguide mainly via its in-plane component

$h_y$ , providing a well-localized excitation of spin waves underneath the antenna. Due to the finite width of the antenna, spin waves with wave numbers up to the order of magnitude of  $\pi/t = 1 \mu\text{m}^{-1}$  can be effectively excited in the waveguide. The detection of spin waves was performed by the BLS technique described in detail elsewhere [54]. Using this technique we mapped two-dimensional spatial distributions of the spin-wave intensity with submicrometer resolution. In particular, two spatial regions were analyzed: the part of the waveguide between the antenna and the continuous film (scanned area 1 in Fig. 5.6) and the part of the continuous film adjacent to the junction with the waveguide (scanned area shaded in red in Fig. 5.6).

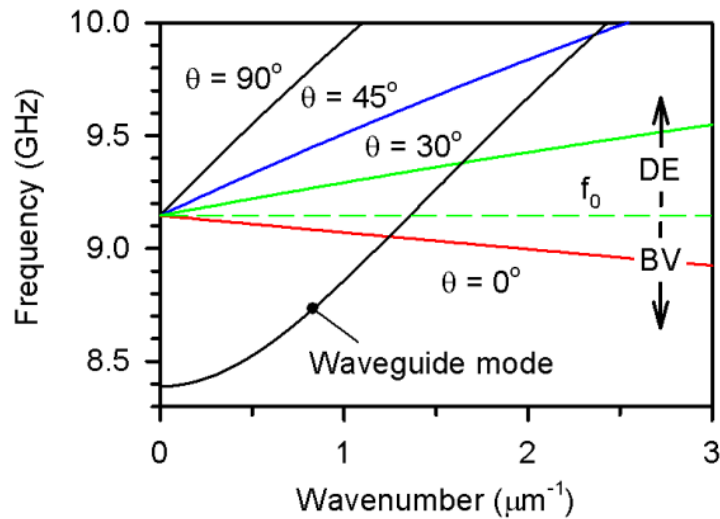


Figure 5.7. Dispersion of spin waves in the waveguide and continuous film. The waveguide mode is marked and the lines marked with the angle  $\theta$  indicate the dispersion for spin waves propagating at an angle  $\theta$  with respect to the applied magnetic field. The FMR frequency is denoted as  $f_0$ . Figure reproduced from Ref. [145].

Before analyzing experimental results, we briefly review the theoretical background of spin wave propagation in the system under investigation. Figure 5.7 shows the spin-wave dispersion characteristics for the stripe waveguide and the continuous magnetic film calculated for our experimental conditions using the theory developed in Ref. [108]. The curve marked in Fig. 5.7 as “waveguide mode” is the dispersion curve for the fundamental mode in the 2- $\mu\text{m}$ -wide wave guide calculated according to Ref. [139]. This mode has the simplest half-sine distribution of the spin wave amplitude over the waveguide width and is characterized by the transverse wave number  $k_z = \pi / w$ , where  $w$  is the width of the waveguide. Higher order modes [139] with  $k_z = n\pi / w$  and  $n > 1$  are not considered here, because, as follows from the experimental data, they are excited by the used antenna very inefficiently. The lines labeled with  $\theta = 0, 35, 45, 90^\circ$  are the spin wave dispersion curves calculated for the continuous permalloy film calculated for different angles  $\theta$  between the direction of the static magnetic field and the wave vector of the spin waves ( $\theta = \arctan(k_y / k_z)$ ). In contrast to spin waves in the waveguide, for which only discrete values of  $k_z$  are allowed ( $k_z = n\pi / w$ ), every combination of  $k_y$  and  $k_z$  is allowed for spin waves in the film. The horizontal dashed line in Fig. 5.7 marks the frequency of the uniform ferromagnetic resonance  $f_0$  in the film, which separates the frequency regions of the DE and backward volume (BV) spin waves.

As seen from Fig. 5.7, the spectrum of spin waves in the waveguide is shifted with respect to that in the continuous film toward smaller frequencies. This happens due to the reduction in the internal magnetic field caused by the demagnetizing effects in the

waveguide [82]. Note that spin waves of the fundamental waveguide mode have a lower cutoff frequency at  $k_y = 0$ . It is equal to about 8.4 GHz for our experimental conditions. The lower cutoff frequency of the spin wave spectrum in the film is 8.3 GHz corresponding to  $k_y \approx 25.6 \mu\text{m}^{-1}$  (out of the range of Fig. 5.7). Such a mismatch between the spectra results in a significant conversion of the wave vector of spin waves radiated from the waveguide into the film. However, the interval of wave numbers where this conversion is possible is much smaller than  $25.6 \mu\text{m}^{-1}$ . In fact, it is determined by the waveguide width, which defines the scale where the translational symmetry of the unconfined film is broken. Thus, the radiation of spin waves with  $k_y \gg \pi/w = 1.5 \mu\text{m}^{-1}$ , i.e., with the frequency much below 9 GHz, happens very inefficiently. Correspondingly, the mismatch between two spectra results in the appearance of a frequency range between the lower cutoff frequency of the waveguide mode at 8.4 GHz and about 9 GHz where spin wave propagation is allowed for the confined waveguide, but their radiation into the continuous film is very unlikely. For larger frequencies, the above discussed conversion is allowed. However, it is accompanied by a noticeable change in the wave vector of spin waves. Therefore, one can expect nontrivial frequency-dependent radiation characteristics.

In the first step of the experiments, we analyzed the propagation of spin waves within the frequency range where the radiation is prohibited. For this, we measured two-dimensional maps of the spin wave intensity  $3 \mu\text{m}$  inside the waveguide and  $2 \mu\text{m}$  outside over the width of the waveguide for  $F$  gradually increasing from 8.4 GHz. A typical

spin-wave intensity map obtained in these measurements is shown in Fig. 5.8(a). The map has dimensions of  $2 \times 5 \mu\text{m}^{-1}$  and was recorded with spatial step sizes of 0.1 and 0.2  $\mu\text{m}$  in the  $z$  and  $y$  directions, respectively. The vertical dashed line in Fig. 5.8(a) shows the position of the junction between the waveguide and the continuous film. Figure 5.8(a) proves the absence of the spin wave radiation within the discussed frequency range. On the right side from the position of the junction the spin waves exhibit very fast decay of their intensity. On the left side they show a nonmonotonous dependence of the intensity on the propagation coordinate  $y$  with a clear maximum and a minimum caused by a formation of a standing wave. Figure 5.8(b) further characterizes the spin wave behavior at different frequencies. It shows dependencies of the spin-wave intensity integrated over transverse cross sections of the waveguide on the propagation coordinate for three different excitation frequencies. The integrated intensity is normalized at the position of the junction. As seen from Fig. 5.8(b), the decay of the spin wave intensity in the continuous film is nearly exponential (note the logarithmic scale) and slightly weakens with the increase in the frequency.

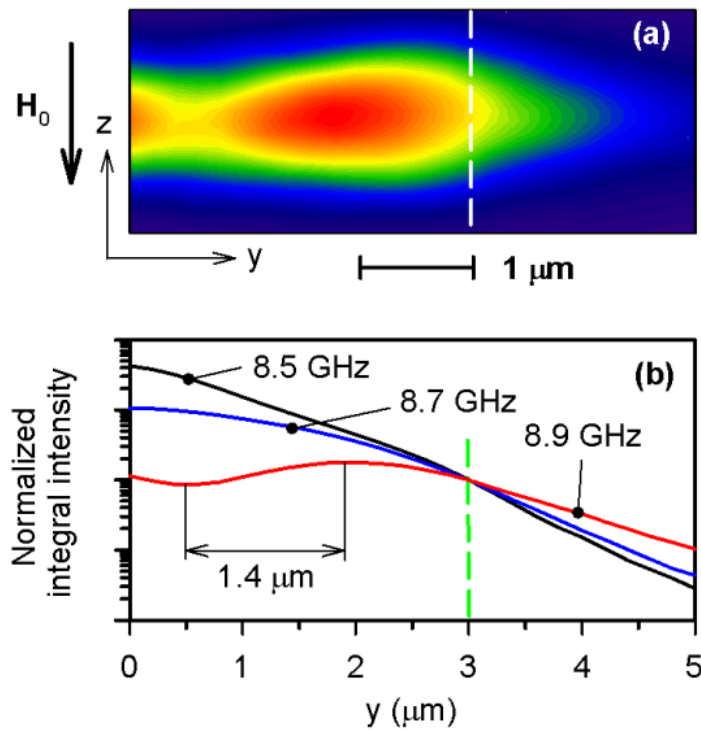


Figure 5.8. Behavior of spin waves at frequencies too low to propagate in the film. (a) Spin wave intensity map over a range  $3 \mu\text{m}$  inside the waveguide and  $2 \mu\text{m}$  outside. The scan range in the  $z$  direction is over the width of the waveguide. The vertical dashed line shows the position of the end of the waveguide. (b) Spin wave intensity integrates over transverse cross sections of the stripe waveguide as a function of the propagation coordinate for three different excitation frequencies as indicated. The data are normalized at the end of the waveguide. Note the logarithmic scale of the vertical axis. Figure reproduced from Ref. [145].

Within the waveguide, the intensity profile shows a behavior typical for the formation of a standing wave. At the frequency of  $8.9 \text{ GHz}$ , one can clearly see its node at  $y = 0.5 \mu\text{m}^{-1}$ . By measuring the distance from this node to the nearest maximum, one can estimate the wavelength of spin waves  $\lambda$ . As seen from Fig. 5.8(b),  $\lambda/4 = 1.4 \mu\text{m}^{-1}$

agrees well with the theoretical value of  $1.47 \mu\text{m}$  calculated based on the spin wave spectrum shown in Fig. 5.7. Note that since the wavelength of the standing wave should increase with decreasing frequency, the corresponding minima are not seen for lower frequencies.

Considering the discussion of the data in Fig. 5.8, one concludes that the shift of the spin wave spectrum due to the variation in the demagnetizing field leads to total spin wave reflection from the junction between the waveguide and the continuous film with the formation of a standing spin wave inside of the waveguide. The reflection is accompanied by a tunneling-like [149] penetration of the spin wave into the continuous film. The penetration length appears to increase with increasing frequency (decreasing wavelength) of the incident spin wave. This does not allow one to directly relate the penetration length to the spin wave wavelength, as one expects for a nonresonant excitation by a dipole field. Most probably the found dependence is caused by the frequency dependent dynamic susceptibility of the permalloy film, which increases as the frequency approaches the frequency of the uniform resonance  $f_0$ .

As discussed above, increasing the frequency  $F$  one should finally come to the situation when the radiation of spin waves into the continuous film becomes allowed. Experimentally we detected the appearance of the radiation for  $F > 9 \text{ GHz}$ , which agrees with the estimations presented in the previous section. Since the observed radiation has rather complex character we need to discuss the peculiarities of spin wave dispersion in a continuous ferromagnetic film first. Figure 5.9 shows another representation of the spin-wave spectrum shown in Fig. 5.7. The lines in Fig. 5.9 are the constant frequency

contours projected onto the  $k_y - k_z$  plane. In this representation, the vector of the phase velocity  $\mathbf{V}_{ph}$  is parallel to the wave vector  $\mathbf{k} = (k_y, k_z)$ , whereas the vector of the group velocity

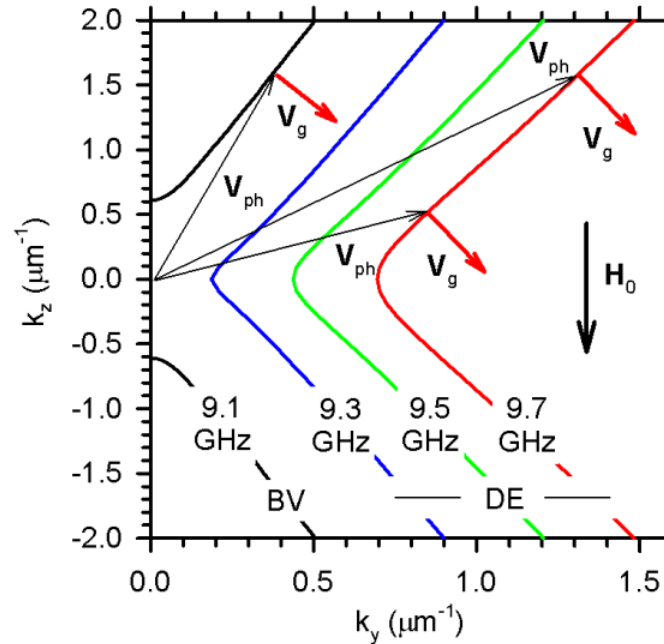


Figure 5.9. Constant frequency curves of spin waves showing the group velocity. Arrows show the directions of the phase  $\mathbf{V}_{ph}$  and group  $\mathbf{V}_g$  velocities. The applied magnetic field is indicated by  $\mathbf{H}_0$ . Figure reproduced from Ref. [145].

$\mathbf{V}_g$  is directed along the normal to the constant-frequency contour ( $\mathbf{V}_g = 2\pi \nabla F(k_y, k_z)$ ) shows that the dispersion characteristics of spin waves have very specific anisotropy: while the direction of the phase velocity for a given frequency can change in a wide range of angles (as usual for sound and light waves), the group velocity exhibits a certain preferential direction only slightly dependent on  $F$  and the type of spin waves (DE or BV). The transformation of spin waves at the interface between the waveguide and the

continuous film can be considered as a reradiation that conserves the frequency, but not the wave vector. In this case, the spin waves radiated into the continuous film should have all combinations of  $k_y$  and  $k_z$  possible for the given  $F$ , limited by the inefficiency of the wave vector conversion only. Nevertheless, despite this large diversity in the direction of the phase velocity, the radiated waves should show a preferential direction of the energy flow defined by the direction of the group velocity [86]. This fact is further illustrated by Fig. 5, which shows dependencies of the angle of the group velocity with respect to the  $z$  axis at a value close to  $70^\circ$  and then stays nearly constant.

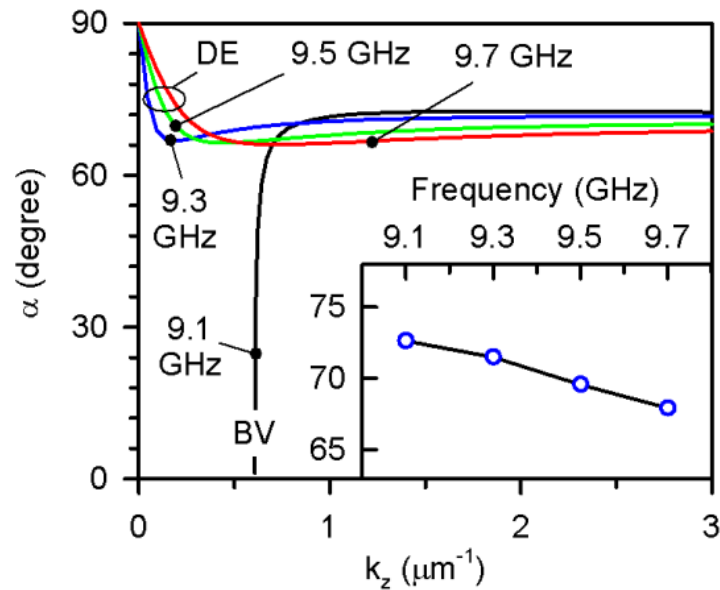


Figure 5.10. Angular dependence of the spin wave group velocity. The angle  $\alpha$  is taken between the group velocity and the  $z$  direction for different frequencies. The inset shows the frequency variation of the mean angle  $\alpha$  for the interval  $k_z = 1-3 \mu\text{m}^{-1}$ . Figure reproduced from Ref. [145].

As a result, this direction is expected to dominate over others in the radiation process. The inset in Fig. 5.10 shows the frequency variation of the mean angle  $\alpha$  for the interval  $k_z = 1-3 \mu\text{m}^{-1}$ , where the dependencies of Fig. 5.10 are saturated. These data can be directly used for comparison with the experimental results.

Figure 5.11 presents the experimentally obtained maps of spin wave radiation at frequencies higher than the radiation threshold 9.0 GHz. The maps have dimensions of

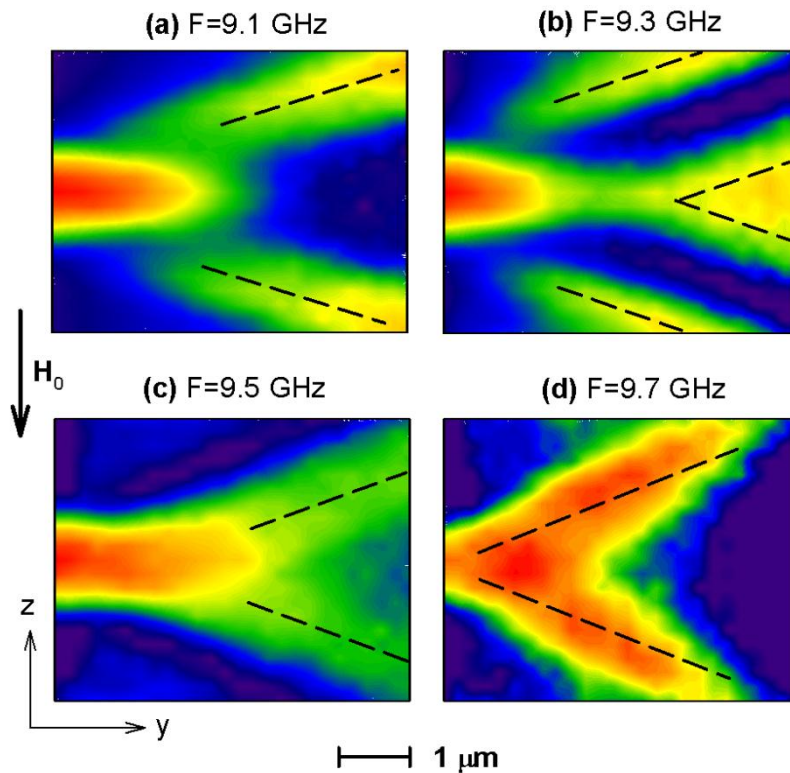


Figure 5.11. Maps of spin wave radiation at different frequencies. The right edge of the maps begin at the edge of the waveguide, which is centered vertically. The scan area measures  $4 \times 5 \mu\text{m}^2$ . The spatial decay of the spin waves is numerically compensated. The dashed lines show the theoretically obtained directions of preferential radiation. Figure reproduced from Ref. [145].

$4 \times 5 \mu\text{m}^2$  in the  $z$  and  $y$  directions, respectively. They were recorded with a spatial step size of  $0.2 \mu\text{m}$  in both dimensions. To elucidate the intrinsic structure of the radiation patterns, the spatial decay of spin waves is numerically compensated by normalizing the integral of the spin wave intensity over the  $z$  cross sections of the maps [82]. Figure 5.11 clearly shows that, in accordance with the above theoretical discussion, the radiation of spin waves into the continuous film happens along certain clearly defined directions only, resulting in a formation of spin wave rays oriented at a certain angle with respect to the direction of the static magnetic field  $\mathbf{H}_0$ . To compare the experimental data with the theory, we draw dashed lines on top of the spin wave rays in Fig. 5.11 with the angles to the direction  $\mathbf{H}_0$  taken from the inset of Fig. 5.10. This comparison shows that the theory predicts the radiation angle with very good accuracy. In fact, the experimentally obtained angle deviates noticeably from the calculated one only for the highest accessible frequency of 9.7 GHz. The reason for the reduced propagation angle is not clear at the moment. The experimentally found angle for the pattern in Fig. 5.11(d) is equal to about  $56^\circ$ , which is smaller than the minimum angle obtained from the theoretical spin wave dispersion spectrum for  $F = 9.7 \text{ GHz}$  (see Fig. 5.10). Therefore, this effect cannot be associated with small modifications of the spectrum due to anisotropy or nonuniformity of the internal magnetic field. Another interesting feature of the spin wave radiation seen in Fig. 5.11 is the strong dependence of the intrinsic structure of the radiation pattern on the excitation frequency. Though all the maps in Fig. 5.11 demonstrate a preferential radiation direction in agreement with the theory, the number of spin wave rays and their

spatial positions can change. We associate this fact with a nonlocal character of the dipolar magnetic fields produced by the spin waves. As was shown above, these long-range fields lead to a significant penetration of spin waves into the continuous film, even in the regime of total reflection. In the radiation regime they cause a strong nonadiabaticity of the spin wave conversion process at the junction between the waveguide and the continuous film. Since the influence of the dipolar fields is weaker for short-wavelength spin waves, one expects a simplification of the structure of the radiation patterns with the increase in the frequency. This is in agreement with the data of Fig. 6. For small frequencies (see Figs. 5.11(a) and 5.11(b)) the radiation patterns demonstrate a tail of the waveguide mode caused by its dipolar fields similar to that seen in Fig. 5.8(a). This tail serves as a radiation source for two or even four spin-wave rays. At higher frequencies (see Figs. 5.11(c) and 5.11(d)), the tail of the waveguide mode becomes less pronounced and the radiated rays start directly at the position of the junction between the waveguide and the continuous film.

Our experimental results show that in microscopic magnetic-film structures the spin-wave transformations at the junction between a patterned stripe waveguide and the continuous film have rather complex character because of the spatial variation of the demagnetizing fields and the specific anisotropy of the spin-wave dispersion characteristics. A simple analytical model can be used to describe the qualitative characteristics of the spin-wave radiation in such systems, but a deeper understanding of its particular properties demands the development of a more complete theory or numerical simulations. We believe that our experimental findings will stimulate such

developments in the future. Note added in proof. Recently, our attention was drawn to Ref. [150], where a similar geometry, albeit with macroscopic dimensions, was investigated.

#### 5.4 DEVIATION OF SPIN WAVES FROM EXPONENTIAL DECAY<sup>1</sup>

In this report, we investigated the propagation of magnetostatic surface spin waves (MSSW) in a continuous Py thin film excited by an asymmetric coplanar waveguide antenna. The spin waves were excited in the Damon-Eshbach [103] configuration, wherein a static magnetic field was applied parallel to the antenna and perpendicular to the propagation direction of the spin waves. While mapping the spatial dependence of the surface spin wave intensity, we observed a significant deviation from the simple exponential decay due to damping: an oscillatory signal is superimposed on top of the exponential decay. To model the observed complicated spatial dependent spin wave intensity, we use a closed-form expression that includes contributions from the propagating spin wave and a background magnetization with spatially uniform phase. This simplified closed-form model allows us to fit the experimental data and to extract several key parameters including the wave vectors, the group velocities, and the propagation lengths of the excited spin waves.

The device studied consists of a nominally 40-nm-thick Py film sputtered on a silicon substrate. The Py film is covered with a 240-nm-thick layer of SiO<sub>x</sub>, which isolates the film electrically from the antenna. An asymmetric coplanar waveguide antenna was defined using photolithography and fabricated by thermal deposition of 300 nm of gold. The antenna consists of a 12- $\mu\text{m}$ -wide signal line connected to a 6- $\mu\text{m}$ -wide ground line with a center-to-center distance of 13  $\mu\text{m}$ . The film is patterned in a square with 1 mm sides, and the antenna extends across the middle of the square. The spin wave excited by

---

<sup>1</sup> This discussion follows closely that in Ref. [151].

the antenna can be treated as 1-D propagation in a continuous film because the propagation length is much shorter than the dimensions of the sample. The device was placed in an in-plane static magnetic field parallel to the antenna with a strength of  $1000 \pm 50$  Oe measured with a Gaussmeter. The MSSWs are excited by the antenna and propagate away from it, as illustrated in Fig. 5.12. Using the micro-BLS technique described in Ref. [54], we measured the time-averaged spin wave intensity as a function of distance from the antenna.

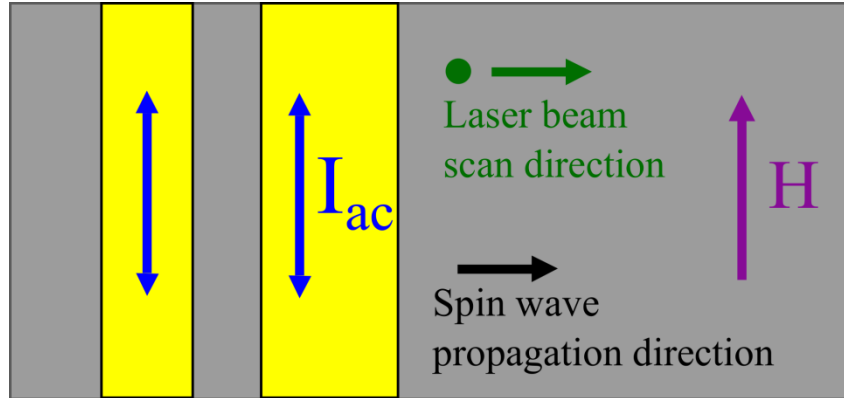


Figure 5.12. Illustration of the measured device and experimental configuration. A microwave current is driven through the asymmetric coplanar waveguide to excite spin waves, which propagate away from the antenna. Figure reproduced from Ref. [151].

To determine the frequency range over which spin waves can be excited effectively, the antenna response was first measured by recording the BLS intensity  $1 \mu\text{m}$  from the edge of the antenna as the frequency was scanned from 9 to 11 GHz. The frequency response is shown in Fig. 5.13. For this film thickness, only a single surface mode (i.e.,  $n=0$  mode) is excited by the microwave source. Higher order modes in the thickness direction are not excited in the frequency range investigated. The response

function measured using BLS intensity near the antenna does not exactly coincide with the amount of power transferred from the antenna into spin waves since the spatial intensity pattern varies with the excitation frequency. Nevertheless, the approximate response function presented in Fig. 5.13 allowed us to choose a reasonable scan range from 9.8 GHz to 10.5 GHz in steps of 0.1 GHz.

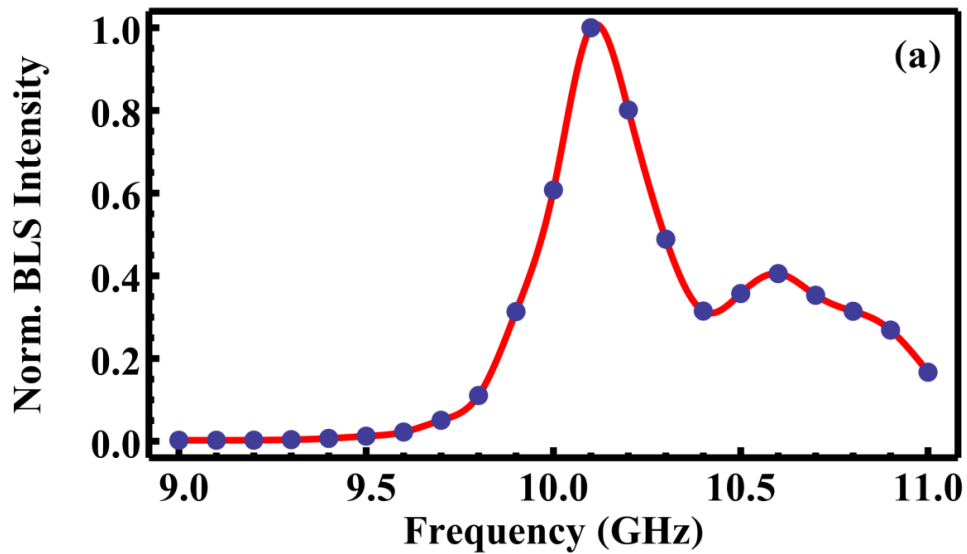


Figure 5.13. Antenna response as a function of frequency. The spin wave intensity is measured at a point 1  $\mu\text{m}$  from the edge of the antenna. The data points are shown in blue and the red line is only an interpolation to guide the eye. The peak indicates the resonance condition of the antenna with the spin wave response. Figure reproduced from Ref. [151].

At 9.8 and 9.9 GHz, propagating spin waves were not excited and the intensity of the measured magnetization decayed monotonically because these frequencies are below the ferromagnetic resonance (FMR) frequency. The spatial intensity pattern on a logarithmic scale at 9.8 GHz is shown in Fig. 5.14. The spatial dependence can be modeled using a function of the form  $C \text{Log}(x/(x+a))+T$ , where the parameter  $a$

determines how quickly the intensity falls off with distance, and  $T$  is the background due to thermal spin waves. Fitting this form to the pattern obtained at 9.8 GHz yields  $a = 29 \mu\text{m}$  and  $T = 160$  in the arbitrary units for the BLS intensity used in the figures. The spatial dependence of the spin wave intensity measured at 9.9 GHz has approximately the same functional form as that measured at 9.8 GHz, which motivates us to apply the same logarithmic function as the background magnetization in the fits of the spin wave intensity patterns above the FMR frequency, as discussed below.

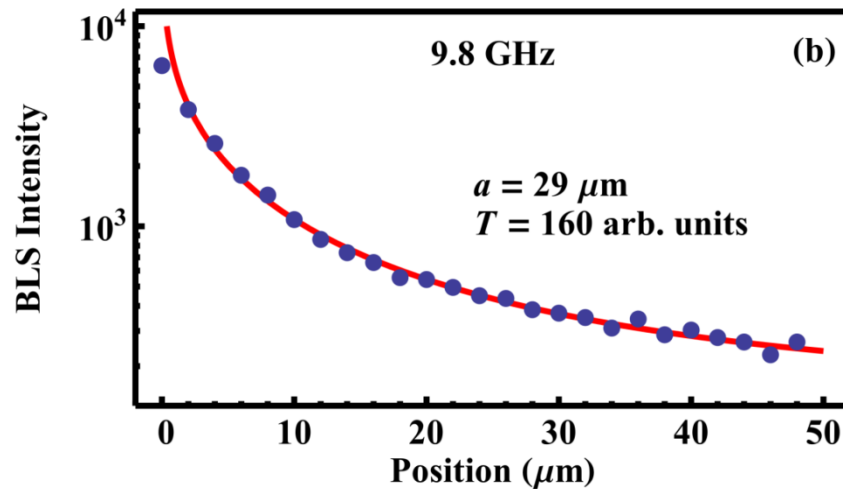


Figure 5.14. Spatial scan taken below resonance at 9.8 GHz. The data points are shown in blue and the red line is fit to a logarithmic function, as described in the text. Figure reproduced from Ref. [151].

The measured spin wave intensities as a function of distance from the edge of the antenna at several frequencies near the antenna resonance are shown in Fig. 5.15. The intensity of the excited MSSW is expected to decay exponentially away from the antenna. However, the observed spatial dependence is much more complicated. At frequencies above 10.2 GHz, a clear oscillatory behavior was observed in the spatial intensity

patterns shown in Figs. 5.15(a-d). The oscillations can be modeled as the interference between a propagating spin wave and a background magnetization. In contrast to the propagating MSSW with quickly decaying amplitude, this background magnetization has a constant phase and slowly decaying amplitude.

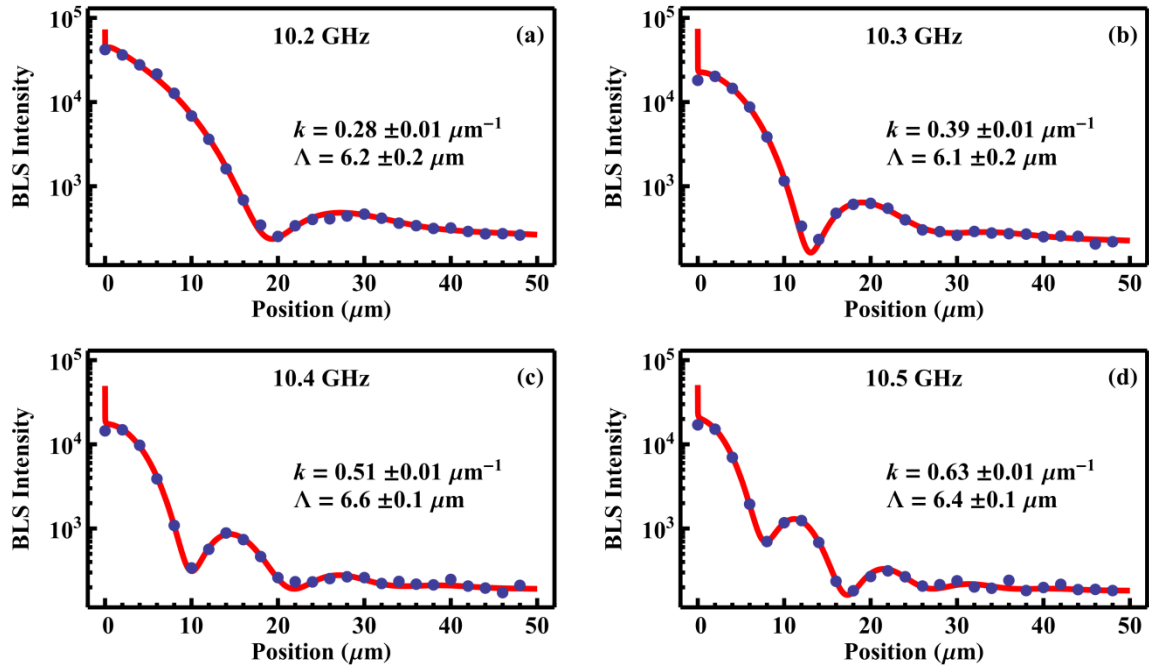


Figure 5.15. Oscillatory spatial intensity patterns for several frequencies as indicated. The measured BLS intensity on a Log scale as a function of the propagation distance (from the edge of the antenna). Simple exponential decay was not observed at any frequency. The blue points mark the measured BLS intensity and the red lines indicate the fit result. Figure reproduced from Ref. [151].

We used the closed-form formula shown below in Eq. (6.1), to fit the spatial intensity patterns at 10.0 GHz and above. The variables in bold font are the fitting parameters. We only consider the perpendicular component of the magnetization since it

dominates the BLS signal particularly at small angles of incident light in our experiments [119].

$$I_{BLS} = \langle m_z(x) \rangle^2 = \left| \mathbf{A} \left( \exp\left(ikx - \frac{x}{\mathbf{A}}\right) + \frac{1}{\mathbf{b}} \exp(i\phi) \text{Log}\left(\frac{x}{x+\mathbf{a}}\right) \right) \right|^2 + \mathbf{T} \quad (6.1)$$

The first term in the sum represents the propagating MSSW with a wave vector  $k$  and propagation length  $\mathbf{A}$ . The second term represents the contribution of the background magnetization with the logarithmic functional form determined by fitting the data presented in Fig. 5.14. The parameters  $\phi$  and  $\mathbf{b}$  respectively account for the phase and amplitude differences between the background magnetization and the spin wave. The constant background  $\mathbf{T}$  is due to the signal from the thermal spin waves and was determined by fitting the spatial intensity pattern in Fig. 5.14.

The proposed model provides excellent fits to the measurement and accurately reproduces the oscillations, as shown in Fig. 5.15(a-d). The fitting procedure converged well when a clear dip was observed in the data. Otherwise, the extracted wave vector has large errors, which leads to uncertainty in the other parameters. The key parameter, the spin wave propagation length  $\mathbf{A}$ , was extracted with small errors above 10.2 GHz. For large wave vectors, a simple exponential fit will suffice to extract the propagation length, but for smaller wave vectors the interference model is required.

To confirm that the wave vectors extracted from the fit are accurate, we compare the measured dispersion relation with a calculated dispersion relation [152] (Eq. (6.2)) using parameters extracted from independent measurements.

$$\omega^2 = \gamma^2 [(H_{ext} + 2\pi M_s)^2 - (2\pi M_s)^2 \exp(-2kL)] \quad (6.2)$$

Here,  $\gamma$  is the gyromagnetic ratio (2.93 MHz/Oe) and  $H_{ext} = 1,000$  Oe is the measured external magnetic field. The saturation magnetization  $M_s$  and Py layer thickness  $L$  were extracted by fitting the BLS spectra of thermal spin wave spectra as a function of the applied field (data not shown). These measurements gave  $4\pi M_s = 10,600$  Oe and  $L = 36$  nm, using an exchange constant of  $1.05 \times 10^{-6}$  erg/cm [153]. The saturation magnetization found for Py is consistent with other values found in the literature, which range between 9 and 11 kOe [154–156]. Figure 5.16 shows the calculated dispersion curve together with the values extracted from the spatial intensity patterns with our model. The agreement of the extracted wave vector with those predicted from the independently calculated dispersion relation is excellent except at 10.0 GHz, where the wavelength is too long for the fitting procedure to converge well.

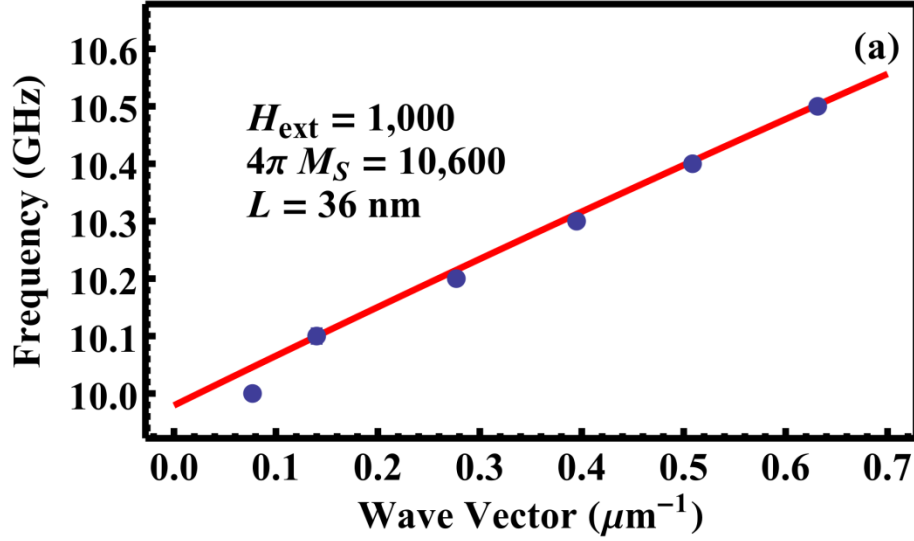


Figure 5.16. Experimentally determined dispersion relation (blue dots). The wave vector of the spin wave at a particular frequency was extracted from fit to the closed-form model. The red line represents the calculated dispersion curve using the parameters mentioned in the text. Figure reproduced from Ref. [151].

The dispersion relation allowed us to extract the group velocity for spin waves, which in turn, was used to calculate the propagation length via a simple equation shown in Eq. (6.3). The propagation length is expected to be independent of frequency for Damon-Eshbach waves in Py with the large wavelengths relevant in our experiments [90]. Assuming a damping constant of  $\alpha = 0.0074$  consistent with other measurements [73], [154], [157], the predicted propagation length using Eq. (6.3) is  $6.4 \mu\text{m}$ . This calculated propagation length agrees well with the experimental values except at the two lowest frequencies where the wave vector could not be determined accurately.

$$\Lambda_{calc} = v_g / (\alpha\gamma(H_{ext} + 2\pi M_S)) \quad (6.3)$$

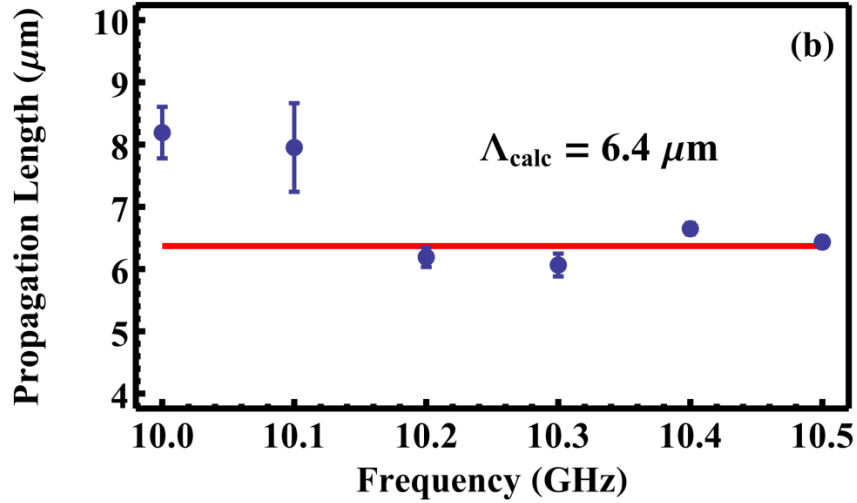


Figure 5.17. Experimentally determined spin wave propagation lengths (blue dots). The red line indicates the propagation length estimated using Eq. (6.3). Figure reproduced from Ref. [151].

To further confirm the validity of the applied model, we performed additional measurements on the same sample using spatially resolved ferromagnetic resonance scanning Kerr effect microscopy (SRFMR-SKEM), which measures the amplitude and phase of the excited magnetization [158]. In the SRFMR-SKEM experiments, the observed dynamic magnetization is consistent with the micro-BLS measurements: when exciting above the FMR frequency, oscillatory behavior in the intensity is observed, and below FMR the amplitude decays monotonically away from the antenna. Below FMR, the phase is constant, which confirms our previous claim that no propagating spin waves were excited in Fig. 5.14. Above FMR, the phase of the spin wave advances linearly as it propagates away from the antenna. However, at a distance far from the antenna, the oscillations disappear and the phase becomes constant, which is consistent with our

model of a quickly decaying spin wave present with a slowly decaying background magnetization with uniform phase.

The interference between the propagating spin wave with a background magnetization should be a common phenomenon. We performed numerical calculations following Eq. 36 in Ref. [108] and reproduced our experimental observation qualitatively. The calculations yield the background magnetization below the FMR frequency and the appearance of oscillatory signal upon the excitation of propagation spin waves. The calculations also show that the oscillations appear even with an infinitely thin excitation source, indicating that the oscillations are not a property of the antenna geometry, but rather a property of the magnetic susceptibility. We speculate why the oscillatory behavior has not been observed clearly and discussed explicitly until now. In Ref. [158], the thickness of the Py film was 100 nm, which leads to a much higher MSSW group velocity and thus a longer propagation length than in our case. Therefore, the background magnetization was always weaker than the propagating the spin wave in the range measured. Furthermore, in confined structures the interference pattern may be obscured by oscillations caused by other mechanisms such as mode beating [159] and reflections from edges and inhomogenities [123]. Additionally, this effect may not be apparent in YIG where the spin wave propagation length is hundreds of times longer than that in Py. If the propagation length is long enough, the amplitude of the background magnetization may only become comparable to the spin wave amplitude far from the antenna at which point the spin wave intensity could be too weak to be measured.

In summary, we have shown that the spatial intensity pattern of spin waves radiating from an antenna in a 1-D geometry is not necessarily simple exponential decay. Oscillations in the intensity pattern may arise for excitations above the FMR frequency. The oscillations can be modeled effectively as a propagating spin wave, with a wave vector given by the dispersion relation, that decays exponentially and a slowly decaying background magnetization with spatially uniform phase. Using a closed-form expression we were able to extract values for the spin wave propagation length and wave vectors from the observed intensity patterns. The accuracy of these values is confirmed by comparing them with independently calculated expressions.

## 5.5 MEASUREMENT OF MAGNON AND PHONON TEMPERATURES<sup>1</sup>

We demonstrate the use of the micro-Brillouin light scattering (micro-BLS) technique as a local temperature sensor for magnons in a Permalloy (Py) thin film and phonons in the glass substrate. When the Py film is uniformly heated, we observe a systematic shift in the frequencies of two thermally excited perpendicular standing spin wave modes. Fitting the temperature dependent magnon spectra allows us to achieve a temperature resolution better than 2.5 K. In addition, we demonstrate that the micro-BLS spectra can be used to measure the local temperature of magnons and the relative temperature shift of phonons across a thermal gradient. Such local temperature sensors are useful for investigating spin caloritronic and thermal transport phenomena in general.

Our experimental setup is illustrated in Fig. 5.18. The sample consists of a Py film sputtered on a glass substrate. The film is nominally 60 nm thick and coated with 10 nm of SiO<sub>x</sub> to prevent oxidation. The substrate is a rectangular piece of glass approximately 1 mm wide and 3 mm long. A magnetic field of 500 Oe was applied parallel to the short side of the sample. For the uniform heating measurements (Fig. 5.18(a)), the sample was mounted on a Peltier heater that was much larger than the sample. For the thermal gradient measurements (Fig. 5.18(b)), one end of the film was mounted on a resistive heater while the other end was mounted on a heat sink. A thermal gradient was applied along the length of the sample and perpendicular to the external magnetic field. A linearly polarized, single frequency laser at 532 nm was directed normal to the sample surface and focused to a spot size of ~1 μm. The average laser power applied was less

---

<sup>1</sup> This discussion follows closely that in Ref. [160].

than 2 mW to avoid overheating the Py film. The component of the backscattered light with orthogonal (parallel) polarization to the incoming beam was sent to a Sandercock-type multipass tandem Fabry-Pérot interferometer to resolve the inelastically scattered light from magnons (phonons). A computer controlled, imaging-based position correction algorithm ensured that the beam remained in focus throughout the measurement.

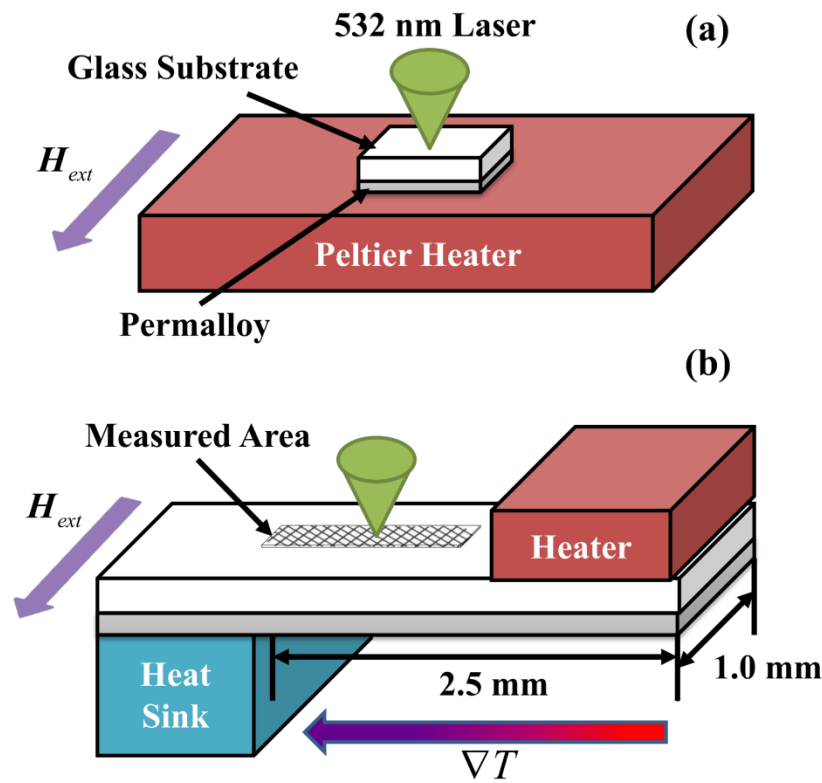


Figure 5.18. Experimental schematics.

(a) Uniform heating. (b) A thermal gradient is applied laterally to the substrate and perpendicular to the magnetic field. Figure reproduced from Ref. [160].

We first discuss how to interpret the micro-BLS magnon spectra, some examples of which are shown in Fig. 5.19(a). The spectra are dominated by two strong peaks corresponding to the first two perpendicular standing spin wave (PSSW) modes ( $n = 1, n$

= 2) of the Py film. The PSSW modes are characterized by sinusoidal amplitude profiles in the film thickness direction with the number of nodes corresponding to  $n$ , as illustrated in the inset of Fig. 5.19(a) [104]. The magnetostatic surface wave ( $n = 0$ ) mode is present but difficult to identify in the figure. It appears as a background surrounding the  $n = 1$  peak due to its broad linewidth. The same range of wavevectors are probed for all spin wave modes [119], which corresponds to different ranges of frequencies due to their different dispersion relations, leading to dissimilar linewidths in the BLS spectra. The linewidth of the  $n = 0$  mode is approximately five times broader than that of the  $n = 1$  mode according to the calculated dispersion relation [104]. For the rest of the paper, we focus on  $n = 1$  and  $n = 2$  modes because their narrow linewidths lend themselves as sensitive temperature sensors.

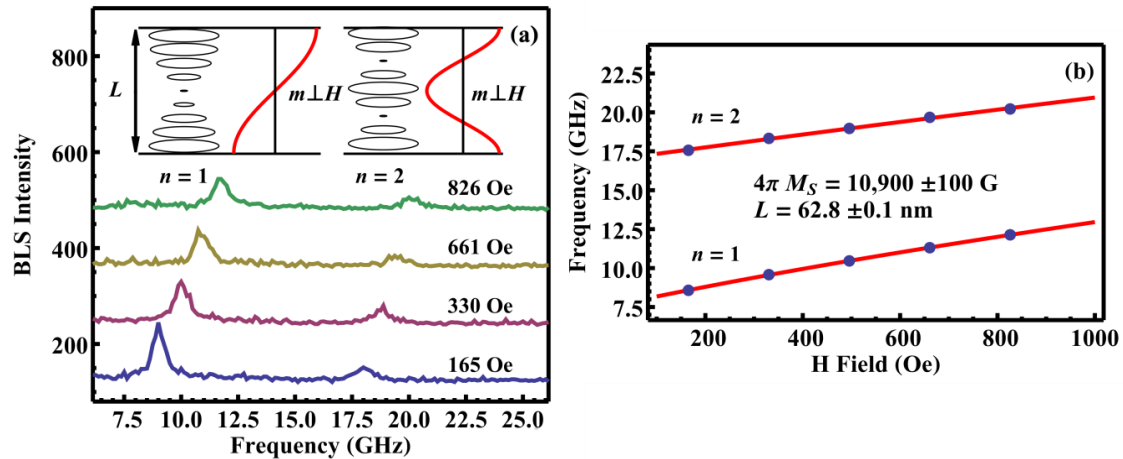


Figure 5.19. Magnetic field dependent thermal magnon spectra. (a) Two PSSW modes are observed ( $n = 1$  and  $n = 2$  modes). The insets illustrate the behavior of the dynamic magnetization in the thickness direction of the film. The ellipses show the path traced out by the dynamic components of the magnetization, and the red sinusoidal curves represent the amplitudes of one of the dynamic components. (b) Fitting the mode frequencies with the dispersion relation allows us to determine the saturation magnetization at room temperature. Figure reproduced from Ref. [160].

For our experiments with normal incident light, the frequencies of the PSSW modes can be calculated according to Eq. (6.4) [161],

$$\omega_n = \gamma \sqrt{\left(H_{ext} + \frac{2A}{M_S} \left(\frac{n\pi}{L}\right)^2\right) \left(H_{ext} + \frac{2A}{M_S} \left(\frac{n\pi}{L}\right)^2 + 4\pi M_S\right)} \quad (6.4)$$

where  $n$  is the number of nodes of the PSSW mode in the thickness direction,  $\gamma$  is the gyromagnetic ratio (2.93 MHz/Oe),  $A$  ( $\sim 1.0 \times 10^{-6}$  erg/cm at  $\sim 300$  K) [153] is the exchange constant,  $H_{ext}$  is the applied external field,  $L$  is the thickness of the ferromagnetic film, and  $M_S$  is the saturation magnetization. The temperature dependence of the exchange constant and saturation magnetization cause the mode frequency to vary with temperature. To confirm our interpretation of the magnon modes, we extract the peak positions from the spectra as the external field is varied. A few examples of the raw magnon spectra at different external fields are shown in Fig. 5.19(a). The peaks corresponding to the PSSW modes are fit with Lorentzian lineshapes, and the extracted peak positions are shown in Fig. 5.19(b). We fit the extracted values to Eq. (6.4) to obtain the saturation magnetization and the film thickness. The parameters obtained from the fitting are  $L = 62.8 \pm 0.1$  nm and  $4\pi M_S = 10,900 \pm 100$  Oe. The value for the saturation magnetization agrees well with those found in the literature for Py at room temperature [155], [156].

We then calibrated how the magnon frequencies shift as a function of temperature when the sample is heated uniformly, as shown in Fig. 5.20. The magnon frequency was extracted by fitting each PSSW peak in the BLS intensity with a Lorentzian lineshape, as

for the magnetic field dependent measurements. At each temperature, 24 independent measurements (for a total measurement time of two hours) were taken. The measurements were fit individually and the centers of the peaks were averaged. The error in frequency quoted for each temperature is the standard deviation of the mean. Over the temperature range studied, the frequency decreases linearly with increasing temperature due to the reduced saturation magnetization and exchange constant at higher temperatures. Linear fits to the data yield slopes of  $(-8.4 \pm 0.4) \times 10^{-3}$  GHz/K and  $(-16.1 \pm 0.8) \times 10^{-3}$  GHz/K for the  $n = 1$  and  $n = 2$  modes, respectively. The average error in the frequencies for the two modes are 0.02 GHz for  $n = 1$  and 0.05 GHz for  $n = 2$ . Therefore, the measured temperature sensitivities are about 2.4 K and 3.1 K for the  $n = 1$  and  $n = 2$  modes, respectively. The temperature sensitivities quoted in this study can be further improved simply by extending the measurement time, but the measured values already compare favorably with other nanoscale thermometry techniques [162].

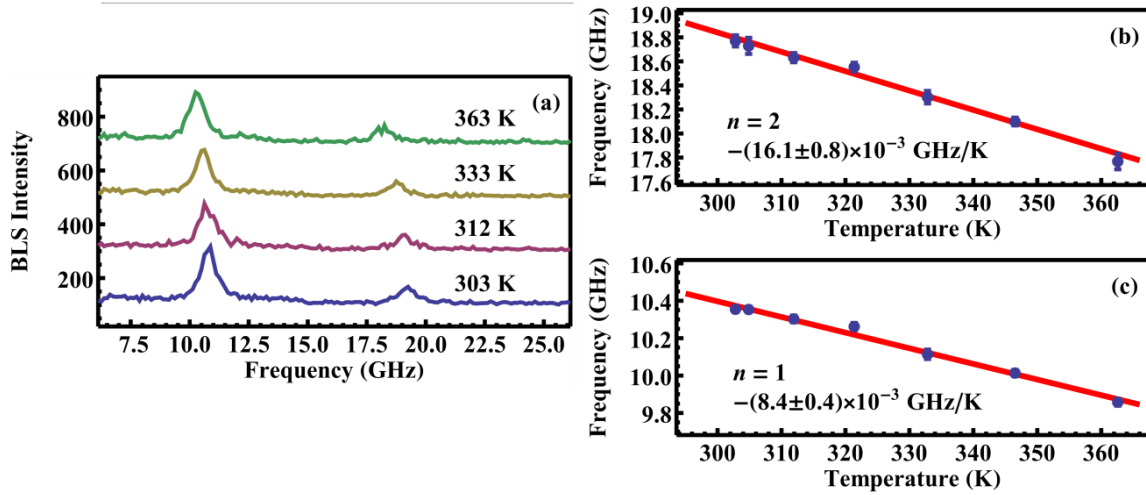


Figure 5.20. Temperature dependent thermal magnon spectra in a uniformly heated film. (a) Thermal magnon spectra with increasing temperature from the bottom to the top. Extracted magnon frequencies as a function of temperature for the (b)  $n = 1$  and (c)  $n = 2$  modes. The solid lines are linear fits, which allow us to determine the frequency shift as a function of temperature. Figure reproduced from Ref. [160].

We now investigate the feasibility of using the BLS spectra as a local magnon temperature sensor. To do so, we establish an in-plane temperature gradient by mounting the sample to a heater and heat sink, as illustrated in Fig. 5.18(b). We measure the magnon spectra at different locations along the temperature gradient by moving the sample on a motorized stage in 10 steps of  $160 \mu\text{m}$  each. We performed 24 independent measurements at each position, averaged the peak positions fitted with a Lorentzian lineshape, and quoted the standard deviation of the peak positions as the error bar. The frequency of the PSSW modes can be used as a temperature sensor for the local magnon temperature when compared to the frequency calibration performed on the uniformly heated film, as shown in Fig. 5.21. To account for the spatial variation of the magnon

frequencies due to spatially non-uniform properties of the film, we subtracted the measured magnon frequencies at each location without the thermal gradient from those with the thermal gradient. The resulting magnon frequency shifts for the  $n = 2$  and  $n = 1$  PSSW modes are displayed in Figs. 5.21(a) and 5.21(b), respectively. The spatial dependence of the magnon spectra corresponds to a linear temperature profile, as expected in this simple geometry. We fit the frequency shifts to a linear function and obtain shifts of  $(-8.9 \pm 1.3) \times 10^{-2}$  GHz/mm for the  $n = 1$  mode and  $(-20 \pm 2) \times 10^{-2}$  GHz/mm for the  $n = 2$  mode. Using the uniform heating data, the measured frequency shifts correspond to a  $-10.6 \pm 1.2$  K/mm temperature gradient between the hot and the cold ends for the  $n = 1$  mode and  $-12.6 \pm 1.2$  K/mm as measured with the  $n = 2$  mode. We note that the temperature gradients extracted from the two PSSW modes are consistent.

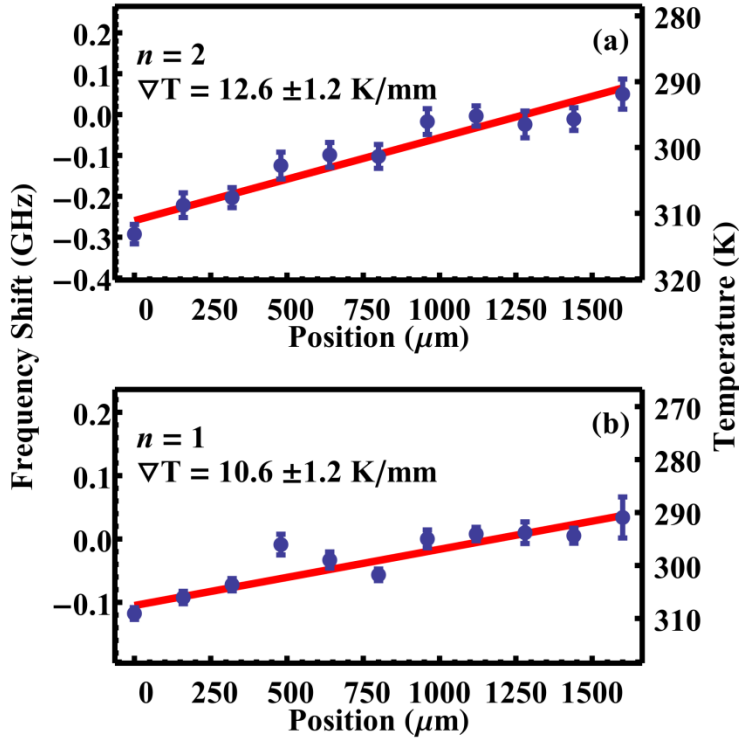


Figure 5.21. Extracted magnon temperature along the thermal gradient. Temperatures are measured for the (a)  $n = 1$  and (b)  $n = 2$  modes. The magnon frequency without a thermal gradient is subtracted from that with the thermal gradient to calculate the frequency shift, and a frequency shift of zero corresponds to room temperature. The temperature scale is obtained by comparing the magnon frequencies to those obtained in the uniformly heated film. The approximate linear shift in magnon frequency is consistent with a linearly varying temperature profile. Figure reproduced from Ref. [160].

To complement the magnon temperature measurement, we measure the acoustic phonon spectra of the glass substrate. The spectrum contains one peak corresponding to the frequency of the acoustic phonons in glass with wave vectors of  $4\pi N/\lambda$ , where  $\lambda$  is the laser wavelength and  $N$  is the index of refraction at the laser wavelength. Assuming  $N = 1.5$ , the measured frequency of 35 GHz implies a speed of sound of 6 km/s, which is quite reasonable for glass. We first calibrated the change in the phonon spectra as a

function of temperature under uniform heating conditions with the setup shown in Fig. 1(a). Unlike the magnon spectra, the phonon frequency did not shift as the temperature was varied. Instead, a systematic increase in the intensity of the phonon peak was observed (Fig. 5(a)) as the temperature was raised. Because the ratio between the phonon energy and  $kT$  is small, the Bose-Einstein distribution for the phonon mode is reduced to the classical limit that depends linearly on temperature, i.e.,  $\langle n \rangle = 1/(\exp(\hbar\omega/kT) - 1) \approx kT/\hbar\omega$ . Consequently, the intensity of the phonon peak in the BLS spectra depends linearly on temperature, as shown in Fig. 5(b). The intensities plotted in Fig. 5(b) are the averaged values from 24 measurements with the standard deviation displayed as the error bar. A linear fit yields that the phonon intensity increased by  $22 \pm 2$  % as the temperature increased from 296 K to 360 K, also an increase of 22 %. The linear fit yields a slope of  $0.35 \pm 0.03$  %/K. To map out the local temperature of the sample with a thermal gradient, we subtracted the intensities at each point with and without the thermal gradient to compensate for spatial non-uniformities in optical properties of the substrate. This procedure allows us to obtain a relative temperature shift for the phonons along the temperature gradient. The data shown in Fig. 5(c) is fit with a linear function with a slope of  $6.3 \pm 1.1$  %/mm. Using the slope obtained from the uniform heating data, this change in BLS intensity of the phonon mode implies a temperature gradient of  $18 \pm 3$  K/mm over the region measured, which is somewhat larger than the value extracted from the magnon spectra but still within two standard deviations. The larger temperature change in the phonons may be partially explained by the fact that the heater is attached to the side of

the substrate opposite from the Py film. Thus, a vertical thermal gradient may exist across the thickness of the substrate.

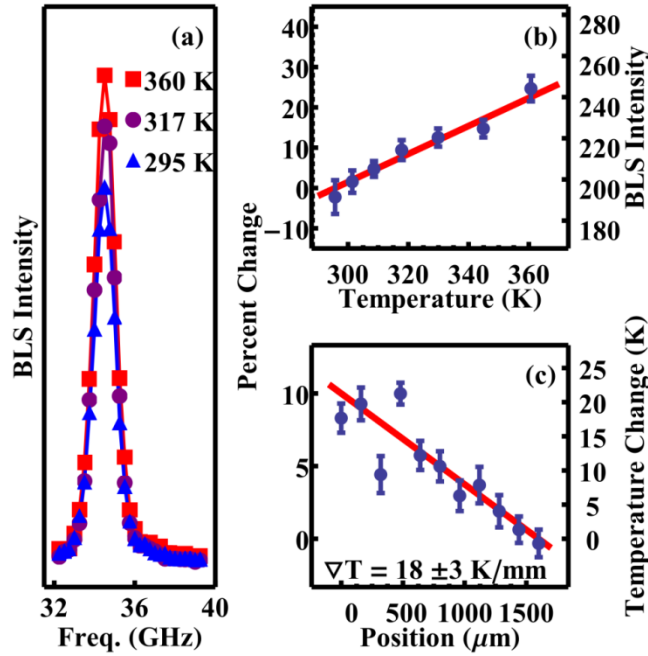


Figure 5.22. Phonon temperature measurements.

(a) Phonon spectra of the glass substrate collected at three different temperatures under uniform heating, which shows how the peak intensity increases as the temperature increases. (b) Percent change of the intensity of the phonon peak as the temperature was increased under uniform heating. (c) Percent change of the intensity as the beam was scanned along the temperature gradient, which shows a linearly varying temperature profile. The change in temperature relative to that measured at the furthest point from the heater is shown on the right axis. Figure reproduced from Ref. [160].

Our experiments demonstrate that the BLS spectra can be used as local temperature sensors for magnons and phonons. The frequency shift of magnon spectra provides an absolute temperature scale. In the case of the phonon, relative temperature changes were measured based on the changes in BLS intensity. We note that relative temperature change is of significant interest in measuring thermal properties. For

example, a micro-Raman technique has been used to measure relative temperature change in suspended graphene sheets from which the thermal conductivity of graphene was determined [163], [164]. Local magnon and phonon temperature sensors may be applied to investigate spin caloritronic and thermal transport phenomena. For example, a key assumption in the current understanding of thermally driven spin currents is that magnons temperature may not reach thermal equilibrium with the phonons locally. This difference between the phonon and magnon temperatures underlies the so called “phonon-magnon drag” that leads to the directional magnon transport or spin current in magnetic insulators and semiconductors [165–168]. Direct experimental confirmation of this phenomenon is currently lacking most likely due to the small temperature difference between these two temperatures in a sample with a modest temperature gradient [169]. Further improvement in the BLS measurement sensitivity of the magnon and phonon temperatures and the use of a large temperature gradient may help to clarify the fundamental mechanism responsible for thermally driven spin currents. In addition, to investigate thermal transport in a non-magnetic microstructure, a thin magnetic metal film may be deposited on the top of the microstructure and used as a local temperature sensor. Moreover, the phonon temperature obtained from the BLS spectra is that of the low-frequency acoustic phonons. In comparison, micro-Raman spectroscopy can be used to obtain the optical phonon temperature. Hence, the combination of these two techniques can be used to investigate highly non-equilibrium phonon transport, such as the hot optical phonon phenomena predicted in silicon and carbon nanotube-based electronic devices [170], [171].

## Chapter 6: Conclusions

### 6.1 SUMMARY OF WORK COMPLETED

The research discussed in this dissertation was motivated by a need to understand how to control and to image magnetic dynamics for possible applications in spintronic devices. To this end, we constructed a  $\mu$ -BLS system to map spin wave intensities with a spatial resolution of approximately 300 nm. BLS spectroscopy is an excellent method for measuring magnetization dynamics in the frequency domain. Being an optical method, it is nondestructive and permits spatial scanning. Furthermore, because the frequency filtering is accomplished optically, incoherent dynamics such as thermally excited spin waves and phonons can be detected, which are important for thermal transport. Currently, there are only four research groups including ours who use this technique to study magnetization dynamics.

One of the most important components of the  $\mu$ -BLS system is the software control system. It must be capable of correcting the slow drift in the scan position due to temperature changes in the laboratory and other sources of mechanical drift to maintain positioning accuracy better than 100 nm over the course of scans that may take several days. Our control software was written in house with the exception of the program for controlling the interferometer. We have demonstrated the ability to maintain accurate positioning using a software routine that employs optical feedback from a CCD camera. By using a plugin architecture, with plugins for each device or function, the scan can be easily extended and configured. In the event of a problem with a scan, monitor plugins can detect pause the scan, take corrective action, then resume the scan. If the situation

cannot be resolved by the program, the operator can be notified via email or text message. Additional instruments connected by computers that may be spread across a network can be controlled with our system.

Even before our BLS system was constructed, we were able to contribute to the understanding of spin wave propagation and scattering in confined structures. We fabricated devices consisted of waveguides etched out of a continuous film of permalloy with a microstrip antenna deposited on top to excite spin waves. We mapped the spin wave intensity in these devices using the  $\mu$ -BLS system of Prof. Demokritov at the University of Muenster. One device consisted of a 2  $\mu\text{m}$ -wide waveguide with a hole etched in the center. We found that the hole led to scattering of the fundamental waveguide mode into higher order modes. This result is of interest for its possible applications to controlling spin waves and as it relates to magnonic crystals where scattering from periodic disturbances crates bandgaps. Another device studied consists of a waveguide emptying into a continuous film. We found that if frequency overlaps with the allowed spin wave band in the continuous film, the spin waves will spread into the continuous film, but will propagate in two beams with an opening angle determined by the anisotropy of the dispersion relation. This offers the possibility of controlling the direction of spin wave propagation in continuous films through the anisotropic dispersion rather than confinement in a waveguide. As recent example of how this effect can be put to use, the authors of Ref. [172] utilized the anisotropic propagation characteristics of dipole coupled spin waves to obtain subwavelength imaging of a grating similar to what has been shown for anisotropic optical metamaterials.

With our  $\mu$ -BLS system we have explored fundamental issues related to spin wave propagation, such as the presence of a background magnetization that interferes significantly with the propagating spin wave when the damping is high enough and group velocity low enough. Our device consisted of a coplanar antenna on a continuous film of permalloy, which allowed us to excite MSSW waves propagating in one dimension. The interference resulted in oscillations in the spatial intensity pattern of the spin waves as they propagated away from the antenna. We were able to extract the spin wave vector, group velocity, and propagation length using a simple expression that modeled the background magnetization together with the propagating spin wave. We also showed using a numerical calculation that the background is intrinsic to the susceptibility. This result was surprising because it was typically thought that the background originates from the Oersted field of the excitation antenna. Rather one can consider the background magnetization as a near field effect of the magnetization field. This means that the presence of the oscillations is not strongly dependent on the specific geometry of the excitation. We may investigate this issue further by studying devices with different antenna geometries. We believe that this effect is the reason that serpentine antennas on thin permalloy film devices do not select a specific wave vector as well as expected.

We have also demonstrated the ability of our system to measure phonon and magnon temperatures over a thermal gradient. Measuring temperature changes over submicron lengths is of significant interest for measuring the thermal properties of basic materials and fabricated structures. With the ability to measure both magnons and phonons we are able to investigate nonequilibrium situations where the magnon and

phonon baths may not be in equilibrium. We showed that the magnon temperature can be extracted from the dependence of its frequency on the temperature. The frequency shifts because the magnon dispersion is dependent on the magnetization and exchange constant, which are both functions of temperature. Using this method, we were able to extract the magnon temperature with an accuracy of 2.5 K, which can easily be improved by increasing the acquisition time. We also demonstrated that the phonon temperature can be measured by the intensity of the BLS signal. In the GHz regime, the Boltzman distribution implies that the energy in the mode which is proportional to the BLS signal is proportional to  $kT$ . For the glass substrate we measured, the phonon temperature was more difficult to extract than the magnon frequency because many different effects can lead to variations in the temperature, but few can shift the frequency.

Unfortunately, our efforts to measure changes in the propagation lengths of spin waves due to the spin Hall effect and spin transfer torque have not yet been successful. The main difficulty is in fabricating devices where the antenna will not short to the waveguide when high current densities are applied to the waveguide. The insulating layer cannot be too thick because it could reduce the BLS signal collected and of course if it is too thin then the antenna shorts to the waveguide at high currents. Nevertheless, we have shown some changes in the resonant frequency of the antenna that are asymmetric in the direction of the applied current. However, the role of the Oersted field cannot be ruled out because the changes observed are slight and gradual, and the Oersted field has the same symmetry with respect to the applied DC voltage and magnetic field direction as the spin Hall effect would have. The ideal way to rule out the Oersted field would be to

observe an unambiguously large increase in the propagation length of the excited spin waves for one direction of current. Alternatively, any large sudden change the amplitude or frequency of the excitation antenna resonance that is asymmetric with current would be indicative of the spin Hall effect induced spin transfer torque. The difficulty with trying to make definitive statements involving small gradual changes is that the Oersted field of the DC current in the waveguide can alter the mode structure of the spin waves and perhaps increase their amplitude near the surface of the film. Work on this project is ongoing.

## 6.2 WORKS PUBLISHED OR PRESENTED

The following is a list of works presented or published.

- **D. R. Birt**, K. An, A. Weathers, L. Shi, and M. Tsoi, “Brillouin light scattering spectra as local temperature sensors for thermal magnons and acoustic phonons”, *Applied Physics Letters*, **102**, 082401 (2013).
- **D. R. Birt**, K. An, M. Tsoi, S. Tamaru, D. Ricketts, K. L. Wong, P. K. Amiri, K. L. Wang, and X. Li, “Deviation from exponential decay for spin waves excited with a coplanar waveguide antenna”, *Applied Physics Letters*, **101**, 252409 (2012).
- V. E. Demidov, S. O. Demokritov, **D. R. Birt**, B. O’Gorman, M. Tsoi, and X. Li, “Radiation of spin waves from the open end of a microscopic magnetic-film waveguide”, *Physical Review B*, **80**, 014429 (2009).
- **D. R. Birt**, B. O’Gorman, M. Tsoi, X. Li, V. E. Demidov, and S. O. Demokritov, “Diffraction of spin waves from a submicrometer-size defect in a microwaveguide”, *Applied Physics Letters*, **95**, 122510 (2009).
- Presentation: **D. R. Birt**, K. An, M. Tsoi, S. Tamaru, D. Ricketts, K. L. Wong, P. K. Amiri, K. L. Wang, and X. Li, “Oscillatory Spatial Intensity Pattern for Spin Waves Excited with a Coplanar Waveguide Antenna”, presented at the 12th Joint Magnetism and Magnetic Materials/Intermag Conference Chicago, IL, Jan. 2013.
- Poster: **D. R. Birt**, V. E. Demidov, S. O. Demokritov, B. O’Gorman, M. Tsoi, and X. Li, “Radiation of spin waves from the open end of a microscopic magnetic-film waveguide”, presented at the 11th Joint Magnetism and Magnetic Materials/Intermag Conference Washington, D.C., Jan. 2010.
- Poster: **D. R. Birt**, B. O’Gorman, M. Tsoi, X. Li, V. E. Demidov, and S. O. Demokritov “Diffraction of spin waves from a submicrometer-size defect in a micro-waveguide”, presented at the 11th Joint Magnetism and Magnetic Materials/Intermag Conference Washington, D.C., Jan. 2010.

### 6.3 OUTLOOK

The original goal of this project was to observe an increase in the propagation length of spin waves resulting from the decrease in damping due to STT effects. Unfortunately, our efforts have not yet been successful. We believe our main limitation has been the breakdown of our devices before the critical current can be achieved. No group has yet observed a change in the attenuation of spin waves, although electrical measurements have demonstrated the amplification of uniform precession in a magnetic strip due to STT and the decreased attenuation of standing modes in confined structures has been observed. We believe we are close to observing some effect; however, we are not sure how large the effect will be. It is not clear how the STT will affect the propagation of a single mode of a microstrip, where a continuum of modes exists. Another interesting project would be to replace the gold antennas used to excite spin waves with platinum strips carrying direct currents. Spin waves should be excited by the STT generated from the spin Hall effect. It would be especially interesting to study the coupling and phase relation between two Pt strips separated by some distance.

We have succeeded in building a general purpose measurement system for characterizing the propagation of spin waves with spatial resolution better than 300 nm. We have also demonstrated that our system is useful for measuring both the magnon and phonon temperatures. This ability allows us to consider measurements for thermal transport studies, which are currently not being pursued by other micro-BLS groups. The simple addition of a Raman spectrometer to our setup would be beneficial for such measurements. In the past 6 months we have published two papers and it should be

possible for us to continue to publish at the same rate. Within a few years it should be possible for our group to publish high impact publications as regularly as some of the other micro-BLS groups. Perhaps we could even have an advantage with our easy access to fabrication facilities. One of the main fabrication techniques we have not yet employed is  $\text{Ar}^+$  milling. It is the ideal method for fabricating structures in magnetic films since it produces the best quality edges. Liftoff typically results in jagged edges, and the  $\text{Ga}^+$  ions from the FIB can alter the magnetic properties of the film near the edges.

Our system could be improved by adding phase and temporal resolution to the measurement of the BLS signal. Most micro-BLS groups have these capabilities and use them in their publications. These additions, although useful, would require a significant investment of time and money. There are other simpler additions that could be made to improve our measurement capabilities. Some improvements could be made to the microwave electronics. For example, it would be useful to employ microwave probes to better match the impedance of the connections to the sample and increase the power converted to spin waves. Additionally, the ability to split the microwave signal into two channels and adjust the phase relation between them would be useful for spin wave interference measurements. The ability to measure static MOKE signals would also be beneficial. With the static MOKE signal we could compare the spin wave spectrum to the state of the magnetization and study propagation in structures where the magnetization is nonuniform.

## Bibliography

- [1] S. A. Wolf and D. Treger, "Spintronics: a new paradigm for electronics for the new millennium," *IEEE Transactions on Magnetics*, vol. 36, pp. 2748–2751, 2000.
- [2] A. Wang and W. D. Woo, "Static Magnetic Storage and Delay Line," *Journal of Applied Physics*, vol. 21, p. 49, 1950.
- [3] K. Button, "Microwave ferrite devices: The first ten years," *IEEE Transactions on Microwave Theory and Techniques*, vol. MIT-32, pp. 1088–1096, 1984.
- [4] F. Jelezko and J. Wrachtrup, "Focus on diamond-based photonics and spintronics," *New Journal of Physics*, vol. 14, p. 105024, Oct. 2012.
- [5] S. Tehrani, E. Chen, M. Durlam, M. DeHerrera, J. M. Slaughter, J. Shi, and G. Kerszykowski, "High density submicron magnetoresistive random access memory (invited)," *Journal of Applied Physics*, vol. 85, p. 5822, 1999.
- [6] S. S. P. Parkin, M. Hayashi, and L. Thomas, "Magnetic domain-wall racetrack memory.," *Science*, vol. 320, pp. 190–194, Apr. 2008.
- [7] S. I. Kiselev, J. C. Sankey, I. N. Krivorotov, N. C. Emley, R. J. Schoelkopf, R. a Buhrman, and D. C. Ralph, "Microwave oscillations of a nanomagnet driven by a spin-polarized current.," *Nature*, vol. 425, pp. 380–383, 2003.
- [8] S. Urazhdin, N. Birge, W. Pratt, and J. Bass, "Current-Driven Magnetic Excitations in Permalloy-Based Multilayer Nanopillars," *Physical Review Letters*, vol. 91, p. 146803, 2003.
- [9] O. Prokopenko, I. Krivorotov, T. Meitzler, E. Bankowski, V. Tibkervich, and A. Slavin, "Spin-Torque Microwave Detectors.," in *Magnonics*, Springer, Berlin 2013, pp. 143–161.
- [10] S. Ishibashi, T. Seki, T. Nozaki, H. Kubota, S. Yakata, A. Fukushima, S. Yuasa, H. Maehara, K. Tsunekawa, D. D. Djayaprawira, and Y. Suzuki, "Large Diode Sensitivity of CoFeB/MgO/CoFeB Magnetic Tunnel Junctions," *Applied Physics Express*, vol. 3, p. 073001, 2010.
- [11] A. N. Kuchko, M. L. Sokolovskii, and V. V Kruglyak, "Spin wave spectrum of a magnonic crystal with an internally structured defect," *Physica B: Condensed Matter*, vol. 370, pp. 73–77, 2005.

- [12] M. P. Kostylev, A. A. Serga, T. Schneider, B. Leven, and B. Hillebrands, “Spin-wave logical gates,” *Applied Physics Letters*, vol. 87, p. 153501, 2005.
- [13] A. Khitun and K. L. Wang, “Nano scale computational architectures with Spin Wave Bus,” *Superlattices and Microstructures*, vol. 38, pp. 184–200, 2005.
- [14] C. Kittel, “Physical theory of ferromagnetic domains,” *Reviews of Modern Physics*, vol. 21, p. 541, 1949.
- [15] V. V Kruglyak, S. O. Demokritov, and D. Grundler, “Magnonics,” *Journal of Physics D: Applied Physics*, vol. 43, p. 264001, 2010.
- [16] G. Binasch, P. Grünberg, F. Saurenbach, and W. Zinn, “Enhanced magnetoresistance in layered magnetic structures with antiferromagnetic interlayer exchange,” *Physical Review B*, vol. 39, pp. 4828–4830, 1989.
- [17] M. Baibich and J. Broto, “Giant magnetoresistance of (001) Fe/(001) Cr magnetic superlattices,” *Physical Review Letters*, vol. 61, pp. 2472–2475, 1988.
- [18] E. Grochowski, “Emerging trends in data storage on magnetic hard disk drives,” *Datatech, ICG Publishing*, pp. 11–16, 1998.
- [19] “Nature Materials Insight: Spintronics,” *Nature Materials*, vol. 11, no. 5, 2012.
- [20] L. Berger, “Emission of spin waves by a magnetic multilayer traversed by a current,” *Physical Review B*, vol. 54, pp. 9353–9358, 1996.
- [21] J. Slonczewski, “Current-driven excitation of magnetic multilayers,” *Journal of Magnetism and Magnetic Materials*, vol. 159, pp. L1–L7, 1996.
- [22] M. Tsoi, a. Jansen, J. Bass, W.-C. Chiang, M. Seck, V. Tsoi, and P. Wyder, “Excitation of a Magnetic Multilayer by an Electric Current,” *Physical Review Letters*, vol. 80, pp. 4281–4284, 1998.
- [23] J. Katine, F. Albert, R. Buhrman, E. Myers, and D. C. Ralph, “Current-driven magnetization reversal and spin-wave excitations in Co /Cu /Co pillars,” *Physical Review Letters*, vol. 84, pp. 3149–52, 2000.
- [24] W. Rippard, M. Pufall, S. Kaka, S. Russek, and T. J. Silva, “Direct-Current Induced Dynamics in Co<sub>90</sub>Fe<sub>10</sub>/Ni<sub>80</sub>Fe<sub>20</sub> Point Contacts,” *Physical Review Letters*, vol. 92, p. 027201, 2004.

- [25] I. Krivorotov, D. V Berkov, N. Gorn, N. Emley, J. C. Sankey, D. C. Ralph, and R. Buhrman, “Large-amplitude coherent spin waves excited by spin-polarized current in nanoscale spin valves,” *Physical Review B*, vol. 76, p. 024418, 2007.
- [26] S. Kaka, M. R. Pufall, W. H. Rippard, T. J. Silva, S. E. Russek, and J. A. Katine, “Mutual phase-locking of microwave spin torque nano-oscillators,” *Nature*, vol. 437, pp. 389–92, 2005.
- [27] F. B. Mancoff, N. D. Rizzo, B. N. Engel, and S. Tehrani, “Phase-locking in double-point-contact spin-transfer devices,” *Nature*, vol. 437, pp. 393–395, 2005.
- [28] A. Ruotolo, V. Cros, B. Georges, a Dussaux, J. Grollier, C. Deranlot, R. Guillemet, K. Bouzehouane, S. Fusil, and A. Fert, “Phase-locking of magnetic vortices mediated by antivortices.,” *Nature Nanotechnology*, vol. 4, pp. 528–532, 2009.
- [29] J. Hirsch, “Spin Hall Effect,” *Physical Review Letters*, vol. 83, pp. 1834–1837, 1999.
- [30] Y. Kajiwara, K. Harii, S. Takahashi, J. Ohe, K. Uchida, M. Mizuguchi, H. Umezawa, H. Kawai, K. Ando, K. Takanashi, S. Maekawa, and E. Saitoh, “Transmission of electrical signals by spin-wave interconversion in a magnetic insulator.,” *Nature*, vol. 464, pp. 262–266, 2010.
- [31] K. Ando, S. Takahashi, K. Harii, K. Sasage, J. Ieda, S. Maekawa, and E. Saitoh, “Electric Manipulation of Spin Relaxation Using the Spin Hall Effect,” *Physical Review Letters*, vol. 101, p. 036601, 2008.
- [32] E. Edwards, H. Ulrichs, V. E. Demidov, S. O. Demokritov, and S. Urazhdin, “Parametric excitation of magnetization oscillations controlled by pure spin current,” *Physical Review B*, vol. 86, p. 134420, 2012.
- [33] L. Liu, C.-F. Pai, Y. Li, H. W. Tseng, D. C. Ralph, and R. A. Buhrman, “Spin-Torque Switching with the Giant Spin Hall Effect of Tantalum,” *Science*, vol. 336, pp. 555–558, 2012.
- [34] C.-F. Pai, L. Liu, Y. Li, H. W. Tseng, D. C. Ralph, and R. a. Buhrman, “Spin transfer torque devices utilizing the giant spin Hall effect of tungsten,” *Applied Physics Letters*, vol. 101, p. 122404, 2012.
- [35] G. E. W. Bauer, E. Saitoh, and B. J. van Wees, “Spin caloritronics.,” *Nature Materials*, vol. 11, pp. 391–399, 2012.

- [36] A. Slachter, F. L. Bakker, J.-P. Adam, and B. J. van Wees, “Thermally driven spin injection from a ferromagnet into a non-magnetic metal,” *Nature Physics*, vol. 6, no. 11, pp. 879–882, 2010.
- [37] K. Uchida, J. Xiao, H. Adachi, J. Ohe, S. Takahashi, J. Ieda, T. Ota, Y. Kajiwara, H. Umezawa, H. Kawai, G. E. W. Bauer, S. Maekawa, and E. Saitoh, “Spin Seebeck insulator,” *Nature Materials*, vol. 9, pp. 894–897, 2010.
- [38] M. Hatami, G. E. W. Bauer, Q. Zhang, and P. Kelly, “Thermal Spin-Transfer Torque in Magnetoelectronic Devices,” *Physical Review Letters*, vol. 99, p. 066603, 2007.
- [39] J. Slonczewski, “Initiation of spin-transfer torque by thermal transport from magnons,” *Physical Review B*, vol. 82, p. 054403, 2010.
- [40] T. Dunn and A. Kamenev, “Optimization of the current pulse for spin-torque switches,” *Applied Physics Letters*, vol. 98, p. 143109, 2011.
- [41] A. V. Nazarov, H. S. Cho, J. Nowak, S. Stokes, and N. Tabat, “Tunable ferromagnetic resonance peak in tunneling magnetoresistive sensor structures,” *Applied Physics Letters*, vol. 81, p. 4559, 2002.
- [42] A. N. Slavin and V. Tiberkevich, “Spin wave mode excited by spin-polarized current in a magnetic nanocontact is a standing self-localized wave bullet,” *Physical Review Letters*, vol. 95, p. 237201, 2005.
- [43] V. E. Demidov, S. Urazhdin, and S. O. Demokritov, “Direct observation and mapping of spin waves emitted by spin-torque nano-oscillators,” *Nature Materials*, vol. 9, p. 984, 2010.
- [44] M. Madami, S. Bonetti, G. Consolo, S. Tacchi, G. Carlotti, G. Gubbiotti, F. B. Mancoff, M. A. Yar, and J. Akerman, “Direct observation of a propagating spin wave induced by spin-transfer torque,” *Nature Nanotechnology*, vol. 6, pp. 635–638, 2011.
- [45] T. Schneider, A. A. Serga, B. Leven, B. Hillebrands, R. L. Stamps, and M. P. Kostylev, “Realization of spin-wave logic gates,” *Applied Physics Letters*, vol. 92, p. 022505, 2008.
- [46] K.-S. Lee and S.-K. Kim, “Conceptual design of spin wave logic gates based on a Mach-Zehnder-type spin wave interferometer for universal logic functions,” *Journal of Applied Physics*, vol. 104, p. 053909, 2008.

- [47] A. Chumak, P. Pirro, A. A. Serga, M. P. Kostylev, R. L. Stamps, H. Schultheiss, K. Vogt, S. J. Hermsdoerfer, B. Laegel, P. A. Beck, and B. Hillebrands, “Spin-wave propagation in a microstructured magnonic crystal,” *Applied Physics Letters*, vol. 95, p. 262508, 2009.
- [48] A. V. Chumak, V. S. Tiberkevich, A. D. Karenowska, A. A. Serga, J. F. Gregg, A. N. Slavin, and B. Hillebrands, “All-linear time reversal by a dynamic artificial crystal,” *Nature Communications*, vol. 1, p. 141, 2010.
- [49] S.-M. Seo, K.-J. Lee, H. Yang, and T. Ono, “Current-Induced Control of Spin-Wave Attenuation,” *Physical Review Letters*, vol. 102, pp. 147202–147204, 2009.
- [50] V. E. Demidov, S. Urazhdin, E. R. J. Edwards, and S. O. Demokritov, “Wide-range control of ferromagnetic resonance by spin Hall effect,” *Applied Physics Letters*, vol. 99, p. 172501, 2011.
- [51] C. W. Sandweg, Y. Kajiwara, K. Ando, E. Saitoh, and B. Hillebrands, “Enhancement of the spin pumping efficiency by spin wave mode selection,” *Applied Physics Letters*, vol. 97, p. 252504, 2010.
- [52] R. Iguchi, K. Ando, Z. Qiu, T. An, E. Saitoh, and T. Sato, “Spin pumping by nonreciprocal spin waves under local excitation,” *Applied Physics Letters*, vol. 102, p. 022406, 2013.
- [53] M. R. Freeman and J. F. Smyth, “Picosecond time-resolved magnetization dynamics of thin-film heads,” *Journal of Applied Physics*, vol. 79, p. 5898, 1996.
- [54] S. O. Demokritov and V. E. Demidov, “Micro-Brillouin Light Scattering Spectroscopy of Magnetic Nanostructures,” *Magnetics, IEEE Transactions on*, vol. 44, pp. 6–12, 2008.
- [55] Z. Zhang, P. C. Hammel, and P. E. Wigen, “Observation of ferromagnetic resonance in a microscopic sample using magnetic resonance force microscopy,” *Applied Physics Letters*, vol. 68, p. 2005, 1996.
- [56] A. Puzic, B. Van Waeyenberge, K. W. Chou, P. Fischer, H. Stoll, G. Schütz, T. Tyliczszak, K. Rott, H. Brückl, G. Reiss, I. Neudecker, T. Haug, M. Buess, and C. H. Back, “Spatially resolved ferromagnetic resonance: Imaging of ferromagnetic eigenmodes,” *Journal of Applied Physics*, vol. 97, p. 10E704, 2005.
- [57] A. A. Khajetoorians, S. Lounis, B. Chilian, a. Costa, L. Zhou, D. Mills, J. Wiebe, and R. Wiesendanger, “Itinerant Nature of Atom-Magnetization Excitation by Tunneling Electrons,” *Physical Review Letters*, vol. 106, p. 037205, Jan. 2011.

- [58] A. A. Khajetoorians, B. Baxevanis, C. Hübner, T. Schlenk, S. Krause, T. O. Wehling, S. Lounis, A. Lichtenstein, D. Pfannkuche, J. Wiebe, and R. Wiesendanger, “Current-driven spin dynamics of artificially constructed quantum magnets.,” *Science*, vol. 339, pp. 55–59, Jan. 2013.
- [59] N. Mecking, Y. Gui, and C.-M. Hu, “Microwave photovoltage and photoresistance effects in ferromagnetic microstrips,” *Physical Review B*, vol. 76, p. 224430, 2007.
- [60] F. Giesen, J. Podbielski, and D. Grundler, “Mode localization transition in ferromagnetic microscopic rings,” *Physical Review B*, vol. 76, p. 014431, 2007.
- [61] M. Bao, K. Wong, A. Khitun, J. Lee, Z. Hao, K. L. Wang, D. W. Lee, and S. X. Wang, “Determining wave vector and material property from the phase-shift of spin-wave propagation,” *Europhysics Letter*, vol. 84, p. 27009, 2008.
- [62] J. Sankey, P. Braganca, A. Garcia, I. Krivorotov, R. Buhrman, and D. C. Ralph, “Spin-Transfer-Driven Ferromagnetic Resonance of Individual Nanomagnets,” *Physical Review Letters*, vol. 96, p. 227601, 2006.
- [63] L. Liu, T. Moriyama, D. C. Ralph, and R. Buhrman, “Spin-Torque Ferromagnetic Resonance Induced by the Spin Hall Effect,” *Physical Review Letters*, vol. 106, p. 036601, 2011.
- [64] A. V. Chumak, A. A. Serga, M. B. Jungfleisch, R. Neb, D. A. Bozhko, V. S. Tiberkevich, and B. Hillebrands, “Direct detection of magnon spin transport by the inverse spin Hall effect,” *Applied Physics Letters*, vol. 100, p. 082405, 2012.
- [65] H.-J. Chia, F. Guo, L. M. Belova, and R. D. McMichael, “Two-dimensional spectroscopic imaging of individual ferromagnetic nanostripes,” *Physical Review B*, vol. 86, p. 184406, 2012.
- [66] H.-J. Chia, F. Guo, L. M. Belova, and R. D. McMichael, “Spectroscopic defect imaging in magnetic nanostructure arrays,” *Applied Physics Letters*, vol. 101, p. 042408, 2012.
- [67] I. Lee, Y. Obukhov, G. Xiang, A. Hauser, F. Yang, P. Banerjee, D. V Pelekhov, and P. C. Hammel, “Nanoscale scanning probe ferromagnetic resonance imaging using localized modes.,” *Nature*, vol. 466, pp. 845–848, 2010.
- [68] K. W. Chou, A. Puzic, H. Stoll, D. Dolgos, G. Schütz, B. Van Waeyenberge, A. Vansteenkiste, T. Tylicszak, G. Woltersdorf, and C. H. Back, “Direct observation

- of the vortex core magnetization and its dynamics,” *Applied Physics Letters*, vol. 90, p. 202505, 2007.
- [69] L. Bocklage, B. Krüger, R. Eiselt, M. Bolte, P. Fischer, and G. Meier, “Time-resolved imaging of current-induced domain-wall oscillations,” *Physical Review B*, vol. 78, p. 180405, 2008.
- [70] F. Wegelin, D. Valdaitsev, A. Krasnyuk, S. Nepijko, G. Schönhense, H. Elmers, I. Krug, and C. Schneider, “Magnetization dynamics in microscopic spin-valve elements: Shortcomings of the macrospin picture,” *Physical Review B*, vol. 76, p. 134410, 2007.
- [71] F. Fohr, Y. Fukuma, S. Kaltenborn, L. Wang, J. Hamrle, H. Schultheiß, A. Serga, H. Schneider, Y. Otani, and B. Hillebrands, “Optical detection of spin transport in non-magnetic metals,” *Arxiv preprint arXiv:1011.4656*, 2010.
- [72] J. Li, M.-S. Lee, W. He, B. Redeker, A. Remhof, E. Amaladass, C. Hassel, and T. Eimüller, “Magnetic imaging with femtosecond temporal resolution.,” *The Review of Scientific Instruments*, vol. 80, p. 073703, 2009.
- [73] S. Tamaru, J. Bain, R. van de Veerdonk, T. Crawford, M. Covington, and M. Kryder, “Measurement of magnetostatic mode excitation and relaxation in permalloy films using scanning Kerr imaging,” *Physical Review B*, vol. 70, p. 014416, 2004.
- [74] M. L. Schneider, J. M. Shaw, A. B. Kos, T. Gerrits, T. J. Silva, and R. D. McMichael, “Spin dynamics and damping in nanomagnets measured directly by frequency-resolved magneto-optic Kerr effect,” *Journal of Applied Physics*, vol. 102, p. 103909, 2007.
- [75] M. Madami, S. Tacchi, G. Gubbiotti, G. Carlotti, F. Montoncello, G. Capuzzo, L. Giovannini, F. Nizzoli, H. Tanigawa, and T. Ono, “Spin Modes in Elliptical Nanorings in the Vortex State: Two-Dimensional Mapping by Micro-Focused Brillouin Light Scattering,” *IEEE Transactions on Magnetics*, vol. 46, pp. 199–202, 2010.
- [76] V. E. Demidov, S. Urazhdin, E. Edwards, M. D. Stiles, R. D. McMichael, and S. O. Demokritov, “Control of Magnetic Fluctuations by Spin Current,” *Physical Review Letters*, vol. 107, p. 107204, 2011.
- [77] T. Sebastian, T. Brächer, P. Pirro, A. A. Serga, B. Hillebrands, T. Kubota, H. Naganuma, M. Oogane, and Y. Ando, “Nonlinear Emission of Spin-Wave

Caustics from an Edge Mode of a Microstructured  $\text{Co}_{0.2}\text{Mn}_{0.6}\text{Fe}_{0.4}\text{Si}$  Waveguide,” *Physical Review Letters*, vol. 110, p. 067201, 2013.

- [78] V. E. Demidov, M. Buchmeier, K. Rott, P. Krzysteczko, J. Münchenberger, G. Reiss, and S. O. Demokritov, “Nonlinear Hybridization of the Fundamental Eigenmodes of Microscopic Ferromagnetic Ellipses,” *Physical Review Letters*, vol. 104, p. 217203, 2010.
- [79] V. E. Demidov, J. Jersch, K. Rott, P. Krzysteczko, G. Reiss, and S. O. Demokritov, “Nonlinear Propagation of Spin Waves in Microscopic Magnetic Stripes,” *Physical Review Letters*, vol. 102, p. 177207, 2009.
- [80] S. Tacchi, F. Montoncello, M. Madami, G. Gubbiotti, G. Carlotti, L. Giovannini, R. Zivieri, F. Nizzoli, S. Jain, A. O. Adeyeye, and N. Singh, “Band Diagram of Spin Waves in a Two-Dimensional Magnonic Crystal,” *Physical Review Letters*, vol. 107, p. 127204, 2011.
- [81] P. Pirro, T. Bracher, K. Vogt, B. Obry, H. Schultheiss, B. Leven, and B. Hillebrands, “Interference of coherent spin waves in micron-sized ferromagnetic waveguides,” *arXiv*, vol. 7, pp. 2–7, 2011.
- [82] V. E. Demidov, J. Jersch, S. O. Demokritov, K. Rott, P. Krzysteczko, and G. Reiss, “Transformation of propagating spin-wave modes in microscopic waveguides with variable width,” *Physical Review B*, vol. 79, p. 054417, 2009.
- [83] V. E. Demidov, S. O. Demokritov, K. Rott, P. Krzysteczko, and G. Reiss, “Nano-optics with spin waves at microwave frequencies,” *Applied Physics Letters*, vol. 92, p. 232503, 2008.
- [84] G. Carlotti and G. Gubbiotti, “Magnetic properties of layered nanostructures studied by means of Brillouin light scattering and the surface magneto-optical Kerr effect,” *Journal of Physics: Condensed Matter*, vol. 14, pp. 8199–8233, 2002.
- [85] J. W. Lau and J. M. Shaw, “Magnetic nanostructures for advanced technologies: fabrication, metrology and challenges,” *Journal of Physics D: Applied Physics*, vol. 44, no. 30, p. 303001, 2011.
- [86] O. Büttner, M. Bauer, S. O. Demokritov, B. Hillebrands, Y. S. Kivshar, V. Grimalsky, Y. Rapoport, and A. N. Slavin, “Linear and nonlinear diffraction of dipolar spin waves in yttrium iron garnet films observed by space- and time-resolved Brillouin light scattering,” *Physical Review B*, vol. 61, p. 11576, 2000.

- [87] V. E. Demidov, S. Urazhdin, V. Tiberkevich, A. N. Slavin, and S. O. Demokritov, “Control of spin-wave emission from spin-torque nano-oscillators by microwave pumping,” *Physical Review B*, vol. 83, p. 060406(R), 2011.
- [88] F. Fohr, A. A. Serga, T. Schneider, J. Hamrle, and B. Hillebrands, “Phase sensitive Brillouin scattering measurements with a novel magneto-optic modulator,” *Review of Scientific Instruments*, vol. 80, p. 43903, 2009.
- [89] A. A. Serga, T. Schneider, B. Hillebrands, S. O. Demokritov, and M. P. Kostylev, “Phase-sensitive Brillouin light scattering spectroscopy from spin-wave packets,” *Applied Physics Letters*, vol. 89, p. 063506, 2006.
- [90] D. D. Stancil and A. Prabhakar, *Spin Waves: Theory and Applications*. New York: Springer, 2009, p. 355.
- [91] S. Chikazumi, *Physics of Ferromagnetism*, 2nd ed. New York: Oxford University Press, 1997.
- [92] T. M. Wallis, J. Moreland, and P. Kabos, “Einstein–de Haas effect in a NiFe film deposited on a microcantilever,” *Applied Physics Letters*, vol. 89, p. 122502, 2006.
- [93] G. Zolfagharkhani, A. Gaidarzhy, P. Degiovanni, S. Kettemann, P. Fulde, and P. Mohanty, “Nanomechanical detection of itinerant electron spin flip,” *Nature nanotechnology*, vol. 3, pp. 720–723, 2008.
- [94] S. Bretzel, G. E. W. Bauer, Y. Tserkovnyak, and A. Brataas, “Barnett effect in thin magnetic films and nanostructures,” *Applied Physics Letters*, vol. 95, p. 122504, 2009.
- [95] M. Matsuo, J. Ieda, E. Saitoh, and S. Maekawa, “Spin current generation due to mechanical rotation in the presence of impurity scattering,” *Applied Physics Letters*, vol. 98, p. 242501, 2011.
- [96] R. Matsumoto and S. Murakami, “Theoretical Prediction of a Rotating Magnon Wave Packet in Ferromagnets,” *Physical Review Letters*, vol. 106, p. 197202, 2011.
- [97] M. Matsuo, J. Ieda, and K. Harii, “Mechanical generation of spin current by spin-rotation coupling,” *arXiv preprint arXiv: 1301.1111*, pp. 1–5, 2013.
- [98] E. C. Stoner, “Atomic moments in ferromagnetic metals and alloys with non-ferromagnetic elements,” *The London, Edinburgh, and Dublin Philosophical Magazine and Journal of Science*, vol. 15, no. 101, pp. 1018–1034, 1933.

- [99] J. Slater, “The ferromagnetism of nickel,” *Physical Review*, vol. 57, p. 537, 1936.
- [100] D. Langreth and J. Wilkins, “Theory of spin resonance in dilute magnetic alloys,” *Physical Review B*, vol. 6, pp. 3189–3227, 1972.
- [101] W. F. Brown Jr, *Magnetostatic Principles in Ferromagnetism*. Amsterdam: North-Holland Pub. Co, 1962, p. 202.
- [102] L. A. L. E. Landau and E. Lifshitz, “On the theory of the dispersion of magnetic permeability in ferromagnetic bodies,” *Phys. Z. Sowjetunion*, vol. 8, pp. 101–114, 1935.
- [103] R. W. Damon and J. R. Eshbach, “Magnetostatic Modes of a Ferromagnetic Slab,” *Journal of the Physics and Chemistry of Solids*, vol. 19, pp. 308–320, 1961.
- [104] B. A. Kalinikos and A. N. Slavin, “Theory of dipole-exchange spin wave spectrum for ferromagnetic films with mixed exchange boundary conditions,” *Journal of Physics C: Solid State Physics*, vol. 19, p. 7013, 1986.
- [105] R. F. Soohoo, “General exchange boundary condition and surface anisotropy energy of a ferromagnet,” *Physical Review*, vol. 131, pp. 594–601, 1963.
- [106] K. Y. Guslienko, S. O. Demokritov, B. Hillebrands, and A. N. Slavin, “Effective dipolar boundary conditions for dynamic magnetization in thin magnetic stripes,” *Physical Review B*, vol. 66, p. 132402, 2002.
- [107] G. Gubbiotti, M. Conti, G. Carlotti, P. Candeloro, E. Di Fabrizio, K. Y. Guslienko, a Andre, C. Bayer, and a N. Slavin, “Magnetic field dependence of quantized and localized spin wave modes in thin rectangular magnetic dots,” *Journal of Physics: Condensed Matter*, vol. 16, pp. 7709–7721, Nov. 2004.
- [108] B. A. Kalinikos, “Excitation of propagating spin waves in ferromagnetic films,” *Microwaves, Optics and Antennas, IEE Proceedings H*, vol. 127, p. 4, 1980.
- [109] A. T. Young, “Rayleigh scattering,” *Physics Today*, vol. 35, p. 42, 1982.
- [110] A. Hubert and G. Traeger, “Magneto-optical sensitivity functions of thin-film systems,” *Journal of magnetism and magnetic materials*, vol. 124, pp. 185–202, 1993.
- [111] P. Johnson and R. Christy, “Optical constants of transition metals: Ti, v, cr, mn, fe, co, ni, and pd,” *Physical Review B*, vol. 9, pp. 5056–5070, 1974.

- [112] G. S. Krinchik and V. A. Artem'ev, "Magneto-optical Properties of Ni, Co, and Fe in the Ultraviolet Visible and Infrared Parts of the Spectrum," *Sov. Phys. JETP*, vol. 26, p. 1080, 1968.
- [113] P. Grünberg and F. Metawe, "Light scattering from bulk and surface spin waves in EuO," *Physical Review Letters*, vol. 39, 1977.
- [114] S. O. Demokritov and E. Tsymbal, "Light scattering from spin waves in thin films and layered systems," *Journal of Physics C: Solid State Physics*, vol. 6, pp. 7145–7188, 1994.
- [115] J. Cochran and J. Dutcher, "Calculation of the intensity of light scattered from magnons in thin films," *Journal of magnetism and magnetic materials*, vol. 73, p. 299, 1988.
- [116] J. Cochran, J. Rudd, W. Muir, B. Heinrich, and Z. Celinski, "Brillouin light-scattering experiments on exchange-coupled ultrathin bilayers of iron separated by epitaxial copper (001)," *Physical Review B*, vol. 42, no. 1, p. 508, 1990.
- [117] L. Giovannini, R. Zivieri, G. Gubbiotti, G. Carlotti, L. Pareti, and G. Turilli, "Theory of Brillouin cross section for scattering from magnetic multilayers: Second-order magneto-optic effect in Ni/Cu bilayers and trilayers," *Physical Review B*, vol. 63, p. 104405, 2001.
- [118] M. Buchmeier, H. Dassow, D. Bürgler, and C. Schneider, "Intensity of Brillouin light scattering from spin waves in magnetic multilayers with noncollinear spin configurations: Theory and experiment," *Physical Review B*, vol. 75, p. 185536, 2007.
- [119] J. Hamrle, J. Pištora, B. Hillebrands, B. Lenk, and M. Münzenberg, "Analytical expression of the magneto-optical Kerr effect and Brillouin light scattering intensity arising from dynamic magnetization," *Journal of Physics D: Applied Physics*, vol. 43, p. 325004, 2010.
- [120] R. E. Camley, P. Grünberg, and C. Mayr, "Stokes--anti-Stokes asymmetry in Brillouin scattering from magnons in thin ferromagnetic films," *Physical Review B*, vol. 26, p. 2609, 1982.
- [121] R. E. Camley and D. L. Mills, "Surface response of exchange-and dipolar-coupled ferromagnets: Application to light scattering from magnetic surfaces," *Physical Review B*, vol. 18, p. 4821, 1978.

- [122] V. E. Demidov, S. O. Demokritov, B. Hillebrands, M. Laufenberg, and P. P. Freitas, "Radiation of spin waves by a single micrometer-sized magnetic element," *Applied Physics Letters*, vol. 85, p. 2866, 2004.
- [123] D. R. Birt, B. O'Gorman, M. Tsoi, X. Li, V. E. Demidov, and S. O. Demokritov, "Diffraction of spin waves from a submicrometer-size defect in a microwaveguide," *Applied Physics Letters*, vol. 95, p. 122510, 2009.
- [124] K. Vogt, H. Schultheiss, S. Jain, J. E. Pearson, a. Hoffmann, S. D. Bader, and B. Hillebrands, "Spin waves turning a corner," *Applied Physics Letters*, vol. 101, p. 042410, 2012.
- [125] B. Obry, T. Meyer, P. Pirro, T. Brächer, B. Lägel, J. Osten, T. Strache, J. Fassbender, and B. Hillebrands, "Microscopic magnetic structuring of a spin-wave waveguide by ion implantation in a Ni<sub>81</sub>Fe<sub>19</sub> layer," *Applied Physics Letters*, vol. 102, p. 022409, 2013.
- [126] G. Gubbiotti, S. Tacchi, M. Madami, G. Carlotti, a O. Adeyeye, and M. P. Kostylev, "Brillouin light scattering studies of planar metallic magnonic crystals," *Journal of Physics D: Applied Physics*, vol. 43, p. 264003, 2010.
- [127] S. Tacchi, G. Duerr, J. Klos, M. Madami, S. Neusser, G. Gubbiotti, G. Carlotti, M. Krawczyk, and D. Grundler, "Forbidden Band Gaps in the Spin-Wave Spectrum of a Two-Dimensional Bicomponent Magnonic Crystal," *Physical Review Letters*, vol. 109, p. 137202, 2012.
- [128] V. E. Demidov, M. P. Kostylev, K. Rott, P. Krzysteczko, G. Reiss, and S. O. Demokritov, "Generation of the second harmonic by spin waves propagating in microscopic stripes," *Physical Review B*, vol. 83, p. 054408, 2011.
- [129] V. E. Demidov, S. O. Demokritov, G. Reiss, and K. Rott, "Effect of spin-polarized electric current on spin-wave radiation by spin-valve nanocontacts," *Applied Physics Letters*, vol. 90, p. 172508, 2007.
- [130] H. Ulrichs, V. E. Demidov, S. O. Demokritov, and S. Urazhdin, "Parametric excitation of eigenmodes in microscopic magnetic dots," *Physical Review B*, vol. 84, p. 094401, 2011.
- [131] V. E. Demidov, S. Urazhdin, and S. O. Demokritov, "Control of spin-wave phase and wavelength by electric current on the microscopic scale," *Applied Physics Letters*, vol. 95, p. 262509, 2009.

- [132] R. Y. Chiao and B. P. Stoicheff, “Brillouin Scattering in Liquids Excited by the He-Ne Maser,” *Journal of the Optical Society of America*, vol. 54, p. 1286, 1964.
- [133] L. Durvasula and R. Gammon, “Pressure-scanned three-pass Fabry-Perot interferometer,” *Applied Optics*, vol. 17, p. 3298, 1978.
- [134] J. R. Sandercock, “Trends in Brillouin scattering: studies of opaque materials, supported films, and central modes,” in *Light Scattering in Solids III*, Springer, 1979, pp. 173–206.
- [135] J. R. Sandercock, “High resolution, high contrast Fabry-Perot spectrometer,” U.S. Patent 40146141977.
- [136] A. Koreeda and S. Saikan, “Note: Higher resolution Brillouin spectroscopy by offset stabilization of a tandem Fabry-Pérot interferometer.,” *The Review of Scientific Instruments*, vol. 82, p. 126103, 2011.
- [137] J. R. Sandercock, “Simple stabilization scheme for maintenance of mirror alignment in a scanning Fabry-Perot interferometer,” *Journal of Physics E: Scientific Instruments*, vol. 9, p. 566, 1976.
- [138] C. Mack, *Fundamental Principles of Optical Lithography: The Science of Microfabrication*. Sussex: Wiley-Interscience, 2008, p. 534.
- [139] V. E. Demidov, S. O. Demokritov, K. Rott, P. Krzysteczko, and G. Reiss, “Mode interference and periodic self-focusing of spin waves in permalloy microstripes,” *Physical Review B*, vol. 77, p. 64406, 2008.
- [140] C. Bayer, J. Park, H. Wang, M. Yan, C. Campbell, and P. Crowell, “Spin waves in an inhomogeneously magnetized stripe,” *Physical Review B*, vol. 69, p. 134401, 2004.
- [141] A. Kozhanov, D. Ouellette, M. Rodwell, S. J. Allen, A. P. Jacob, D. W. Lee, and S. X. Wang, “Dispersion and spin wave ‘tunneling’ in nanostructured magnetostatic spin waveguides,” *Journal of Applied Physics*, vol. 105, p. 07D311, 2009.
- [142] M. P. Kostylev, A. A. Serga, T. Schneider, T. Neumann, B. Hillebrands, B. Leven, and R. L. Stamps, “Resonant and nonresonant scattering of dipole-dominated spin waves from a region of inhomogeneous magnetic field in a ferromagnetic film,” *Physical Review B*, vol. 76, p. 184419, 2007.

- [143] K. R. Smith, M. J. Kabatek, P. Krivosik, and M. Wu, “Spin wave propagation in spatially nonuniform magnetic fields,” *Journal of Applied Physics*, vol. 104, p. 043911, 2008.
- [144] B. Obry, V. I. Vasyuchka, A. V. Chumak, A. a. Serga, and B. Hillebrands, “Spin-wave propagation and transformation in a thermal gradient,” *Applied Physics Letters*, vol. 101, p. 192406, 2012.
- [145] V. E. Demidov, S. O. Demokritov, D. R. Birt, B. O’Gorman, M. Tsoi, and X. Li, “Radiation of spin waves from the open end of a microscopic magnetic-film waveguide,” *Physical Review B*, vol. 80, p. 014429, 2009.
- [146] K.-S. Lee, D.-S. Han, and S.-K. Kim, “Physical Origin and Generic Control of Magnonic Band Gaps of Dipole-Exchange Spin Waves in Width-Modulated Nanostrip Waveguides,” *Physical Review Letters*, vol. 102, pp. 127202–127204, 2009.
- [147] A. Chumak, a. a. Serga, B. Hillebrands, and M. P. Kostylev, “Scattering of backward spin waves in a one-dimensional magnonic crystal,” *Applied Physics Letters*, vol. 93, p. 022508, 2008.
- [148] Z. K. Wang, V. L. Zhang, H. S. Lim, S. C. Ng, M. H. Kuok, S. Jain, A. O. Adeyeye, Y. Minami, T. Yogi, K. Sakai, A. G. Jacobson, and Y. R. Shen, “Observation of frequency band gaps in a one-dimensional nanostructured magnonic crystal Millisecond Brillouin scattering spectroscopy Coherent Brillouin Spectroscopy,” *Applied Physics Letters*, vol. 94, pp. 83112–83113, 2009.
- [149] S. O. Demokritov, A. A. Serga, A. André, V. E. Demidov, M. P. Kostylev, B. Hillebrands, and A. N. Slavin, “Tunneling of Dipolar Spin Waves through a Region of Inhomogeneous Magnetic Field,” *Physical Review Letters*, vol. 93, p. 47201, 2004.
- [150] T. Schneider, A. A. Serga, C. Sandweg, and B. Hillebrands, “No Title,” in *Abstracts of the 52nd Annual Conference on Magnetism and Magnetic Materials*, 2007.
- [151] D. R. Birt, K. An, M. Tsoi, S. Tamaru, D. Ricketts, K. L. Wong, P. Khalili Amiri, K. L. Wang, and X. Li, “Deviation from exponential decay for spin waves excited with a coplanar waveguide antenna,” *Applied Physics Letters*, vol. 101, p. 252409, 2012.
- [152] A. G. Gurevich and G. A. Melkov, *Magnetization Oscillations and Waves*. CRC Press, 1996.

- [153] N. Smith, D. Markham, and D. LaTourette, “Magnetoresistive measurement of the exchange constant in varied-thickness permalloy films,” *Journal of Applied Physics*, vol. 65, p. 4362, 1989.
- [154] W. Hiebert, a. Stankiewicz, and M. Freeman, “Direct Observation of Magnetic Relaxation in a Small Permalloy Disk by Time-Resolved Scanning Kerr Microscopy,” *Physical Review Letters*, vol. 79, pp. 1134–1137, 1997.
- [155] G. Nahrwold, J. M. Scholtyssek, S. Motl-Ziegler, O. Albrecht, U. Merkt, and G. Meier, “Structural, magnetic, and transport properties of Permalloy for spintronic experiments,” *Journal of Applied Physics*, vol. 108, p. 013907, 2010.
- [156] M. P. Kostylev, A. A. Stashkevich, A. O. Adeyeye, C. Shakespeare, N. Kostylev, N. Ross, K. J. Kennewell, R. Magaraggia, Y. Roussigné, and R. L. Stamps, “Magnetization pinning in conducting films demonstrated using broadband ferromagnetic resonance,” *Journal of Applied Physics*, vol. 108, p. 103914, 2010.
- [157] G. Counil, J.-V. Kim, K. Shigeto, Y. Otani, T. Devolder, P. Crozat, H. Hurdequint, and C. Chappert, “Inductive measurement of the high frequency permeability of a Permalloy thin film,” *Journal of Magnetism and Magnetic Materials*, vol. 272–276, pp. 290–292, 2004.
- [158] S. Tamaru, J. Bain, M. Kryder, and D. Ricketts, “Green’s function for magnetostatic surface waves and its application to the study of diffraction patterns,” *Physical Review B*, vol. 84, p. 064437, 2011.
- [159] V. E. Demidov, S. O. Demokritov, K. Rott, P. Krzysteczko, and G. Reiss, “Self-focusing of spin waves in Permalloy microstripes,” *Applied Physics Letters*, vol. 91, p. 252504, 2007.
- [160] D. R. Birt, K. An, A. Weathers, L. Shi, and M. Tsoi, “Brillouin light scattering spectra as local temperature sensors for thermal magnons and acoustic phonons,” *Applied Physics Letters*, vol. 102, p. 082401, 2013.
- [161] C. Bayer, J. Jorzick, B. Hillebrands, S. O. Demokritov, R. Kouba, R. Bozinoski, A. N. Slavin, K. Y. Guslienko, D. V Berkov, N. L. Gorn, and M. P. Kostylev, “Spin-wave excitations in finite rectangular elements of Ni<sub>80</sub>Fe<sub>20</sub>,” *Physical Review B*, vol. 72, p. 64427, 2005.
- [162] D. G. Cahill, K. Goodson, and A. Majumdar, “Thermometry and Thermal Transport in Micro/Nanoscale Solid-State Devices and Structures,” *Journal of Heat Transfer*, vol. 124, p. 223, 2002.

- [163] A. A. Balandin, “Thermal properties of graphene and nanostructured carbon materials,” *Nature materials*, vol. 10, pp. 569–581, 2011.
- [164] M. M. Sadeghi, M. T. Pettes, and L. Shi, “Thermal transport in graphene,” *Solid State Communications*, vol. 152, p. 1321, 2012.
- [165] C. Jaworski, J. Yang, S. Mack, D. Awschalom, R. Myers, and J. P. Heremans, “Spin-Seebeck Effect: A Phonon Driven Spin Distribution,” *Physical Review Letters*, vol. 106, p. 186601, 2011.
- [166] D. Sanders and D. Walton, “Effect of magnon-phonon thermal relaxation on heat transport by magnons,” *Physical Review B*, vol. 15, p. 1489, 1977.
- [167] H. Adachi, K. Uchida, E. Saitoh, J. Ohe, S. Takahashi, and S. Maekawa, “Gigantic enhancement of spin Seebeck effect by phonon drag,” *Applied Physics Letters*, vol. 97, p. 252506, 2010.
- [168] K. Uchida, H. Adachi, T. An, T. Ota, M. Toda, B. Hillebrands, S. Maekawa, and E. Saitoh, “Long-range spin Seebeck effect and acoustic spin pumping,” *Nature Materials*, vol. 10, pp. 737–741, 2011.
- [169] M. Agrawal and V. Vasyuchka, “Magnon-phonon coupling unmasked: a direct measurement of magnon temperature,” *arXiv preprint arXiv: ...*, 2012.
- [170] F. M. Gerner, A. Majumdar, and C. L. Tien, *Microscale Energy Transport*. Washington DC: Taylor & Francis, 1998.
- [171] Z. Yao, C. Kane, and C. Dekker, “High-field electrical transport in single-wall carbon nanotubes,” *Physical review letters*, vol. 84, pp. 2941, 2000.
- [172] S. Mansfeld, J. Topp, K. Martens, J. Toedt, W. Hansen, D. Heitmann, and S. Mendach, “Spin Wave Diffraction and Perfect Imaging of a Grating,” *Physical Review Letters*, vol. 108, p. 047204, 2012.

## Vita

Daniel attended the Texas Academy of Mathematics and Science at the University of North Texas from 2001-2003. While there he was fortunate to perform research in the Ion Beam Modification and Analysis Laboratory with Prof. Jerome Duggan. For his research accomplishments there, he was awarded a Barry M. Goldwater Scholarship. He attended Caltech from 2003-2007, graduating with a BS in Physics with honors. In 2007 he entered the graduate program of Materials Science and Engineering at the University of Texas at Austin with an NSF IGERT traineeship and began working with Prof. Elaine Li on the project discussed in this dissertation. He is happily married to his beautiful wife with whom he has a seven-month-old son and potential future scientist. Daniel will be joining the Portland Technology Development Group at Intel, beginning in April, 2013.

Permanent email address: [danbirt@gmail.com](mailto:danbirt@gmail.com)

This dissertation was typed by Daniel Birt in Microsoft Word 2010 using MathType to typeset equations and Mendeley as the reference manager.